Chapter 5
Other Existing Carbon Forms

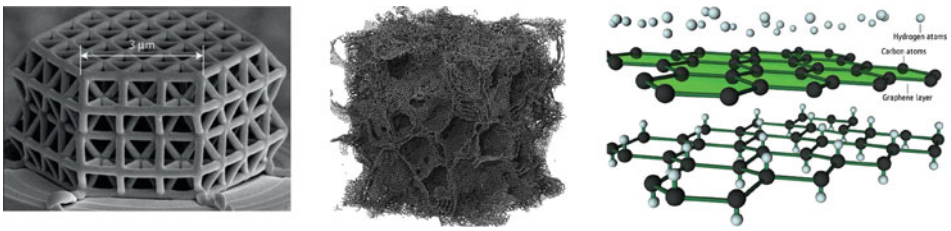

In this section, we show several other carbon allotropes, from those rare as, for example, lonsdaleite to common glassy carbon and "carbon black," xerogels, or hydrogels. In case of carbide- and MOF-derived carbons (relatively new research areas, especially the last one), the production methods vary and structures of formed carbons can be distinct (carbon nanotubes, fullerene- or onion-like nanostructures, nanocrystalline graphitic carbon, amorphous carbon, nanodiamonds, etc.); this is not a special structural type of carbon.

5.1 Glassy Carbon[1]

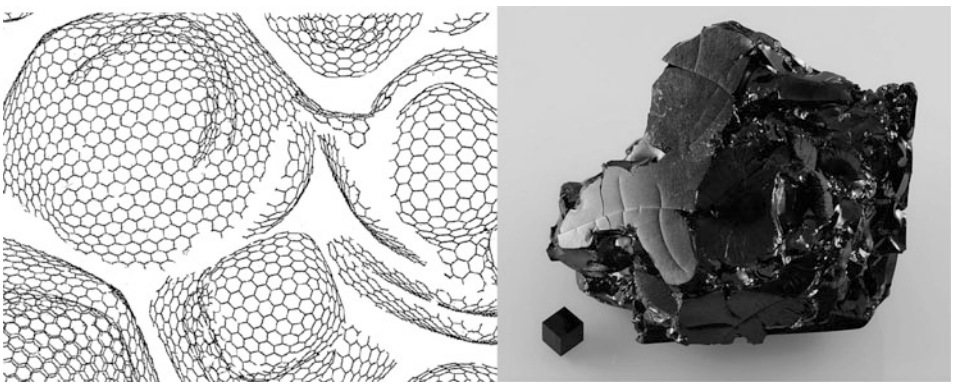

Glass-like carbon (GC, discovered in the mid-1950s; other names–trademarks (not terms): glassy carbon or vitreous carbon) combines glassy and ceramic properties with those of graphite. GC is a non-graphitizing or non-graphitizable carbon. Glassy carbon should not be confused with amorphous carbon.[2] GC's representative properties are as follows:

[1]The GC image above (left) is reproduced with permission of *Taylor & Francis* (P.J.F. Harris. Fullerene-related structure of commercial glassy carbons. *Philosophical Magazine*, **2004**, *84*(29), 3159–3167).

[2]IUPAC: "Glass-like carbon cannot be described as amorphous carbon because it consists of two-dimensional structural elements and does not exhibit 'dangling' bonds" (IUPAC Goldbook, http://goldbook.iupac.org/html/G/G02639.html).

B. I. Kharisov, O. V. Kharissova, *Carbon Allotropes: Metal-Complex Chemistry, Properties and Applications*,
https://doi.org/10.1007/978-3-030-03505-1_5

- 100% sp^2 bonded atoms.
- Young's modulus, fracture stress, and strain values are about 62 GPa, 870 MPa, and 1.3%, respectively [1].
- Hardness.
- High-temperature resistance.
- High purity.
- Low friction.
- Low thermal, electrical resistance and density.
- Impermeability to gases and liquids.
- Extreme resistance to chemical attack.[3]
- Can be produced as an electrically and thermally conductive and corrosion-resistant porous foam.
- Can be doped exhibiting semiconductor phenomena.
- Can be machined into a predetermined shape.
- Chemically inert.
- Resistance in inert gas or vacuum up to 3000 °C and in air up to 600 °C.
- Corrosion resistance.
- High surface quality with excellent polishing characteristics (to a black mirror reflective finish).
- Good resistance to thermal shock.
- Inductive coupling in high-frequency fields.
- No wetting by many saline, metallic, and ceramic melts.
- Biocompatibility.
- Surface coating with metallic and ceramic materials.
- Physical and chemical properties are isotropic.

As it was established long ago, glassy carbons obtained from commercial suppliers contain a high proportion of fullerene-related structures. The presence of curved fragments can be related to the formation of topological defects. sp^2-hybridized carbon layers can yield curved nanostructures such as fullerenes, nanotubes, nanohorns, or nano-onions. Recently, direct evidence of curved planes in GCs (having a fullerene-related structure evolving with the synthesis temperature) and changes in the structure including the degree of curvature of the non-graphitizing glassy carbons as a function of the pyrolysis temperature in the range 800–2500 °C were obtained [2] using neutron and X-ray diffraction measurements and MD calculations. As the carbonization temperature is increased, the C–C bond distribution in GC was found to become more uniform, the domain size rises, the curvature disappears, and the atomic structure tends toward the graphite structure, but without reaching the crystalline 3D order of graphite. The GC microstructure is composed of randomly oriented graphitic crystallites connected by disordered carbon sheets, or a 3D network of curved graphitic ribbons, which loop around each other in no specific orientation.

Glassy carbon is typically synthesized by pyrolyzing any polymeric precursor that cross-links at elevated temperatures [3][4]. As a recent example, the GC-based smallest lattice structure made by man (Fig. 5.1) was reported [4]. Its struts and braces are made of GC and are less than 1 μm long and 200 nm in diameter. This structure was produced by 3D direct laser writing (3D-DLW, a two-photon lithography process) and exhibited material strengths of up to 3 GPa, corresponding approximately to the theoretical strength of GC. Template-based methods are also used, in particular for obtaining glassy carbon nanowires from polymer wires as an intermediate product (Fig. 5.2) [5].

Behavior of carbons (in particular GC) at *high pressures* is object of a permanent interest from long ago [6]. Thus, the transformation of GC into a translucent superhard carbon phase by cold compression was studied in the presence of a uniaxial stress field (Fig. 5.3) [7], revealing that this transition accompanies with sp^2 to sp^3 bonding change in GC causing photoluminescence. Optical images of GC spheres are shown in Fig. 5.4. The volumetric compressions of the larger spheres and the small sphere were roughly calculated to be about 51% and 47% at 53.4 GPa, respectively, analyzing the digital images and assuming an initial spherical shape. In a related report [8], a series of mixed sp^2-sp^3 carbons with outstanding and extraordinary properties (lightweight, ultrastrong (compressive strengths: more than two times that of commonly used ceramics), hard, elastic, and conductive) were recovered after compressing sp^2-hybridized GC at various temperatures. It was shown that the compression induces the local buckling of graphene sheets through sp^3 nodes to form interpenetrating graphene networks with long-range disorder and short-range order on the nanometer scale.

[3]The main reason for the impressive chemical resistance is a consequence of the disordered structure and the inability to form intercalation compounds. This gives rise to high resistance to corrosion by acid and alkaline agents and melts.

[4]Indeed, polymer-derived pyrolytic carbons are highly desirable building blocks for high-strength low-density ceramic meta-materials (*J. Mater. Sci.* **2017**, *52*, 13799–13811).

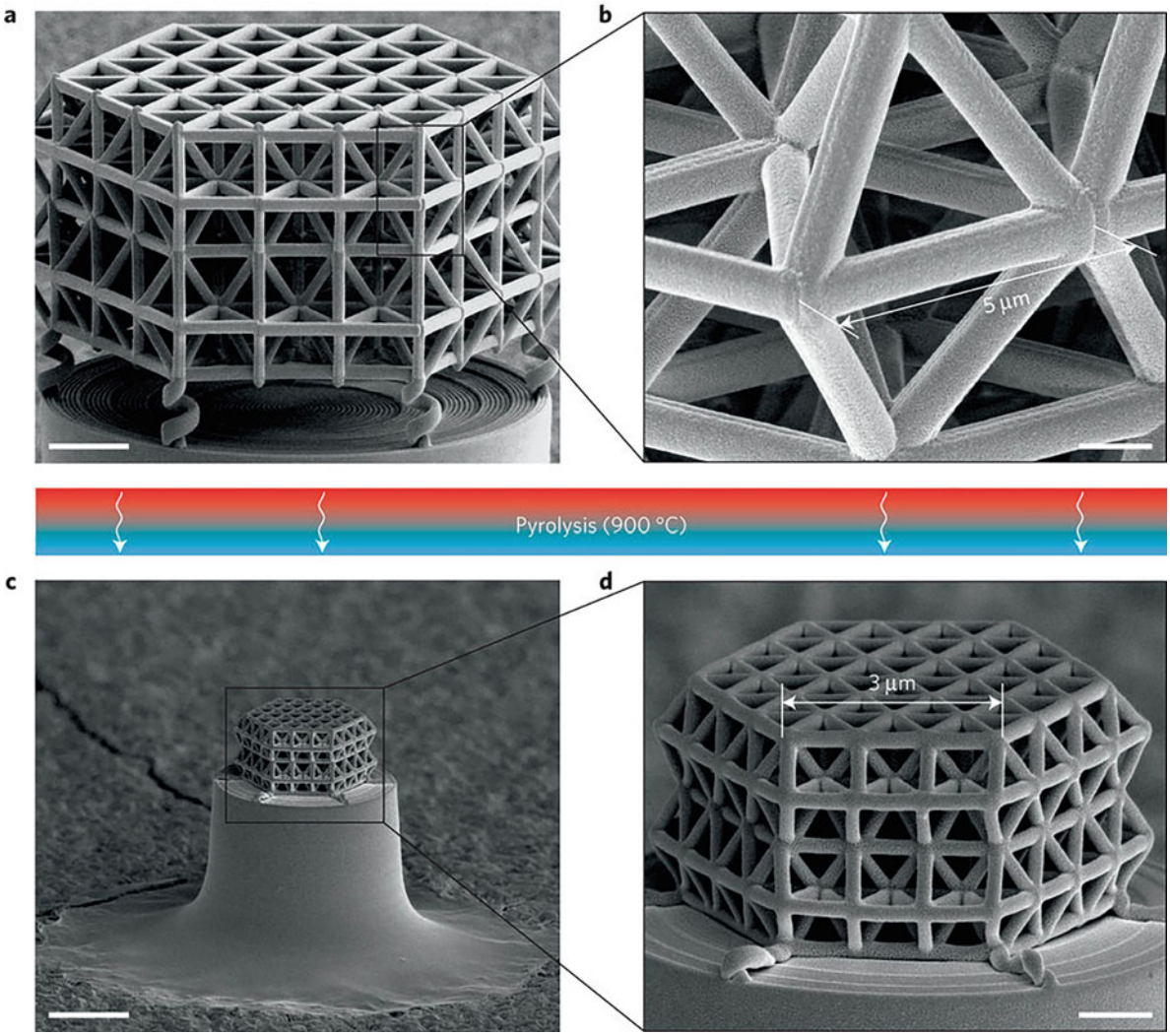

Fig. 5.1 (**a**, **b**) Polymer structure before pyrolysis: whole structure (**a**) and closeup view of a single unit cell (**b**). (**c**, **d**) Facilitated by a supporting construction, which decouples the structures from the substrate, the nanolattices isotropically shrink to about 20% of their initial size during pyrolysis. The magnifications of **a** and **c** (scale bars 5 µm) and also **b** and **d** (scale bars 1 µm) are identical. (Reproduced with permission of *Nature*)

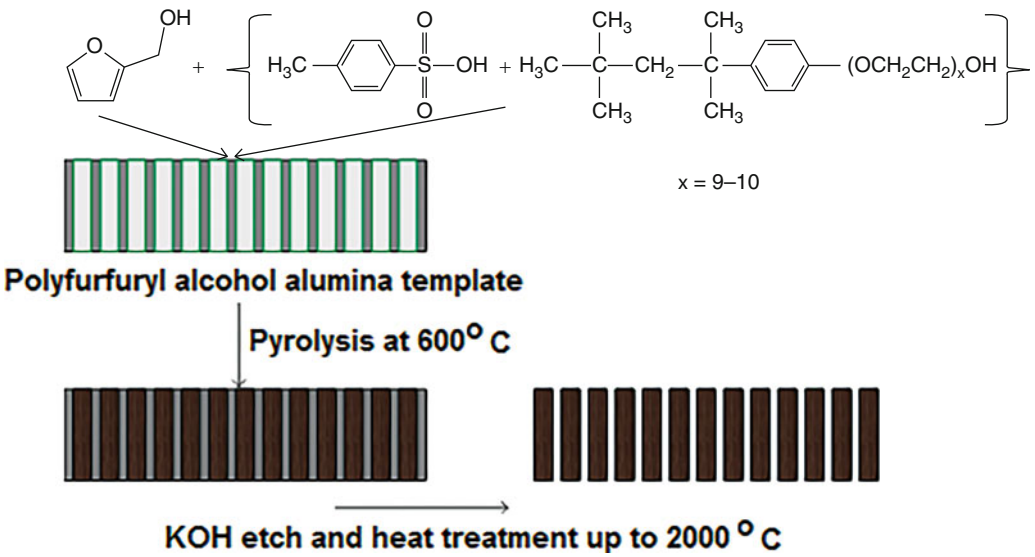

Fig. 5.2 Anodized alumina template-based synthesis of poly-furfuryl alcohol nanowires. The glassy carbon nanowires are obtained by pyrolyzing the polymeric precursor nanowires and then heat treating them at desired temperatures. (Reproduced with permission of the *Hindawi Publishing Corporation*)

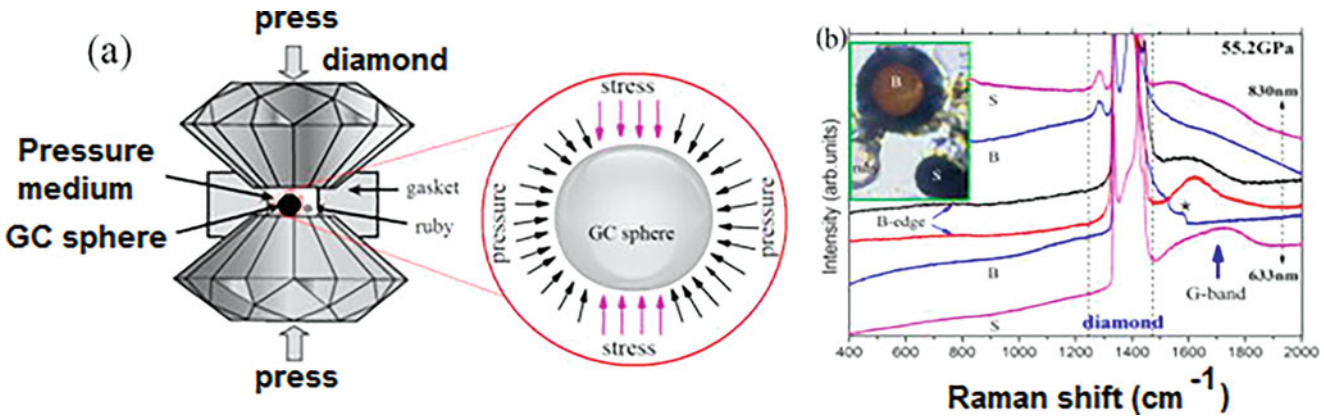

Fig. 5.3 (**a**) Sketch showing the sample loaded into the diamond anvil cell (DAC, left) and the combination of uniaxial stress and chamber pressure exerted on the sphere once it was compressed directly by two anvils (right). (**b**) Raman spectra from the translucent centers of the big ("B") and the opaque small ("S") spheres and from the opaque edge of the big spheres ("B-edge"), at 55.2 GPa. Top two spectra were recorded using an excitation wavelength of 830 nm, with bottom four spectra using 632.8 nm. The peak at 1282 cm^{-1} in the top two spectra is not from glassy carbon. The asterisk near 1580 cm^{-1} points to the position of the Raman line for the diamond-GC sphere contact point, which is used to calculate the uniaxial stress applied on GC. The inset shows an optical image of the spheres in DAC taken under back illumination. Liquid nitrogen was used as PTM. (Reproduced with permission of the *AIP Publishing*)

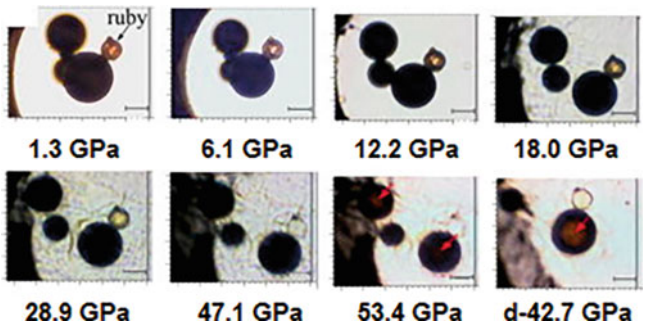

Fig. 5.4 Optical images of three GC spheres at selected pressures in DAC. The last image corresponds to the sample decompressed to 42.7 GPa. The scale bar is 17 μm. All the photos were taken under back illumination. (Reproduced with permission of the *AIP Publishing*)

Additionally to high-pressure studies, the GC was investigated under *laser pulse* treatment. Thus, laser-induced periodic structures with lateral dimensions smaller than the central wavelength of the laser were studied on GC as a function of laser pulse duration (Fig. 5.5) [9]. It was shown that the first laser pulse modifies the surface only slightly (forming only small (~100 nm) particles appearing on the surface), with further increase of periodic changes in the structure up to drastic changes. In all cases the structures are perpendicular to the polarization direction of the irradiating laser light.

For GC *modification and functionalization*, a series of methods and compounds have been used to improve electrode properties, sense, and detect several substances. In particular, SO_2 and SO_2 + H_2O plasma treatments were performed on highly oriented pyrolytic graphite, glassy carbon, and several polymers in order to functionalize their surface with sulfur in different oxidation states [10]. It was confirmed the formation of highly oxidized sulfur species (SO_3, SO_3H, SO_4, and SO_4H) as well as covalently bound sulfur and low oxidized sulfur species (SO and SO_2) being chemisorbed at the surface by this plasma treatment. The degree of oxidation was found to depend on the energy of the ion of the plasma. GCs can be also functionalized or modified by a variety of compounds, in particular MWCNTs [11, 12] (see also below), graphene oxide [13] (see also below), quantum dots (QDs)-phthalocyanine conjugates [14], polyspyrophosphazenes [15], anthraquinone [16], aminobenzene sulfonic acid [17], diazonium salts [18], diaminoalkanes ($NH_2(CH_2)_nNH_2$, $n = 7, 10, 12$) [19], organosilanes [20], MoS_2 [21], and other metal-based species ($Cu/Cu(OH)_2$ and $RuO_2/Ru(OH)_2$) and Prussian blue [22]. Other applications of GCs are as follows [23]:

- Electrode material in electrochemical processes [24–28], in particular CO_2 reduction by *fac*-Mn(apbpy)$(CO)_3$ Br and *fac*-Re(apbpy)$(CO)_3$Cl [29]
- Component of some prosthetic devices
- Microscopy and microanalysis

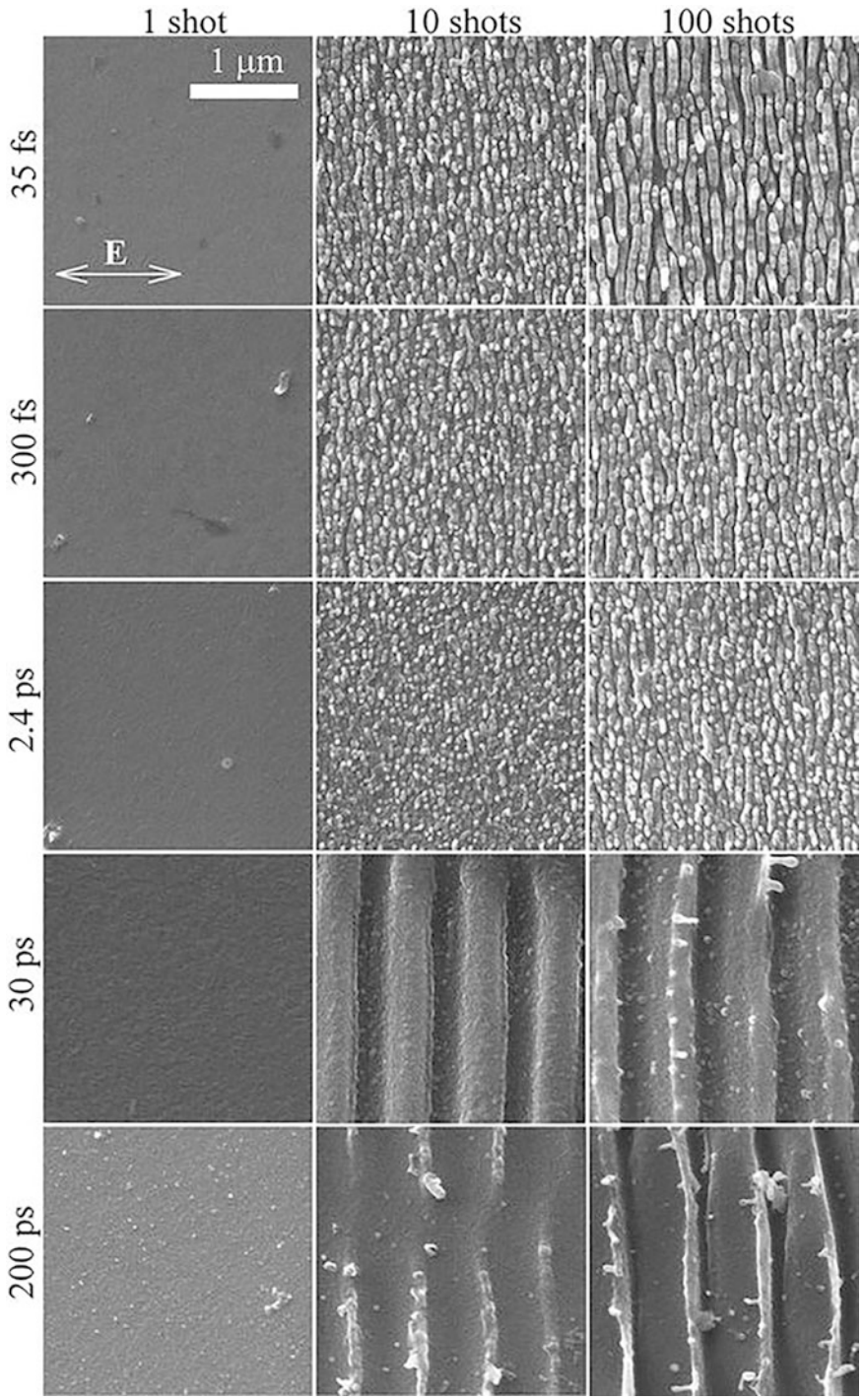

Fig. 5.5 SEM images recorded from the Ti:S laser-treated samples. The pulse numbers and the pulse durations are indicated by the headers. (Reproduced with permission of *Springer*)

- Metallurgical
- Laboratory research
- Vacuum evaporation
- Supercapacitors [30]
- Semiconductors and electronics
- Nuclear industry and a fast shutter valve in particle accelerator [31, 32]

- Aerospace (thermal protection materials) [33]
- Tribological uses [34]
- GC membranes [35]
- Medical uses [36]
- High-temperature crucibles, boats, rods, foams, dishes, powders, and much more [37]

Here, we briefly discuss selected applications of modified GC electrodes as sensors. Thus, a glassy carbon electrode was modified with amino-functionalized graphene oxide (GO) and molecularly imprinted polymer for electrochemical sensing of bisphenol A (Fig. 5.6) [38]. The fabricated GO-based sensor not only provided high sensitivity and selectivity for BPA but also displayed good repeatability, remarkable stability, linear range, and satisfactory recoveries. For simultaneous determination of acetaminophen (Ac) and tyramine (Tyr), a GC electrode modified with functionalized MWCNTs showed limits of detection of 0.42 μM (3σ) for Ac and 0.8 μM (3σ) for Tyr (Fig. 5.7) [39].

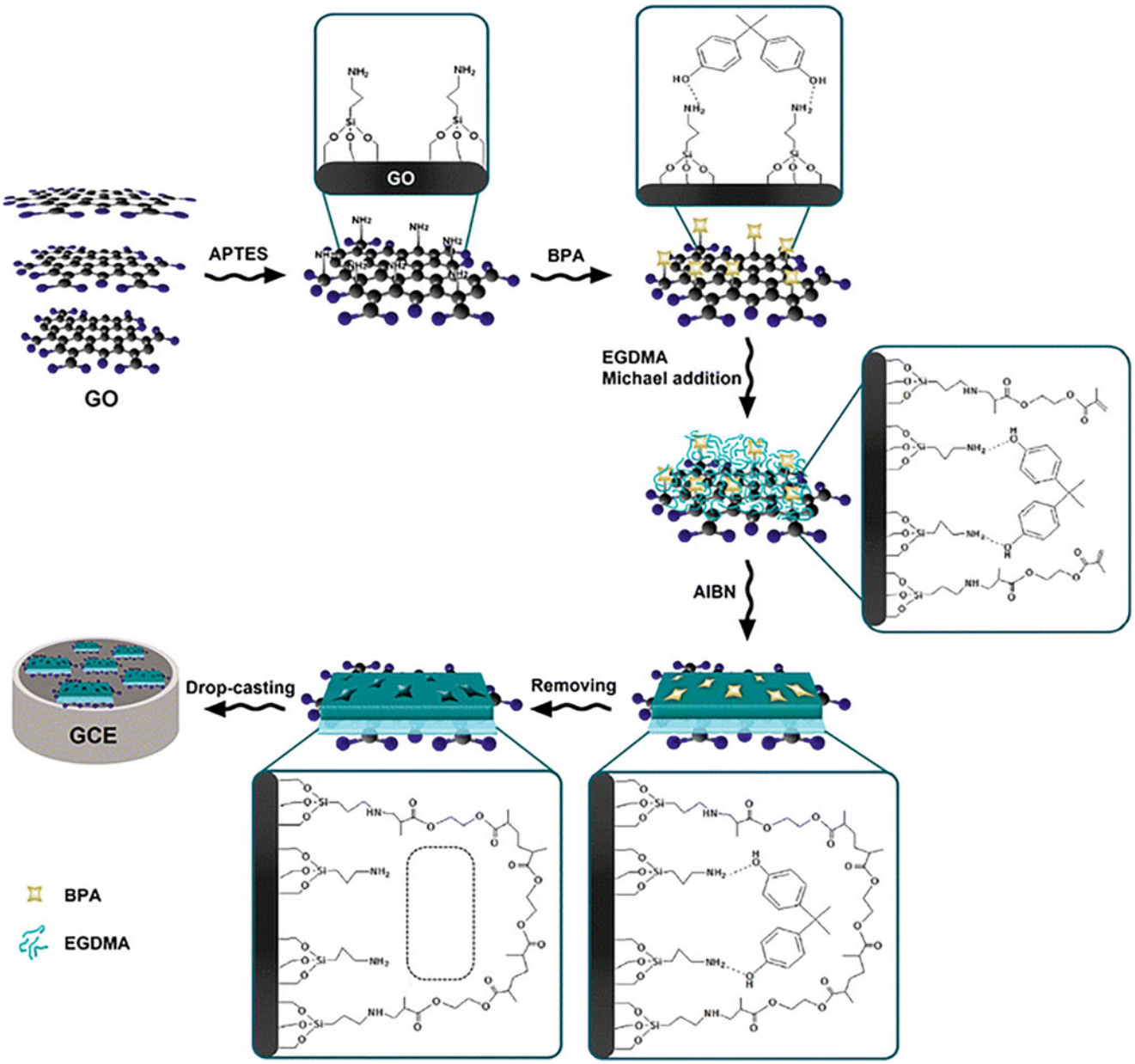

Fig. 5.6 Schematic illustration of the fabrication procedure of GO/APTES–MIP sensor by surface immobilized template strategy (APTES, 3-aminopropyltriethoxysilane; MIP, molecularly imprinted polymer). (Reproduced with permission of *Springer*)

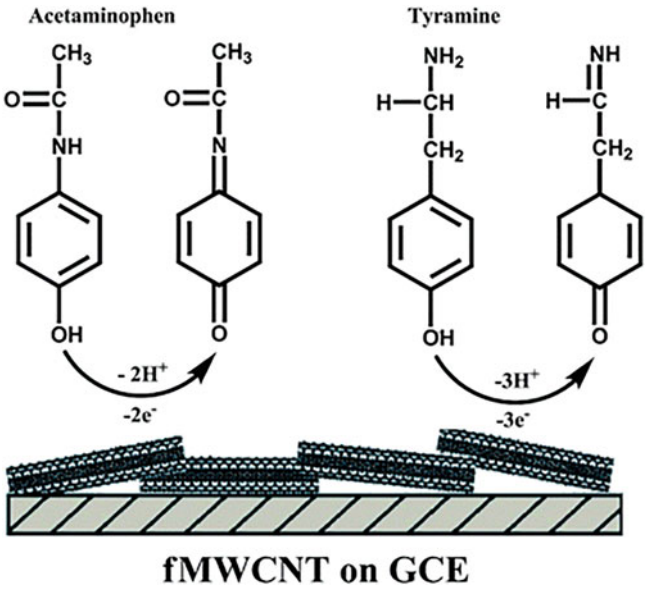

Fig. 5.7 Possible reaction for electrochemical oxidation of Ac and Tyr at the surface of fMWCNT-MGCE. (Reproduced with permission of the *Royal Society of Chemistry*)

5.2 Carbon Black

Carbon black (CB),[5] known from ancient civilizations in China and Egypt as a soot, is a commercial form of solid carbon that is manufactured in highly controlled processes to produce specifically engineered aggregates of carbon particles that vary in particle size, aggregate size, shape, porosity, and surface chemistry [40]. Carbon black can be considered as a highly disordered form of graphitic carbon. By heating the substance to 3000 °C under inert conditions, it is changed into an ordered graphitic formation. Carbon black main properties are as follows:

- Should not be confused with black carbon, atmospherical contaminant containing carbon with other impurities (i.e., heavy metals, among others) [41]. The terms carbon black and soot have often been used interchangeably despite the fact that soot by definition is an undesired by-product of incomplete combustion of fossil fuels and biomass. The terms carbon black and black carbon are often misused.
- Black carbon (BC) is a collective term that describes a range of carbonaceous substances from partly charred plant residues to highly graphitized (i.e., highly ordered molecular carbon structures as found in graphite) soot that are generated as products of incomplete combustion.
- Essentially carbon blacks are the pure soot. However, it is dissimilar to soot in its much higher surface-area-to-volume ratio and significantly lower (negligible and non-bioavailable) PAH (polycyclic aromatic hydrocarbon) content [42].

[5]See also the section below about carbon allotropes in the environment.

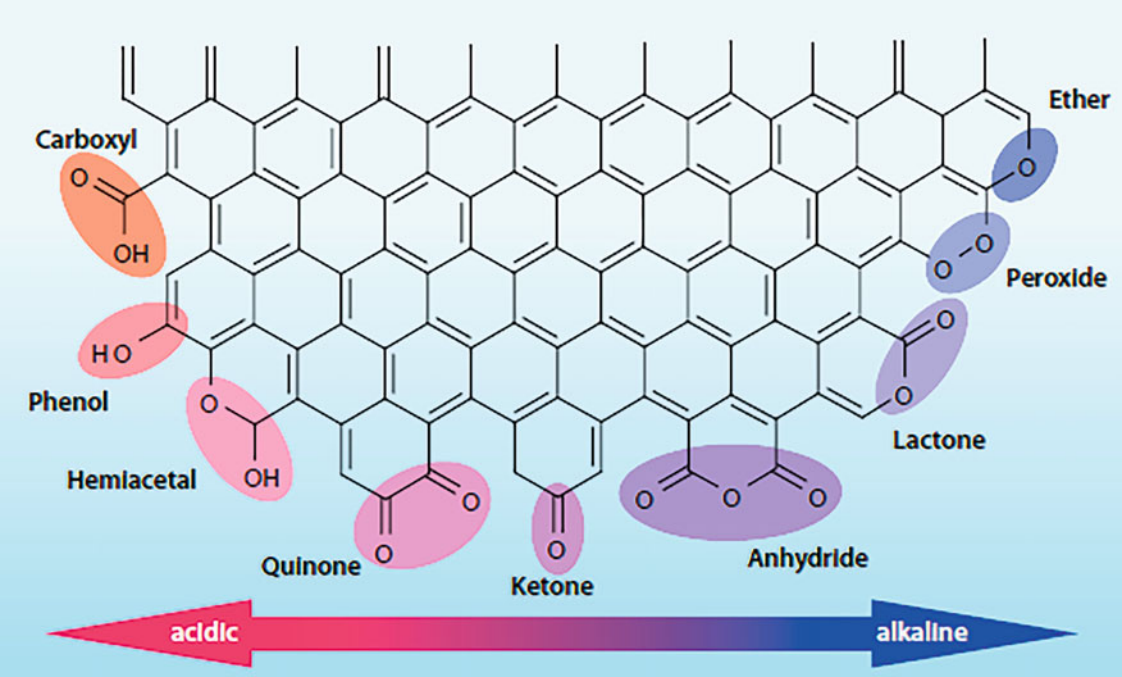

Fig. 5.8 The surface of carbon black can bind oxygen in the form of acidic or alkaline functional groups. (Reproduced with permission of *Orion Engineered Carbons*)

- Contains more than 95% pure carbon with minimal quantities of oxygen (0.2–0.5%), hydrogen (0.2–1.3%), and nitrogen (0–0.7%), as well as sulfur (0.1–1.0) and residual ash (up to 1%).
- sp^2 carbon.
- Particle size in the range of 10–500 nm, fused into chain-like aggregates with 3D arrangement of primary particles in it.
- Surface of carbon black can bind oxygen in the form of acidic or alkaline functional groups (carbonyl, carboxyl, pyrone, phenol, quinone, lactol, and ether groups, Fig. 5.8).
- Smaller carbon black primary particles have a higher specific surface area.
- The removal of traces of organic elements is possible with the use of special solvents.
- Carbon black also contains traces of metals and nonmetals (Sb, As, Ba, Cd, Cr, Co, Cu, Pb, Ni, Hg, Se, Zn).
- Density may vary from 1.7 to 1.9 g/cm^3.
- Porosity, a fundamental property of carbon black, can be controlled during the production process.
- Oxidized surfaces improve pigment wetting, dispersion, rheology, and overall performance in selected systems.
- Oxidation increases electrical resistivity and makes carbon blacks more hydrophilic.
- High volatile levels of volatile components (surface oxygen groups) are associated with low pH.
- It is known to be a nonconductive material due to its volatile content.
- Excellent absorption of UV light.
- Production cost $1/kg.
- Carbon black is considered possibly carcinogenic to humans and classified as a group 2B carcinogen.
- Black carbon second only to CO_2 in heating the planet [43].

Raw materials for the carbon black are normally heavy oil (having the greatest carbon-to-hydrogen ratio) with a high content of aromatic hydrocarbons, natural gas (inexpensive), coal tar distillates (carbo-chemical oils), mineral, vegetable or residual oils, ethylene cracking tar, or acetylene. The most suitable oils are those in which the majority of the carbon is in the form of substances comprising three- or four-membered rings. The *production methods* below are based on their heating and decomposition (thermal or thermal–oxidative decomposition) processes. As one of the thermal–oxidative processes, we note the *furnace black process* (Fig. 5.9), the most common method, using liquid and gaseous hydrocarbons as feedstock and as heat source, respectively. Particle size or specific surface area can easily be defined at the outset by setting the appropriate process parameters, making it possible to produce a broad range of carbon blacks (Fig. 5.10), which are suitable for use in various applications without fundamentally changing the process for each product variant. An alternative technique is

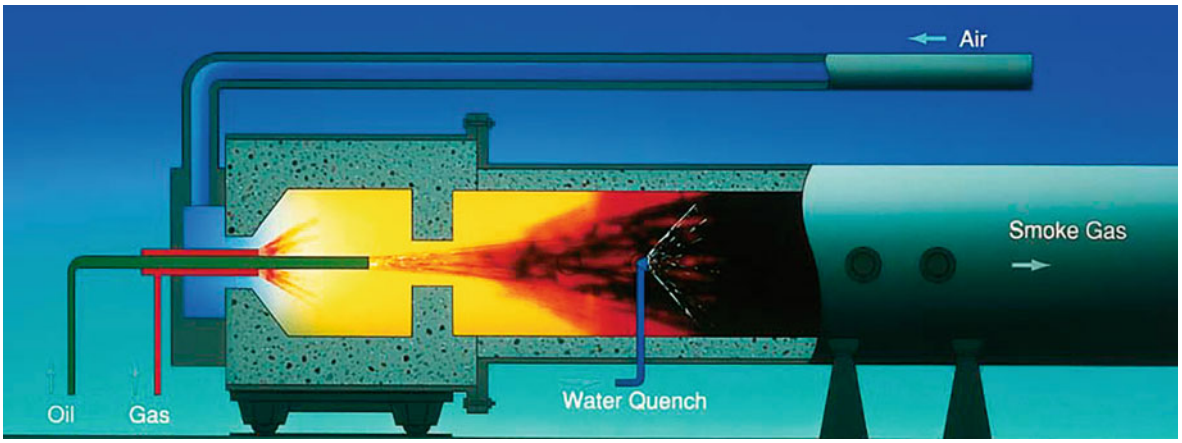

Fig. 5.9 Scheme of a furnace black reactor. (Reproduced with permission of *Orion Engineered Carbons*)

Fig. 5.10 From left to right: powder carbon black, dry-pelletized carbon black, wet-pelletized carbon black. (Reproduced with permission of *Orion Engineered Carbons*)

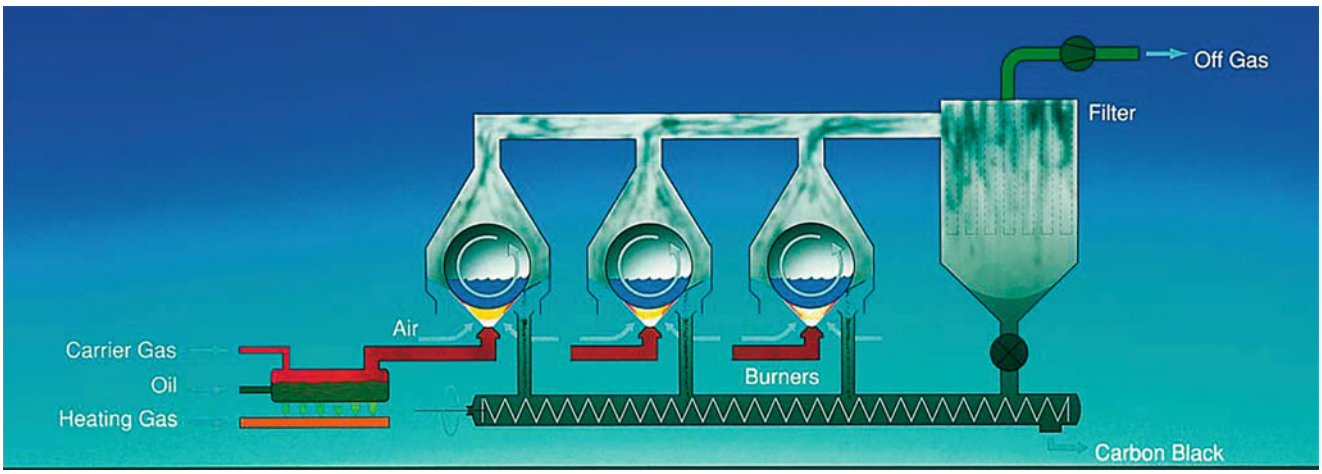

Fig. 5.11 Scheme of gas black production process. (Reproduced with permission of *Orion Engineered Carbons*)

Degussa gas black process (Fig. 5.11), using oil or coal tar distillates as raw material and realized in continuously vacuum-cleaned facilities. As a result of contact with oxygen at high temperatures, acidic oxides form on the surface of the carbon black particles (Fig. 5.12). In contrast to furnace blacks, gas blacks undergo an acidic reaction when suspended in water. Another process is the oldest *lamp black process* (Fig. 5.13), resulting in carbon blacks with a broad primary particle size distribution ranging from approximately 60 to over 200 nm (Fig. 5.14) and widely used in special applications.

As thermal decomposition processes, we note the *thermal black process* (Fig. 5.15), which is a noncontinuous or cyclic process in the absence of oxygen and at decreasing temperature, with natural gas as the most commonly used feedstock,

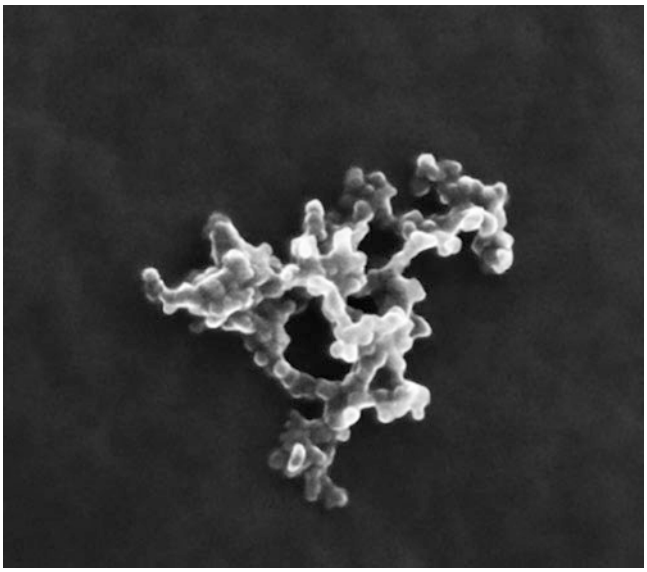

Fig. 5.12 Electron microscope view of gas black particles. (Reproduced with permission of *Orion Engineered Carbons*)

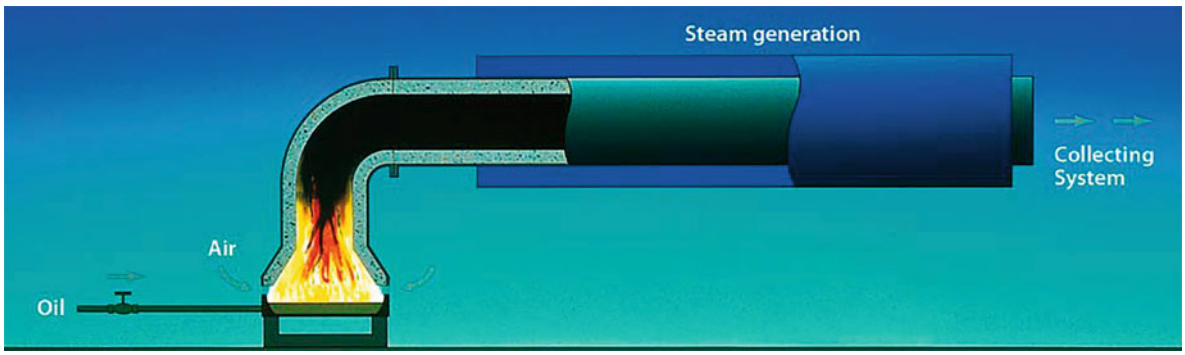

Fig. 5.13 Scheme of lamp black production process. (Reproduced with permission of *Orion Engineered Carbons*)

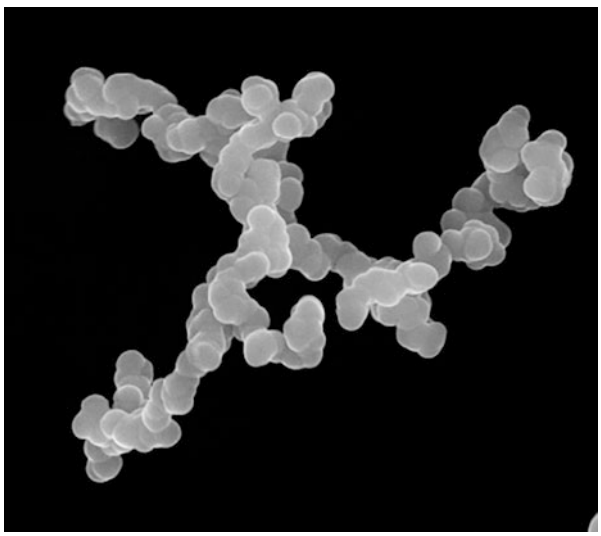

Fig. 5.14 Electron microscope view of lamp black particles. (Reproduced with permission of *Orion Engineered Carbons*)

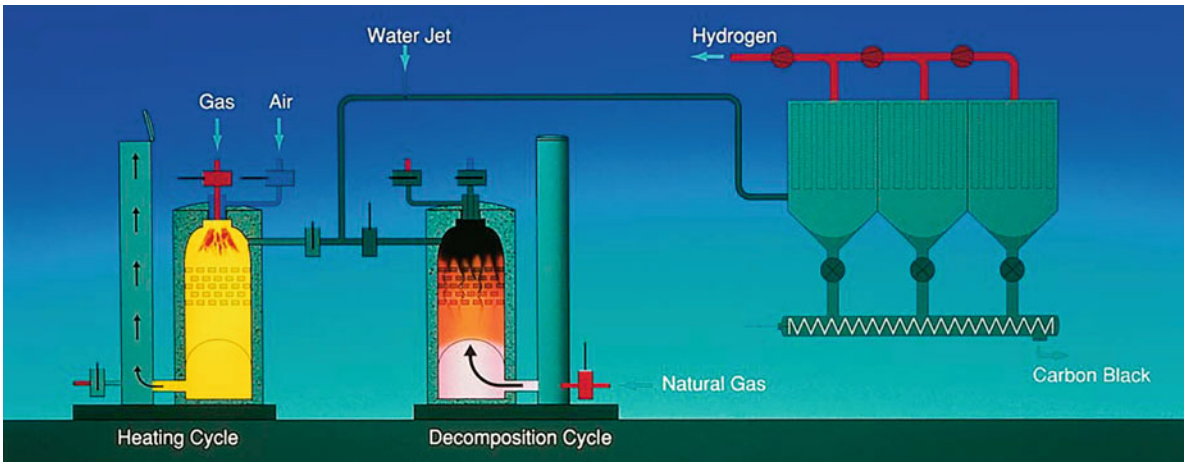

Fig. 5.15 Scheme of thermal black production process. (Reproduced with permission of *Orion Engineered Carbons*)

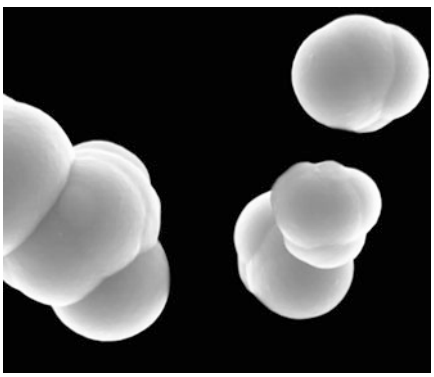

Fig. 5.16 Electron microscope view of thermal black particles. (Reproduced with permission of *Orion Engineered Carbons*)

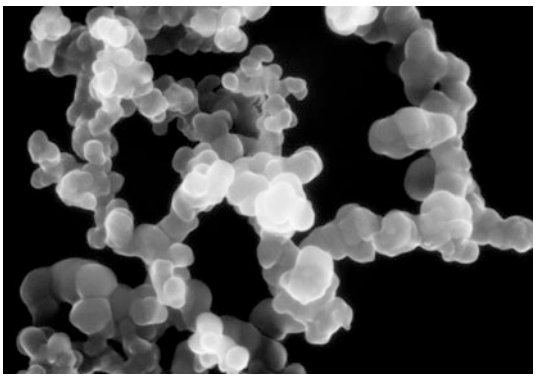

Fig. 5.17 Electron microscope view of acetylene black particles. (Reproduced with permission of *Orion Engineered Carbons*)

although higher-grade hydrocarbon oils are also used. Resulting primary particle sizes range from 300 to 500 nm (Fig. 5.16). Finally, the *acetylene black process* is carried out at higher temperatures, when exothermic decomposition of acetylene yields carbon (Fig. 5.17) and hydrogen.

Three main properties (Fig. 5.18) of carbon black are "particle size" (size of spherical particles), "structure" (size of the particle chain), and "surface chemistry" (functional groups on surface), having a large effect on practical properties such as blackness and dispersibility when they are mixed with inks, paints, or resins. Its surface area varies (15–64 m^2 per gram) depending on the production method. High surface area is usually associated with greater jetness, higher conductivity, improved weatherability, and higher viscosity but requires increased dispersion energy [44]. The importance of carbon black structure on mechanical and rheological properties is well documented [45]. In addition, a surprising conclusion was made that the primary particles of carbon blacks are highly defective multi-shell fullerenes (Fig. 5.19) [46]. A synthesis of C_{60}, carbon nano-onions, and nano- to submicron diamonds by pyrolysis was proposed on this basis, so carbon blacks can be considered as source materials for carbon nanotechnology.

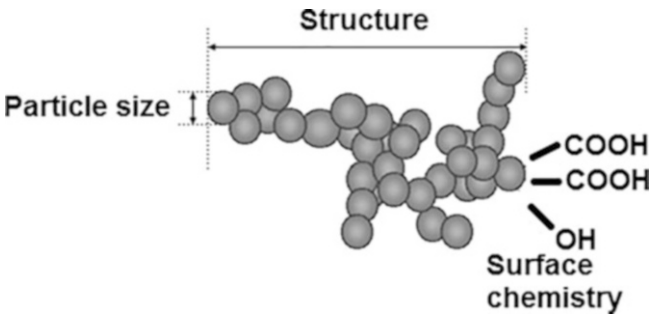

Fig. 5.18 Three main properties of carbon black [47]. (Reproduced with permission of the *Mitsubishi Chemical Co.*)

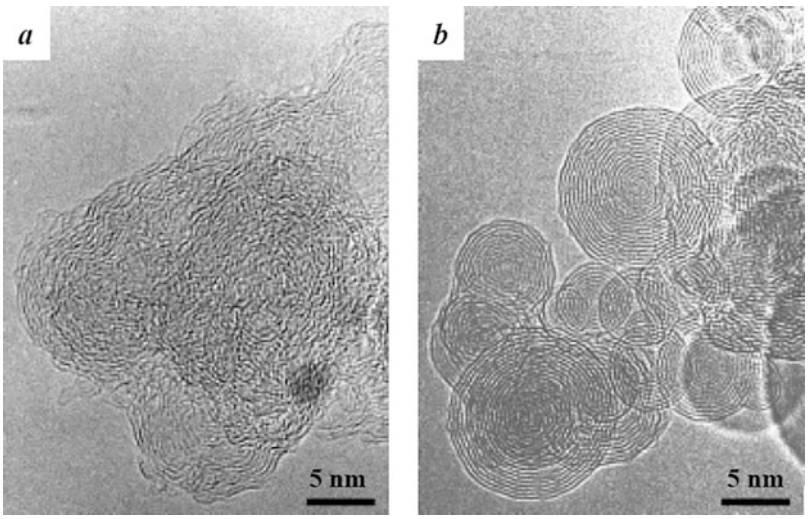

Fig. 5.19 Crystallization of carbon black structure by intensive electron beam bombardment (JEOL, JEM-2010 at 200 keV, ~150 A/cm^2) onto Toka Black #8500F claimed to have an average diameter of 14 nm in the primary particles. (**a**) Pristine structure shows numerous defects and ambiguous grain boundaries. (**b**) After irradiation for 20 min at this spot, spherical contours and inner layers of carbon nano-onions clearly appeared. (Reproduced with permission of the *Elsevier Science*)

Influence on the Climate Carbon black (in this case – more exactly – black carbon), emitted by fossil fuel combustion and biomass burning, is now considered among most important substances, responsible for heating the planet [48]. In particular, black carbon emissions from household cookstoves consuming solid fuel produce approximately 25% of total anthropogenic BC emissions [49]. Investigations on the influence of its aerosols on atmospheric processes have been carried out in a series of countries, in particular India [50] and other Asian countries. Thus, black carbon emitted from fires in northern Eurasia is transported and deposited on ice and snow in the Arctic and can accelerate its melting during certain times of the year [51]. The coating materials of atmospherically aged black carbon consist mainly of sulfate, nitrate, ammonium, and organic carbon (Fig. 5.20) [52]. Also, black carbon in soot is the dominant absorber of visible solar radiation in the atmosphere [53]. Anthropogenic sources of black carbon, although distributed globally, are most concentrated in the tropics where solar irradiance is highest. Black carbon is often transported over long distances, mixing with other aerosols along the way. The aerosol mix can form transcontinental plumes of atmospheric brown clouds, with vertical extents of 3–5 km.

Main Applications Carbon black is used in distinct groups of materials improving their physicomechanical, optical, electrical, and other properties. Its predominant part is used as a reinforcement and performance additive in rubber products, improving their resilience, tear strength, conductivity, and other properties [54]. Carbon black is added to the rubber used in tire treads, to high-pressure hoses, and has other demanding applications, as well as added to plastics as material reinforcement [55]. Also, carbon black is used as black pigment for a variety of applications in the coatings, polymers, and printing industries. It can be a part of magnetic flexible composites, as, for example, $NiCoFe_2O_4$–carbon black hybrids grafted in a PVA matrix [56]. Another example of carbon black composite is a minor thermoplastic polyurethane (TPU) phase spreading at the interface of two major phases polyoxymethylene/polyamide copolymer (POM/COPA) and carbon black particles selectively localized at the TPU/COPA interface of the tri-continuous blends fabricated by melt compounding [57].

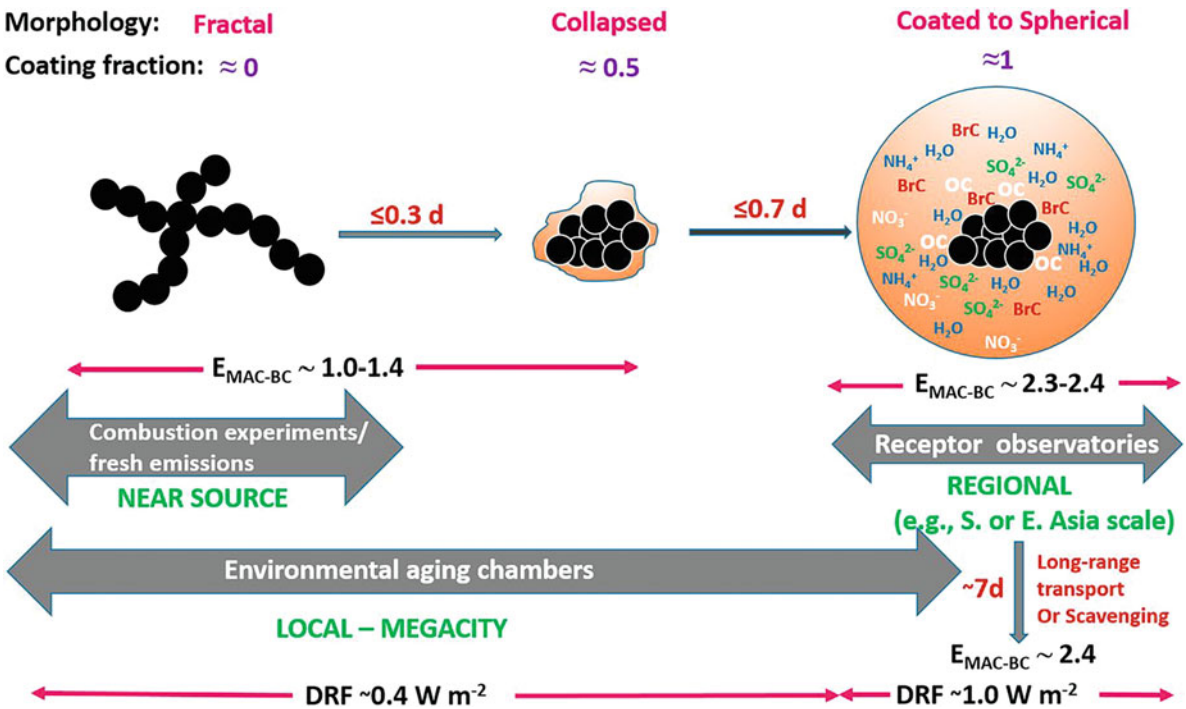

Fig. 5.20 Time-course evolution of black carbon aerosol composition, light absorption (where EMAC-BC is the enhancement because of coatings), and associated climate effects (as DRF) (Copyright (2016) *National Academy of Sciences*)

5.3 Carbon Hydrogels, Cryogels, Xerogels, and Aerogels[6]

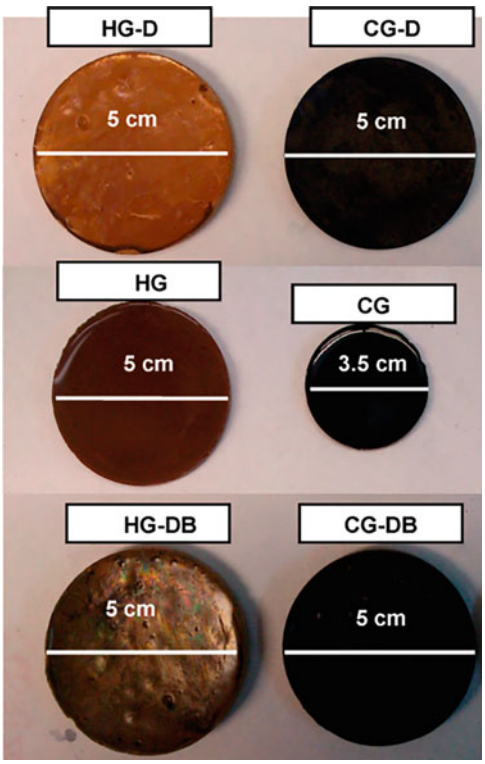

[6]Reproduced with permission of *MDPI* (*Gels*, **2016**, *2*, 4).

Definitions The term *hydrogel* describes 3D network structures obtained from a class of synthetic and/or natural polymers which can absorb and retain significant amount of water. The hydrogel structure is created by the hydrophilic groups or domains present in a polymeric network upon the hydration in an aqueous environment [58]. Hydrogels are broadly classified into two categories: *permanent/chemical gel* (when they are covalently cross-linked (replacing hydrogen bond by a stronger and stable covalent bonds) networks and *reversible/physical gel* (when the networks are held together by molecular entanglements and/or secondary forces including ionic, hydrogen bonding, or hydrophobic interactions). A *xerogel* is a solid formed from a gel by drying it slowly at about room temperature with unhindered shrinkage. Xerogels usually retain high porosity (25%) and enormous surface area (150–900 m^2/g), along with very small pore size (1–10 nm). *Aerogels* are synthetic porous materials derived from sol–gel materials in which the liquid component has been replaced with gas to leave intact solid nanostructures without pore collapse [59]. A *cryogel* is a highly porous monolithic or powdered product of freeze-drying of frozen suspensions and gels and their subsequent heat treatment. The specific surface area of cryogels typically ranges from 300–400 m^2/g (transition metal hydroxides) to 700–800 m^2/g (carbon and silica cryogels).

Carbon *aerogels* (CAs), a special class of aerogels that are derived by the pyrolysis of organic precursors at temperatures higher 1000 °C [60], are a light porous material connected by several spherical nanoparticles and are materials which are currently of interest for catalysis, lithium–ion batteries [61], and onboard lightweight hydrogen storage applications. Generally, their doping with transition metals or lanthanides improves these and other properties. Thus, for example, Pd-, Ti-, or Fe-doped carbon aerogels with high surface area and mesoporous structures, prepared by standard resorcinol–formaldehyde method (Fig. 5.21),[7] facilitated hydrogen diffusion and adsorption [62]. Metal nanoparticle dispersion onto the CAs

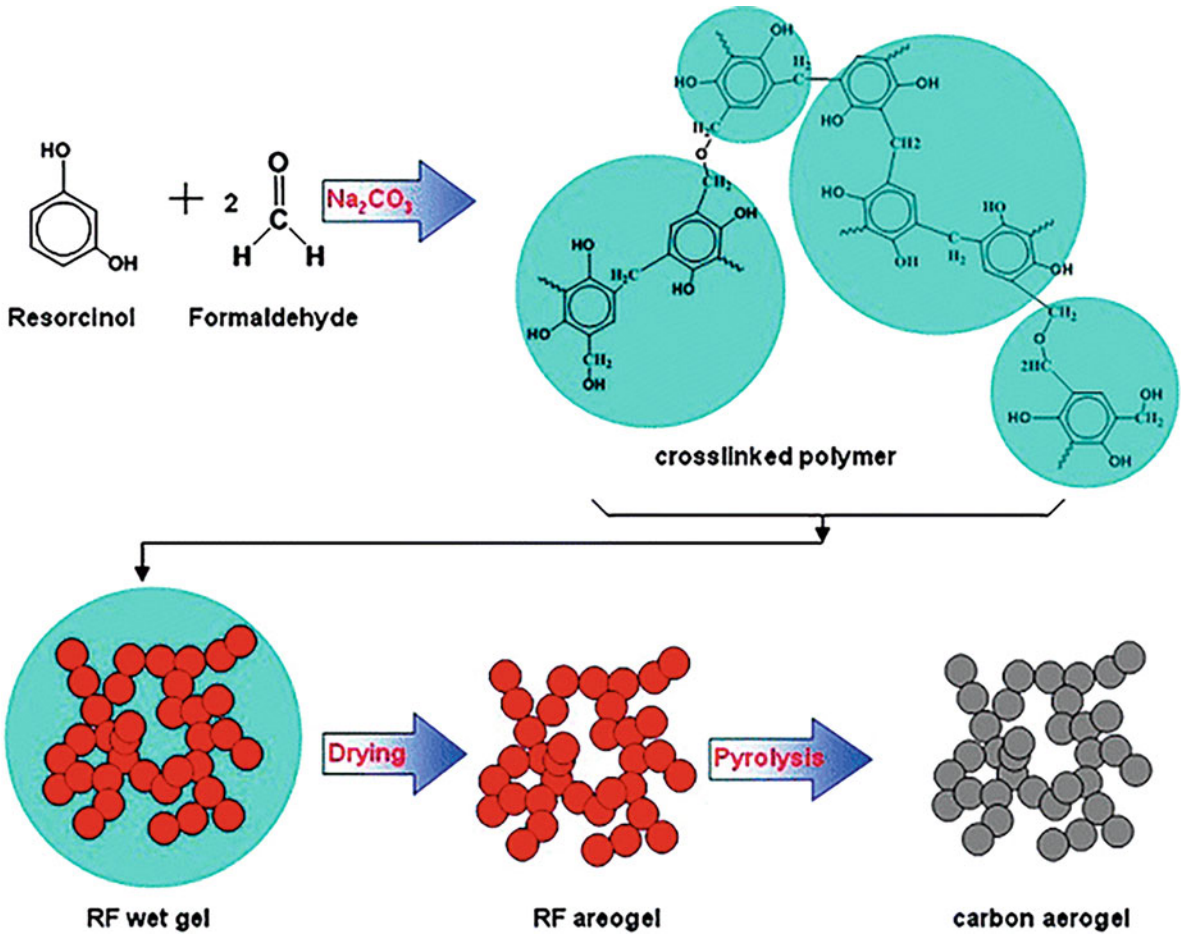

Fig. 5.21 Reaction mechanism for the synthesis of resorcinol–formaldehyde (RF) wet gels, aerogels, and carbon aerogels. (Reproduced with permission of *Springer* Ref. [206])

[7]This method is mentioned in a variety of reports on carbon aerogels. Other precursors of carbon aerogels are phenolic–furfural and melamine–formaldehyde aerogels, among others (*Aerogels Handbook. Advances in Sol-Gel Derived Materials and Technologies.* Springer, **2011**, New York, NY.).

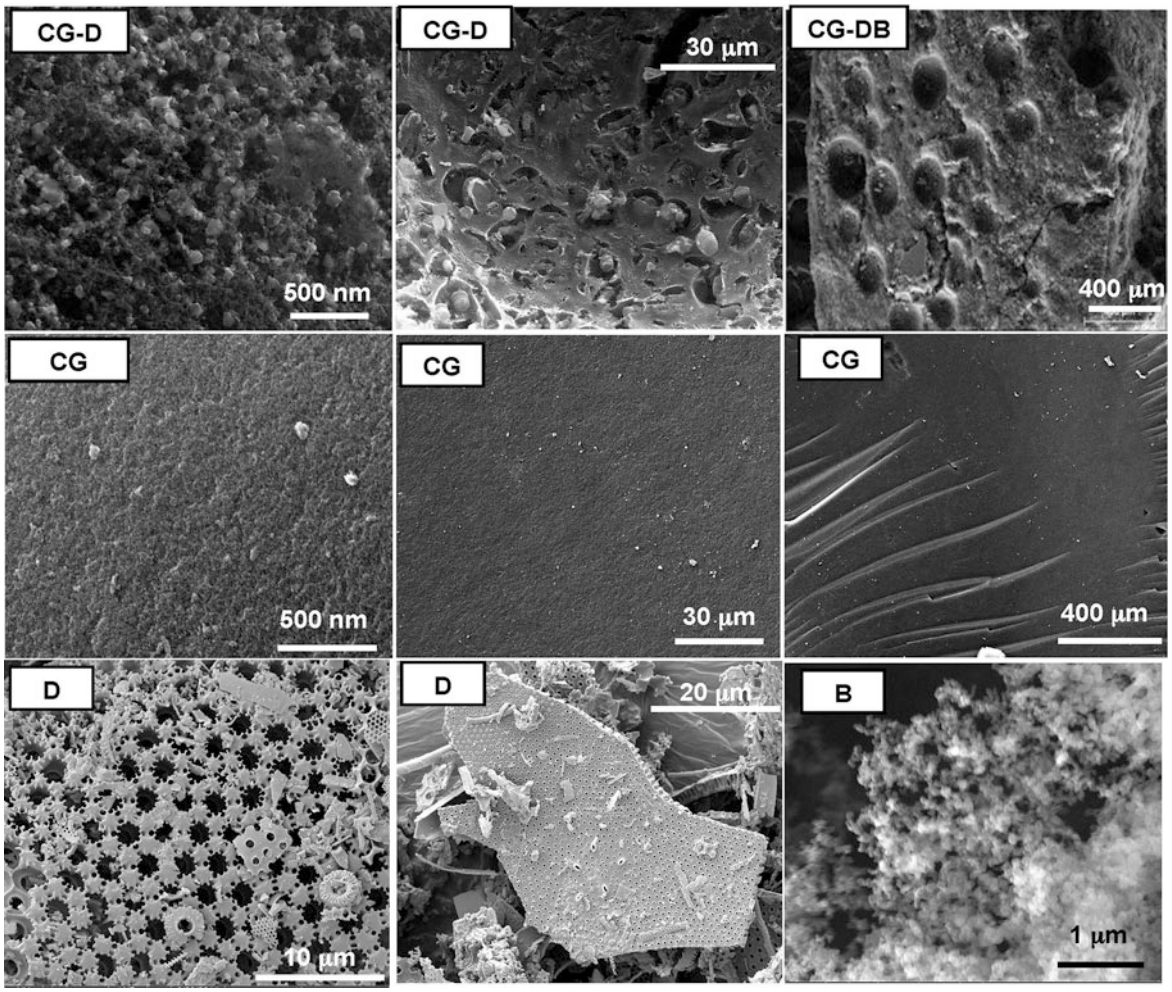

Fig. 5.22 Scanning electron microscopy (SEM) images representative of the studied monolithic aerogels prepared in the presence and absence of the additives. Images of the diatomite (sample D) and the carbon black (sample B) are also shown for clarity. (Reproduced with permission of *MDPI*)

was found to improve the hydrogen adsorption abilities. Lanthanide-doped (Ln = Ce, La, Nd, Pr) carbon aerogels were obtained based on the similar modified resorcinol–formaldehyde aerogel preparation procedure and were tested as catalysts for the Michael reaction [63]. The mostly mesoporous materials with pore size diameters around 5–15 nm contained up to 22 wt.% of metal. For Ln-doped carbon aerogels, the conversion was found to be modest (Ln = Pr, 32%) to high (Ln = Nd, 92%). In addition to doping with metals, the formation of composites is also in a favor for carbon aerogels, improving their mechanical and other properties. For instance, monolithic carbon aerogels, prepared by sol–gel polycondensation of melamine–resorcinol–formaldehyde mixtures by incorporating diatomite and carbon black additives, displayed (Fig. 5.22) a well-developed porous structure. The diatomite prevented structural shrinkage and deformation of the as-prepared monoliths upon densification by carbonization, even after removal of the siliceous framework [64].

Among carbon aerogels and hydrogels, the graphene oxide ones are of an especial interest (in particular, for active bacteria adsorption and removal [65]). Thus, the fabrication of hierarchically structured, reduced graphene oxide (rGO) aerogels with heavily loaded (46–67 wt. %) palladium (Pd), platinum (Pt), nickel (Ni), and tin (Sn) metallic nanoparticles was carried out from metal salts chelated with EDTA, mixed with graphene oxide (GO), then freeze-dried, and reduced [66]. It was suggested that rGO aerogels can achieve a higher nanoparticle loading by using chelation to minimize electrostatic interactions between metal ions and GO. In case of Pd nanoparticles, their higher loading in graphene aerogels lead to improved hydrogen gas sensing performance, other possible applications could be energy storage and catalysts of vapor phase reactions. Another method of metal loading by graphene oxide is the use of Prussian blue (PB, Fig. 5.23), whose nanoparticles were used to

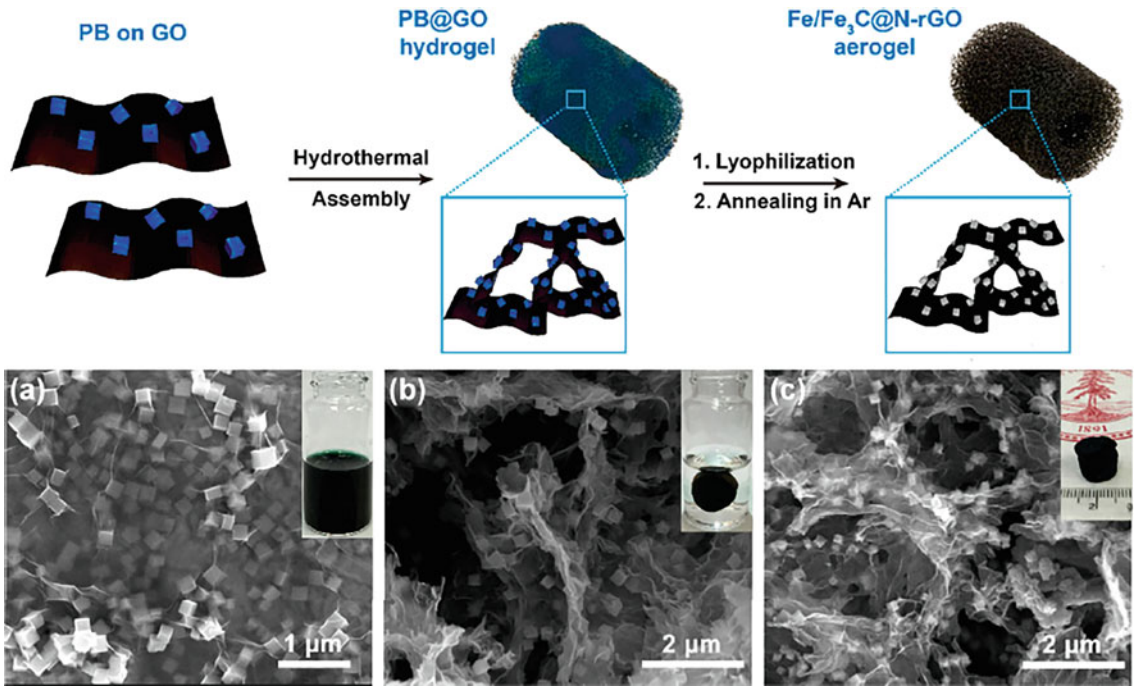

Fig. 5.23 Fabrication process of the 3D Fe/Fe_3C@N-rGO aerogel catalyst. SEM images of (a) the as-synthesized PB@GO, (b) the PB@GO hydrogel obtained via hydrothermal treatment in acidic medium in the presence of DCDA, and (c) the Fe/Fe_3C@N-rGO aerogel catalyst obtained via lyophilization and pyrolysis of the PB@GO hydrogel (insets are the digital camera images of the corresponding states). (Reproduced with permission of *Springer*)

anchor Fe/Fe_3C species to nitrogen-doped reduced graphene oxide aerogels as outstanding ORR catalysts [67]. PB is an ideal precursor to obtain the M–N/C catalyst due to its large surface area, high-density Fe–N_4 coordination sites, and low cost. The strong interaction between nanosized Fe_3C and the graphitic carbon shell led to synergistic effects in the ORR, and the protection of the carbon shell guaranteed stability of the catalyst. We note also GO/polyethylenimine (PEI) hydrogels (Fig. 5.24), which were revealed as efficient dye adsorbents, exhibiting removal rates within about 4 h in accordance with the pseudo-second-order model [68]. The GO/PEI hydrogels were prepared through both hydrogen bonding and electrostatic interactions between amine-rich PEI and GO sheets. The dye-adsorbed hydrogels can be conveniently separated from an aqueous environment, suggesting potential large-scale applications of the GO-based hydrogels for wastewater treatment.

Carbon aerogels can be also obtained from *natural products*. Thus, hierarchical porous N-doped carbons were fabricated from cellulose for use as high-performance supercapacitors and CO_2 capture applications [69]. Porous cellulose aerogels were first obtained via a dissolving–gelling process and then carbonized in NH_3 atmosphere (Fig. 5.25) to give hierarchical porous N-doped carbon aerogels with more interconnected macropores and micropores. Thus obtained N-doped carbon aerogel exhibited an exceptional CO_2 adsorption capacity of 4.99 $mmol \cdot g^{-1}$, which is much higher than those of other porous carbons. In a similar report [70], porous carbon aerogel (CA)/NiO composite (Fig. 5.26) were prepared by pyrolysis of sodium carboxymethyl cellulose aerogels via a sol–gel and freeze-drying process. The resultant CA/NiO composites possess an interconnected 3D structure, high specific surface area of up to 175.05 m^2/g, and saturation magnetization of 3.14 emu/g, presenting excellent electrochemical performance for supercapacitors.

In addition to aerogels, cellulose-derived carbon *xerogels* and *cryogels* are also known [71]. Their preparation included dissolution, gelation, and subsequent drying. The internal surface area of cellulose xerogels and cryogels varied from 700 to 850 $m^2 \cdot g^{-1}$, and the volume of pores was 0.3 $mL \cdot g^{-1}$. The obtained materials can be applied for dye removal. Also, highly porous carbon aerogels were obtained by using bagasse as a raw material (Fig. 5.27) [72], carbonizing the freeze-dried bagasse aerogel. It was observed that the specific surface area, the pore size, and the distribution of the hierarchical porous carbon were affected by the activation temperature. The special hierarchical porous structure was attributed to the reaction between KOH (activator) and carbon in the aerogels during the activation process. The activation process occurred at a

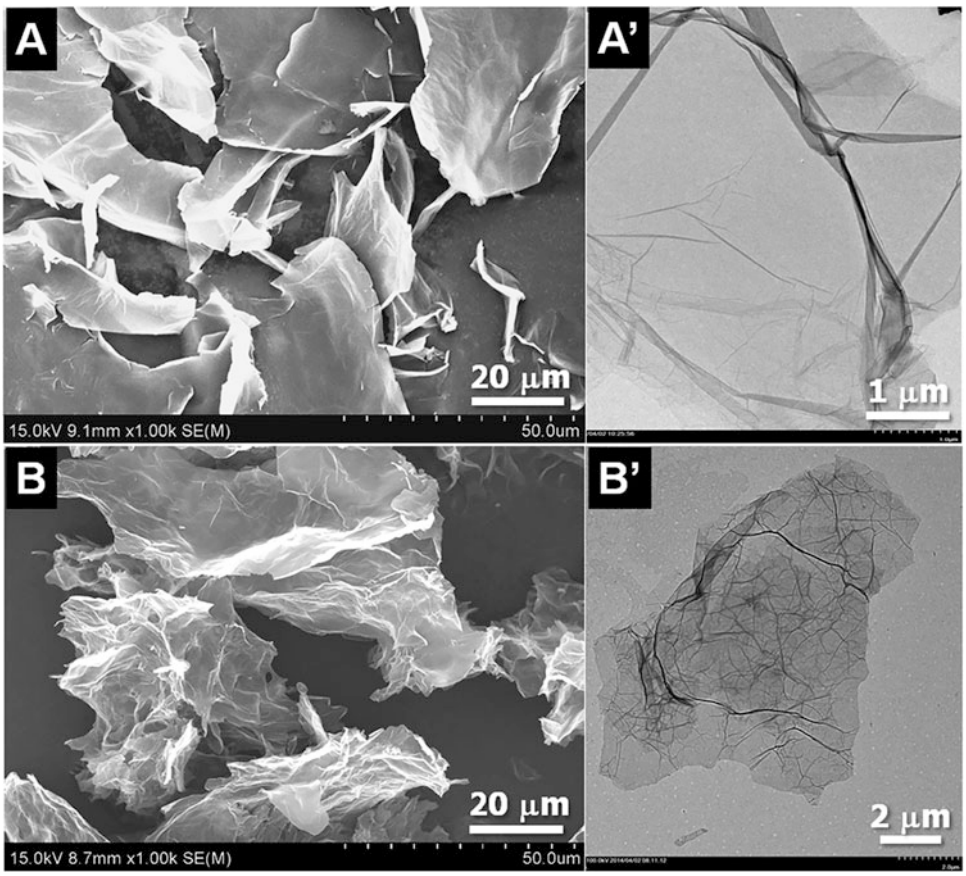

Fig. 5.24 Morphology of lyophilized GO sheets (**a**, **a**') and GO/PEI gel (**b**, **b**'). SEM images (**a**, **b**) and TEM images (**a**', **b**'). (Reproduced with permission of *Springer*)

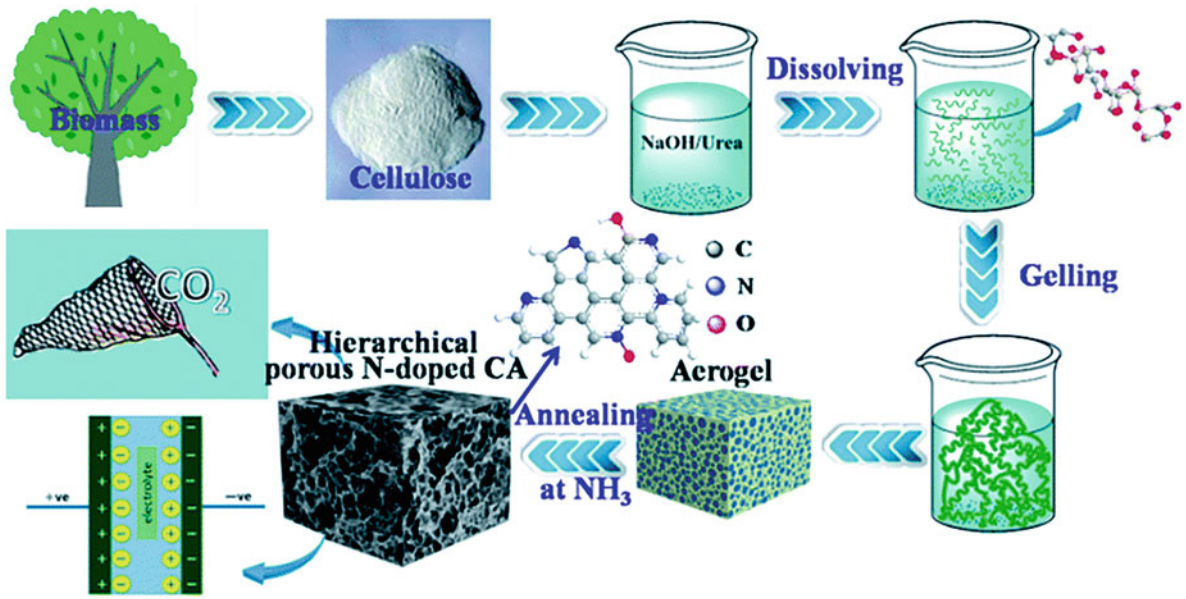

Fig. 5.25 Illustration of the preparations and applications of hierarchical porous N-doped carbon aerogel. (Reproduced with permission of the *Royal Society of Chemistry*)

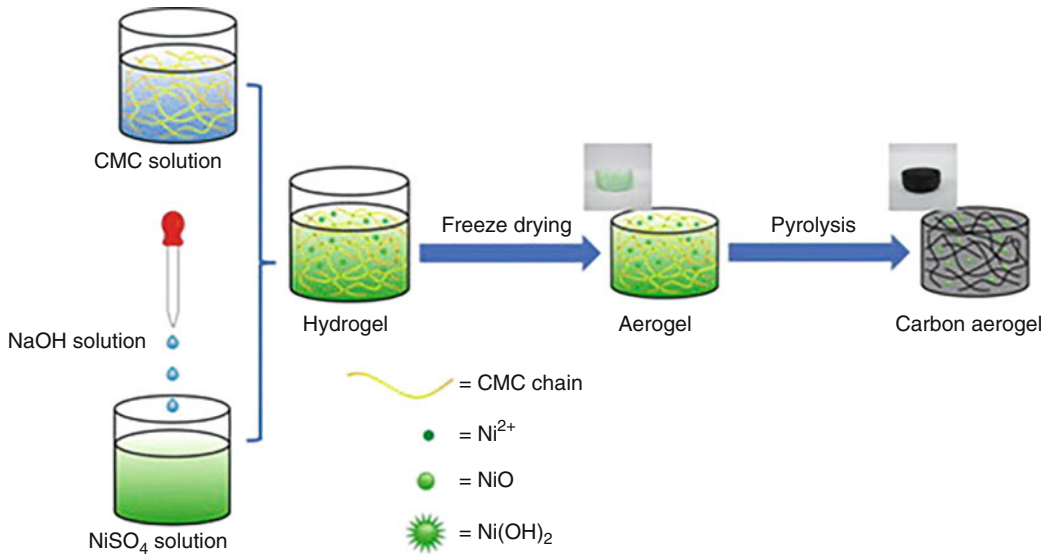

Fig. 5.26 Fabrication process of the CA/NiO composites. (Reproduced with permission of the *Elsevier Science*)

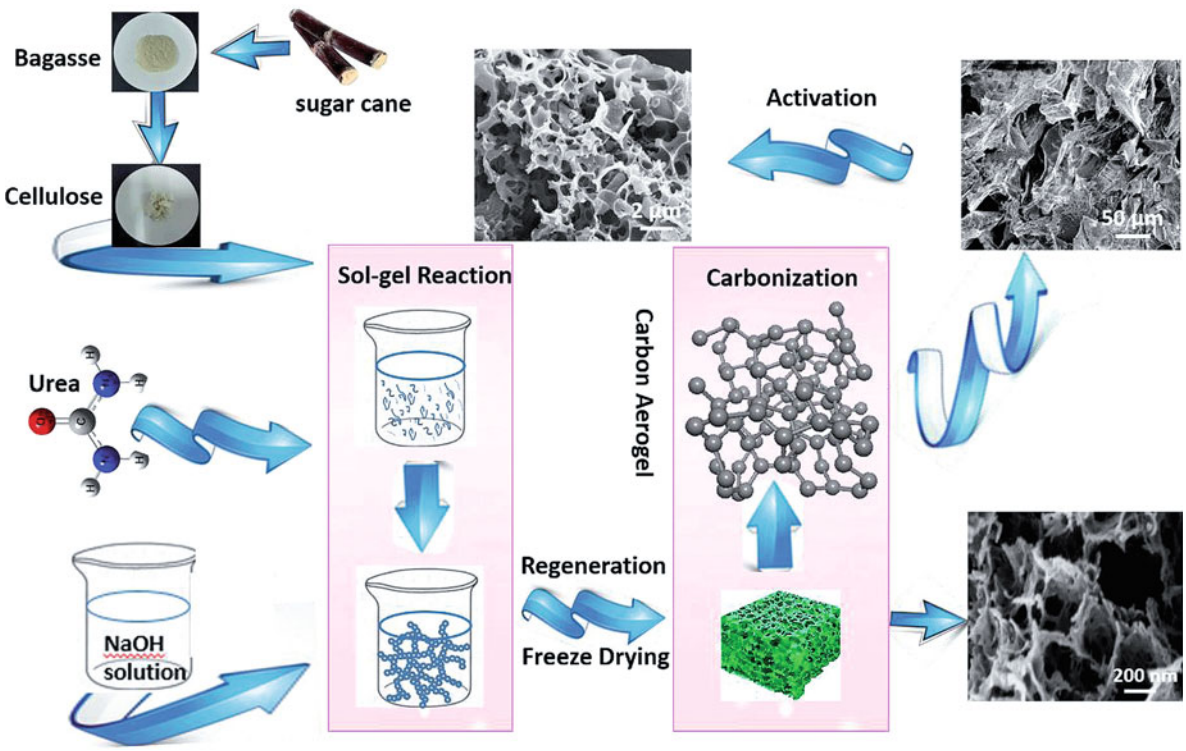

Fig. 5.27 Schematic of the fabrication of highly porous bagasse-derived carbon aerogels with hierarchical pore structure. (Reproduced with permission of the *Royal Society of Chemistry*)

high-temperature treatment of as-synthesized carbon aerogels and KOH penetrated in the pores of the carbon aerogels. At high temperatures, the reaction between carbon on the surface of the wall of the channels of the aerogels and KOH can occur according to the reaction 5.1. The high-energy storage ability of the hierarchical porous carbon was attributed to the specially designed pore structures, i.e., coexistence of the micropores and mesopores, showing an effective way to fabricate low-cost energy storage devices on the basis of carbon aerogels. On the basis of this aerogel, a two-electrode solid-state symmetrical supercapacitor device was assembled (Fig. 5.28).

$$4KOH + C \rightarrow K_2CO_3 + K_2O + 2H_2 \tag{5.1}$$

Coherent carbon cryogel–ammonia borane (C–AB) nanocomposites (Fig. 5.29) were synthesized by impregnation of carbon cryogels, derived from resorcinol–formaldehyde hydrogels, with AB in THF solution with a purpose to improve H_2 storage properties [73]. Carbon cryogels had a surface area of 300 m^2/g, a pore volume of 0.70 cm^3/g (57% open porosity),

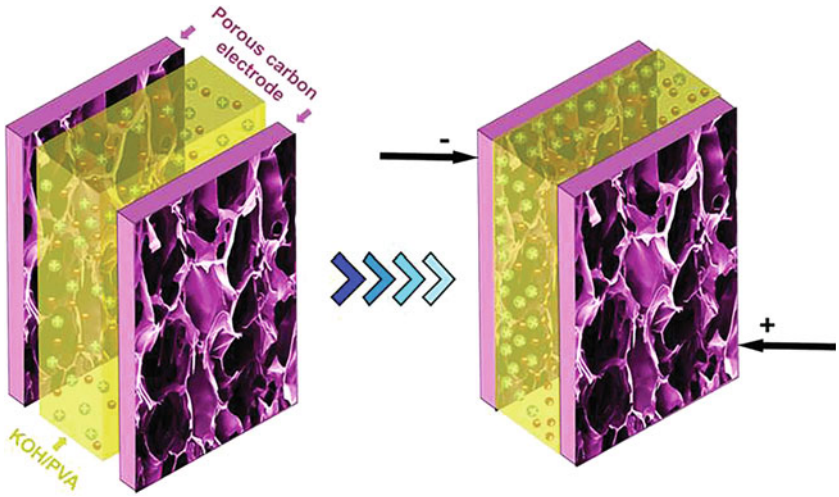

Fig. 5.28 Schematic of the fabricated hierarchical porous carbon supercapacitor. (Reproduced with permission of the *Royal Society of Chemistry*)

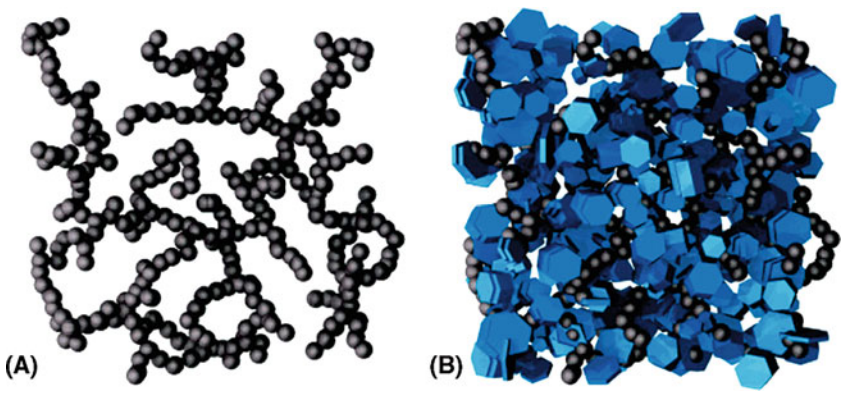

Fig. 5.29 Schematic of (**a**) an unmodified carbon cryogel and (**b**) a C–AB nanocomposite. (Reproduced with permission of the *American Chemical Society*)

and pores ranging from 2 to 20 nm in diameter. A merged two-step hydrogen release reaction with an appreciable reduction in the dehydrogenation temperature to <90 °C as well as the suppression of borazine release was observed. Overall hydrogen storage capacity was found to be dependent on both AB loading and the number of hydrogen molecules released from each AB molecule (a 13 wt. % hydrogen release from AB in the form of a nanocomposite was observed).

Carbon *xerogels* were synthesized from two different precursors, resorcinol and pyrogallol, and two different catalysts, Na_2CO_3 and H_2SO_4, through a series of procedures and final pyrolysis at 800 °C under a N_2 flow, and used as supports for Pt catalysts (3.5 nm in size of metal nanoparticles) for the application in polymer electrolyte fuel cells (ORR reactions) [74]. The capacity of the carbon xerogels for direct immobilization of metal complexes was tested with a manganese(III) *salen* complex which possesses an extended ligand π system and two reactive hydroxyl groups on the aldehyde fragment [75]. It was suggested that complex immobilization took place preferably by covalent bond between the surface oxygen functional groups and the ligand reactive groups, rather than by π–π interactions. The size and shape of the carbon xerogel pores were also shown to play an important role in the final loading of the manganese(III) *salen* complex. The impact of solvent composition as well as inorganic salt content and type on the structure of carbon xerogels, derived from the sol–gel polycondensation of resorcinol with furfural in a water–methanol–inorganic salt (NaCl, NH_4ClO_4, and $FeCl_3$) solution, was investigated [76]. Inorganic salts were removed prior to carbonization. It was revealed that a significant amount of salt can be introduced to the gel network of the desired structure. The samples derived from mixtures with $FeCl_3$ manifested well-developed mesoporosity and depleted microporosity in comparison to samples prepared from mixtures with NaCl and NH_4ClO_4 (Fig. 5.30). Iron ions chemically bond to the xerogel matrix and cause its partial graphitization during the carbonization process, resulting in enhanced mesoporosity.

Xerogel-derived carbons are a special case. Thus, porous carbons can be prepared from metal–organic gel (MOG) template (Fig. 5.31), an extended metal–organic framework (MOF) structure. The target MOGs were first prepared by mixing aluminum nitrate and 1,3,5-benzentricarboxylic acid in ethanol solutions, dried in air or by supercritical CO_2, resulting in MOXs and MOAs, respectively, and then carbonized to construct the target porous carbon products, named as MOX-C and MOA-C, respectively. The carbon products inherit the highly porous nature of MOF and combine with gel's integrated

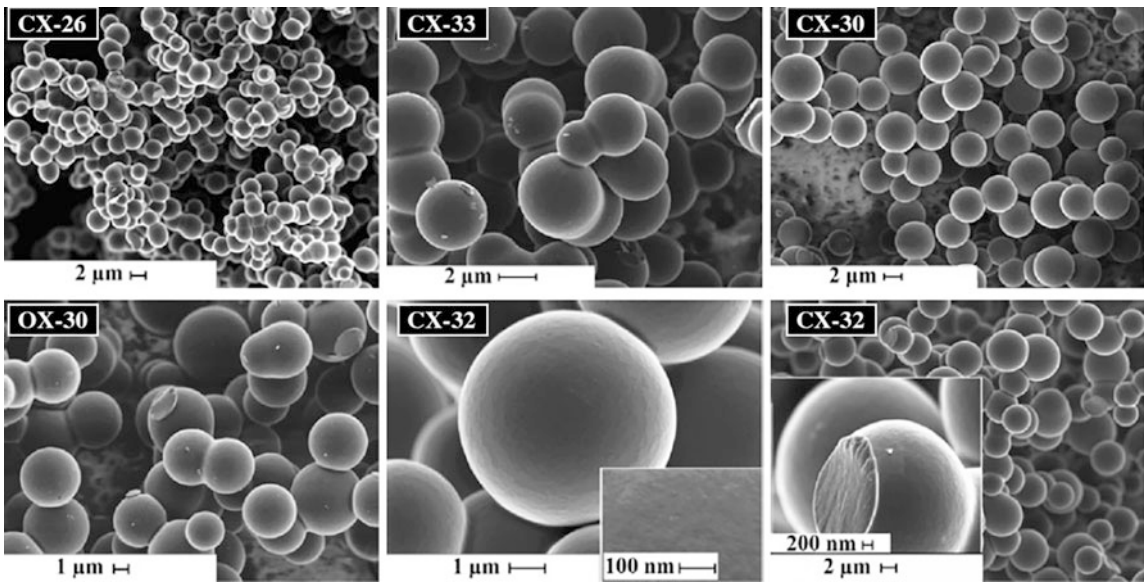

Fig. 5.30 SEM images of organic and carbon xerogels derived from mixtures with NH_4ClO_4. Magnified pictures of CX-32 show exclusively microporous structure inside the carbon spheres. (Reproduced with permission of *Springer*)

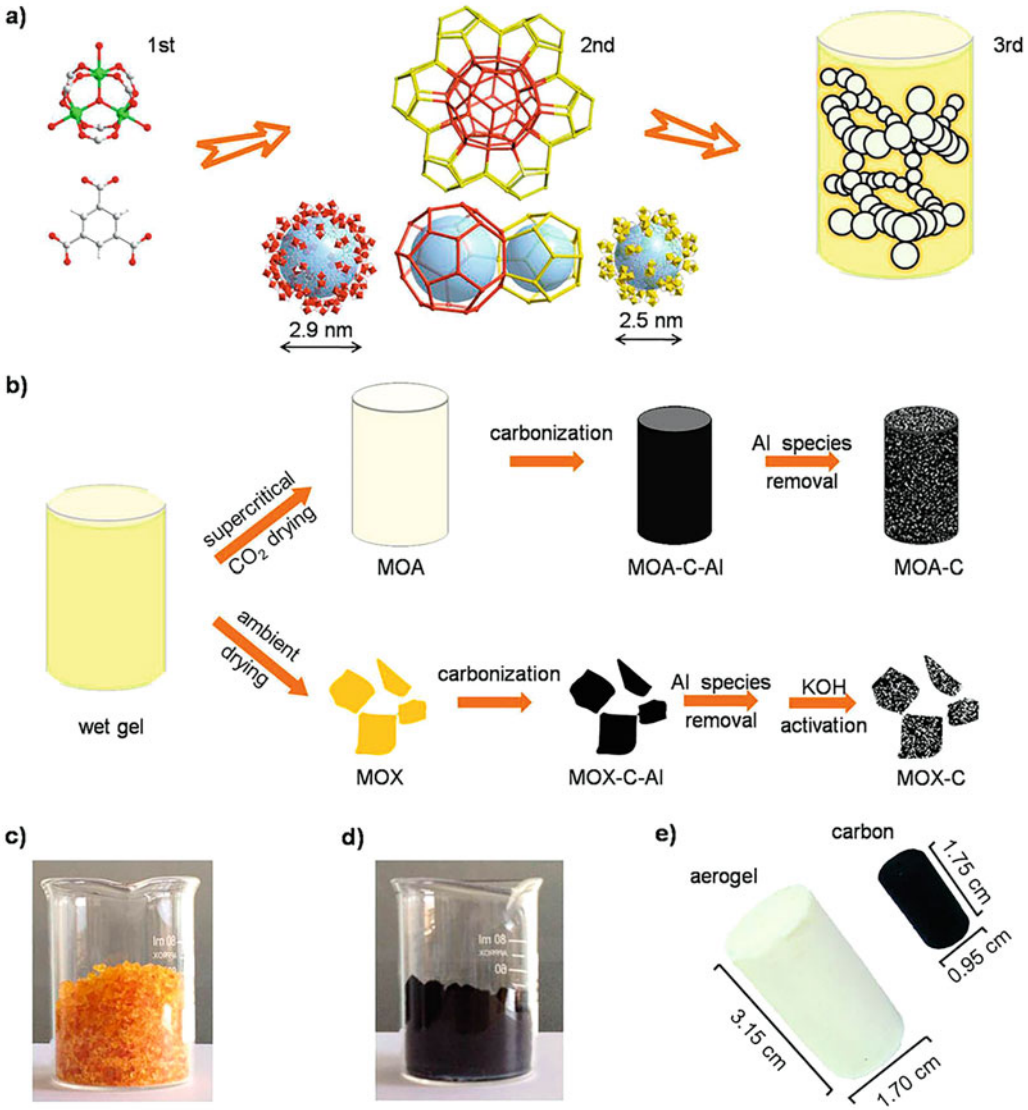

Fig. 5.31 Fabrication of porous carbon materials from Al-based metal–organic gels. (**a**) Schematic illustration of the gel structure, (**b**) typical synthesis procedure of the porous carbon products, (**c**, **d**) photographs of as-made xerogels (bulk density: 0.5612 g cm^{-3}) and their derived carbon products MOX-C (0.1185 g cm^{-3}), and (**e**) photograph of an integrate aerogel monolith (0.1189 g cm^{-3}) and its derived carbon product MOA-C (0.0952 g cm^{-3}). (Reproduced with permission of *Nature*)

character, which resulted in hierarchical porous architectures with ultrahigh surface areas, quite large pore volumes [77] and can be applied in processes for energy storage. The xerogel-derived carbon exhibited a very high surface area and hydrogen storage capacity, while the aerogel-derived carbon monolith has a hierarchical pore structure with micro-, meso-, and macropores and quite large pore volume, which is quite suitable for Li–S batteries.

5.4 Carbide-Derived Carbon

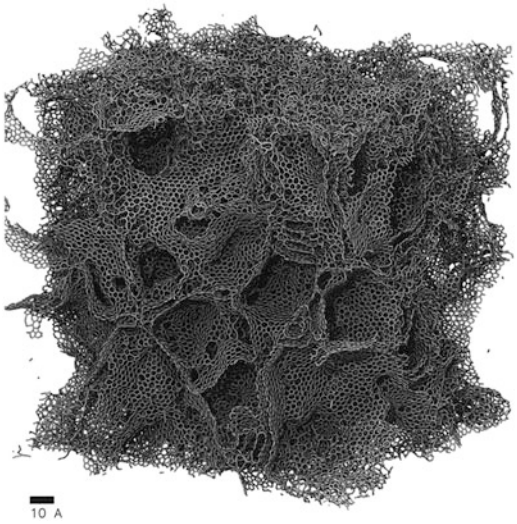

The field of carbide-derived carbon (CDC,[8] also known as tunable nanoporous carbon [78]) is a young, wide, and very important research area, which is being developed and comprehensively generalized mainly by research group of *Gogotsy* et al. [79–85]. This is indeed not the only carbon phase, but a variety of carbon allotropes, which can be formed starting from metal carbides as precursors via physical (e.g., thermal decomposition) or chemical (e.g., halogenation) processes. In addition to classic carbides (binary (e.g., SiC, TiC) or ternary carbides (e.g., Ti_2AlC, Ti_3SiC_2)), the CDCs can also be derived [86] from polymer-derived ceramics, such as Si–O–C or Ti–C, and carbonitrides, such as Si–N–C.

CDCs can occur in various structures, ranging from amorphous to crystalline carbon, from sp^2- to sp^3-bonded, and from highly porous to fully dense. These phases, depending on experimental conditions (for instance, addition of hydrogen into the reaction mixture of Cl_2–Ar), could be carbon nanotubes, fullerene- or onion-like nanostructures, nanocrystalline graphitic carbon, amorphous carbon, nanodiamonds, etc. (Fig. 5.32), i.e., many carbon allotropes can be obtained this way changing methods and reaction conditions. For CDC nomenclature purposes, specific terms like OM-SiC-CDC (OM is ordered mesoporous carbide precursors) are recommended to be used, since they clearly indicate the precursor and not just the resulting structure.

Synthesis methods for CDC include the treatment of carbides with chlorine (*chlorination technique*) at high temperatures (about 1000–1200 °C, although broader temperature ranges as 200–1200 °C were reported [87]), vacuum decomposition, and leaching in supercritical water, among others. In case of chlorination of carbides, the following simplified reaction 5.2 takes place. The chlorine-based synthesis of CDCs may be considered [88] to be a *nanocasting method* (i.e., a multistep technique which basically consists of the carbonization of an organic precursor in the nanospace of an inorganic material, which acts as a template), as the rigid metal carbide lattice acts as a template, with the metal atoms extracted layer by layer, so that the final carbon structure is templated by the carbide structure (Fig. 5.33). CDC membranes can be also obtained applying the chlorination method above. Thus, the Cl_2 treatment of a TiC thin film deposited onto a macroporous ceramic substrate by a magnetron sputtering technique at 350 °C led to the active carbon layer of ~500 nm in thickness with an amorphous carbon structure (Figs. 5.34 and 5.35) [89], showing a route to design highly efficient application-specific carbon membranes.

$$MC + x/2Cl_2 = MCl_x + C\ (M = Si, Ti, Zr, Nb; t = 450 - 950^oC) \tag{5.2}$$

The interaction mechanism of MC and Cl_2, as well as reaction products and pore size distribution, could depend on temperature, as well as their applications. For example, CDC produced at 600–800 °C show great potential for energy-related applications. In general, an initial carbide structure influences on the final CDC microstructure (a complex shape of formed CDC could be maintained). In particular, it was noted that, under the same processing conditions, the CDC prepared from Ti_3SiC_2 has a disordered network of graphite ribbons, meanwhile CDC from SiC revealed an amorphous structure. Surface area and microstructure of CDC also depend on catalysts used (e.g., Co, Ni, and Fe chlorides), halogen (chlorine, bromine,

[8]The image above is reproduced with permission of *Wiley* (*Advanced Science*, **2017**, *4*(7), 1700059).

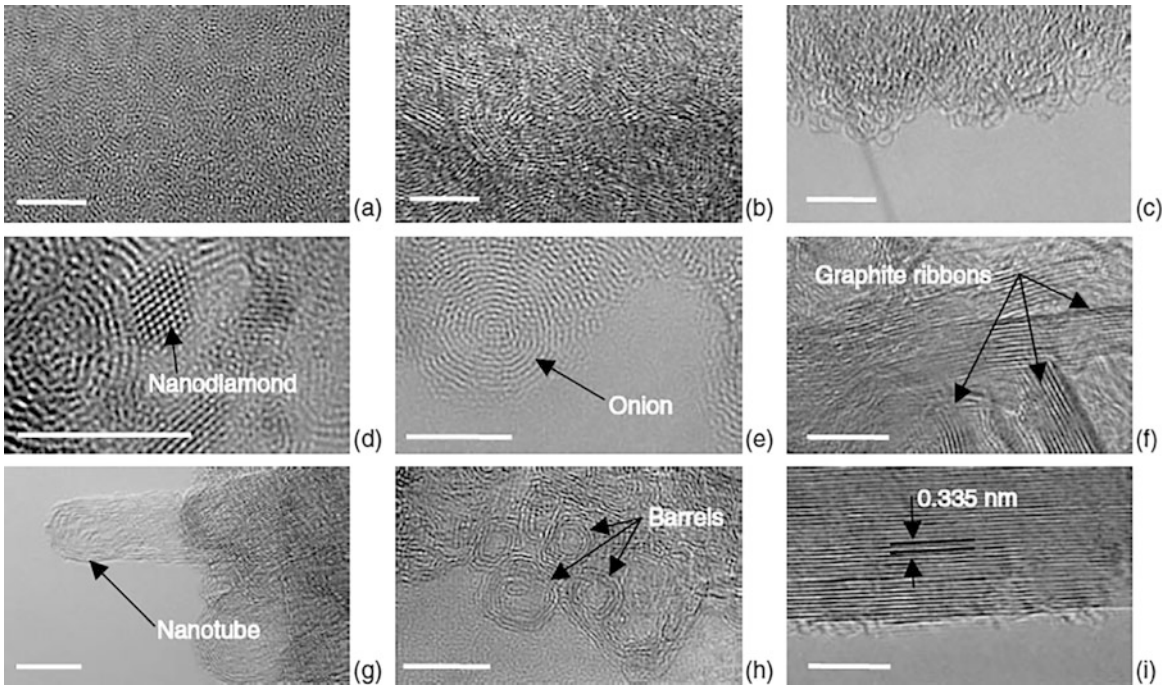

Fig. 5.32 High-resolution TEM images of various carbon structures produced by chlorination of carbides: amorphous carbon (**a**), turbostratic graphite (**b**), fullerene-like carbon (**c**), nanodiamond (**d**), carbon onion (**e**), graphite ribbons (**f**), CNTs (**g**), barrel-like particles (**h**), and ordered graphite. Scale bar, 5 nm. (Reproduced with permission of *Taylor & Francis* (Yushin et al. [79]))

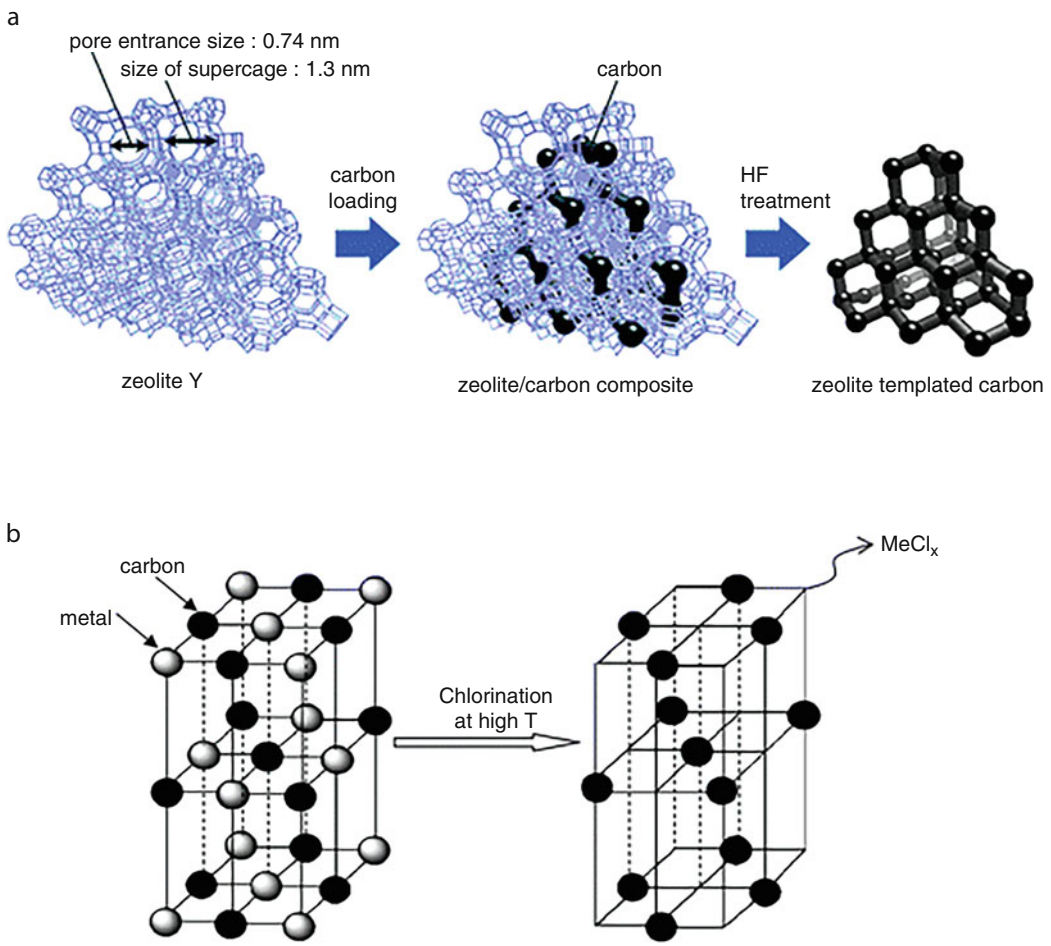

Fig. 5.33 Schematic illustration of (**a**) the carbon nanocasting technique using zeolite Y as template and (**b**) the selective high-temperature chlorination of a metal carbide lattice with a fcc structure (such as TiC and ZrC). (Reproduced with permission of the *Royal Society of Chemistry*)

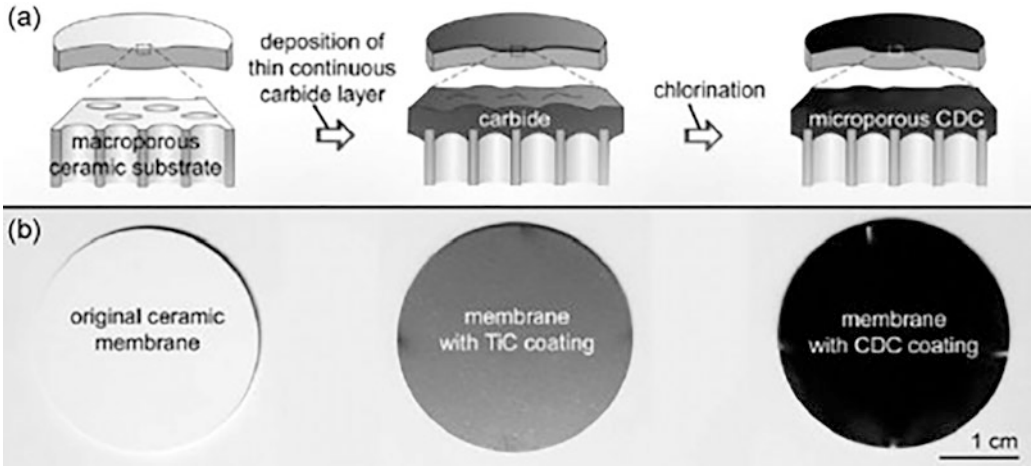

Fig. 5.34 CDC thin film formation: (**a**) schematic of the process flow, (**b**) optical images of the thin film at the corresponding processing stages. (Reproduced with permission of the *Elsevier Science*)

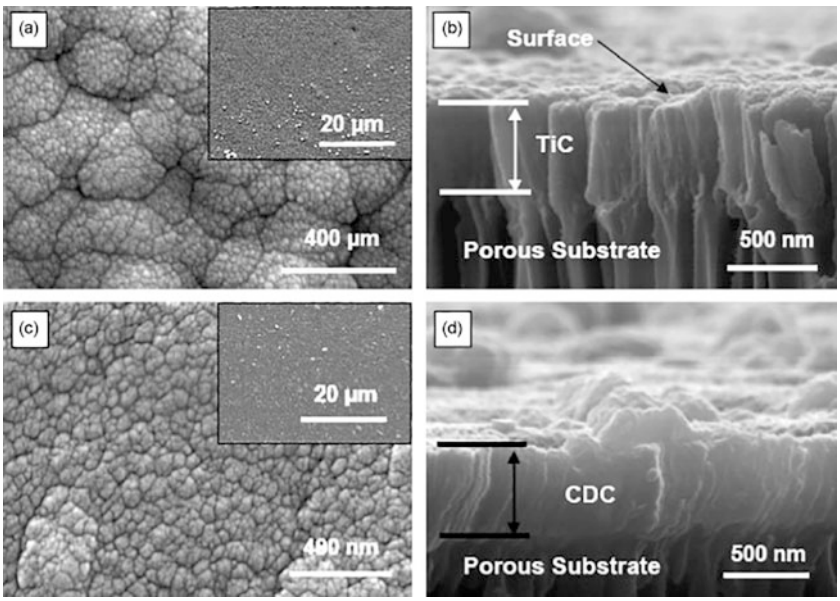

Fig. 5.35 SEM micrographs of TiC coating on an Anodisc substrate before (**a**, **b**) and after (**c**, **d**) chlorination: (**a**) coating top view and (**b**) cross section of the membrane depicting the substrate pores completely covered by ~500 nm TiC layer, (**c**) top view and (**d**) cross section of the produced CDC coating. (Reproduced with permission of the *Elsevier Science*)

and iodine), or initial carbide porosity. Posttreatments of TiC-CDCs, formed by chlorination method, at 600 °C in Ar, H_2, or NH_3 atmosphere were recommended for chlorine removal, indicating more effective results for the last two gases [90]. Other techniques are also applied for preparation of CDCs; one of them is the reaction of CaC_2 with inorganic salts at high temperatures for 1–5 h (reactions 5.3, 5.4, 5.5, and 5.6):

$$CaC_2 + MgCl_2 = MgC_2 + CaCl_2 \tag{5.3}$$

$$2MgC_2 = Mg_2C_3 + C \tag{5.4}$$

$$Mg_2C_3 = 2Mg + 3C \tag{5.5}$$

or

$$CaC_2 + 2NaCl = 2C + 2Na + CaCl_2 \tag{5.6}$$

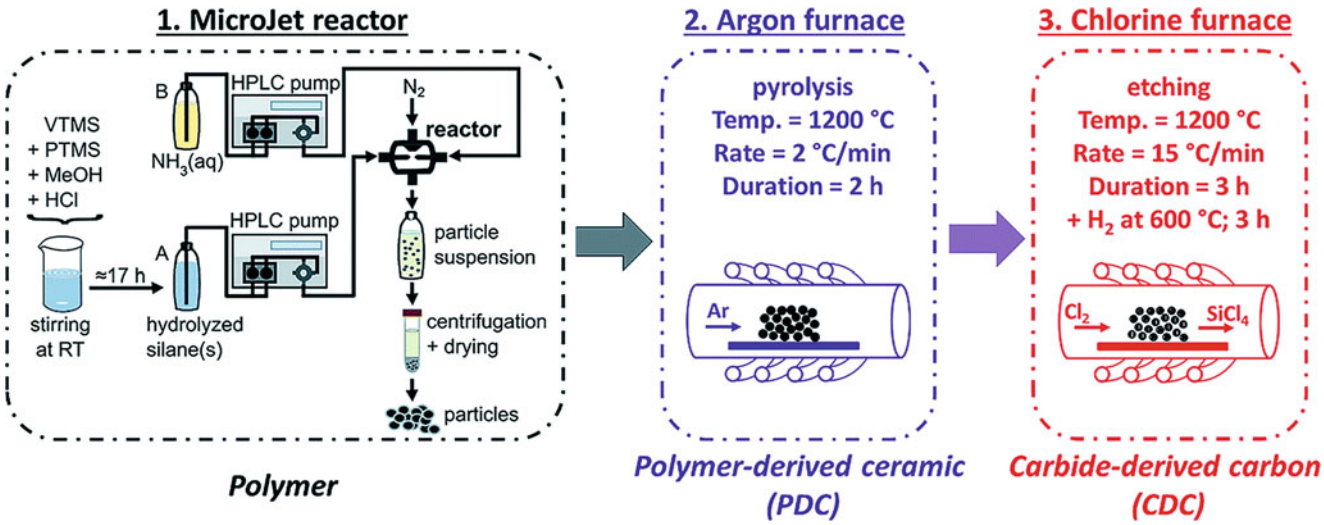

Fig. 5.36 Schematic overview of the synthesis method: (1) the production of the polymer beads with the MicroJet reactor, (2) the pyrolysis, and (3) the chlorine treatment. *VTMS* vinyltrimethoxysilane, *PTMS* phenyltrimethoxysilane, *MeOH* methyl alcohol, *RT* room temperature (A and B) solution A or solution B, *HPLC* high-performance liquid chromatography. (Reproduced with permission of the *Royal Society of Chemistry*)

The MicroJet reactor technique (Fig. 5.36) was applied in the first step of CDC fabrication [91]. Intermediate silicon oxycarbides were used as precursors for CDC synthesis. Chlorine etching of PDC at high temperatures allowed removal of silicon and oxygen, resulting in formation of nanoporous carbon (Fig. 5.37) with yields of 2.2 mass % to 21.9 mass %. These yields, although are relevant for the economic efficiency to produce highly porous carbon materials, can be possibly improved by using organic functional groups with a higher amount of carbon, like naphthyl or anthracenyl groups, or considering the combination of the pyrolysis and chlorine treatment should be considered to improve the process. The high porosity of formed SiOC-CDCs is attractive for electrochemical energy storage with supercapacitors.

Hydrothermal reactions in the M_xC–nH_2O(g) system can also lead to CRDs (C, MeO_x, CH_4, CO_2, CO, and H_2 are the main products of these hydrothermal reactions 5.7, 5.8, 5.9, 5.10, and 5.11). The CDCs can be prepared by thermal- or laser-assisted decomposition of SiC too. Varying decomposition conditions, carbon nanotubes of distinct types (i.e., selective preparation of zigzag CNT form), or nano-onions can be obtained. No catalyst is required for the CNT development, in a difference with spray pyrolysis, where ferrocene is usually applied as a catalyst.

$$x/2\ \mathrm{MC} + x\mathrm{H_2O} = \mathrm{M}_{x/2}\mathrm{O}_x + x/2\ \mathrm{CH_4} \tag{5.7}$$

$$\mathrm{MC} + (x+1)\mathrm{H_2O} = \mathrm{MO}_x + \mathrm{CO} + (x+1)\mathrm{H_2} \tag{5.8}$$

$$\mathrm{MC} + (x+2)\mathrm{H_2O} = \mathrm{MO}_x + \mathrm{CO_2} + (x+2)\mathrm{H_2} \tag{5.9}$$

$$\mathrm{MC} + x\mathrm{H_2O} = \mathrm{MO}_x + \mathrm{C} + x\mathrm{H_2} \tag{5.10}$$

$$\mathrm{MO}_x + n\mathrm{H_2O} = \mathrm{MO}_x + n\mathrm{H_2O} \tag{5.11}$$

Metal atom can be selectively extracted not only at high temperatures (1000–1400 °C) using Cl_2 [92], as it is shown above, but also at much lower temperatures. Thus, using the ternary-layered carbides, Ti_3AlC_2, Ti_2AlC, and Ti_3SiC_2 (called as MAX phases), the *electrochemical method* (Figs. 5.38 and 5.39) placing them into HF, HCl, or NaCl solutions was applied for this purpose [93], resulting in predominantly amorphous CDC with high rates and a narrow distribution of micropores. (We emphasize that the substitution of classic high-temperature techniques by the electrochemical ones also allowed the preparation of carbon nanotubes in similar conditions [94–97].) Nanoporous TiC-CDC can be also synthesized by electrolysis of TiC powder in molten $CaCl_2$ at higher temperatures (850 °C, 48 h, applied constant voltage of 3.1 V, equipment is shown in Fig. 5.40) [98]. Thus produced TiC-CDC was found to be a mixture of amorphous carbon and ordered graphite phase with a highly degree of graphitization. Authors considered this method of TiC-CDC production as very attractive, in particular because it could serve for mass production of high-quality CDCs.

MD Simulations For silicon CDC, the effect of fluorine doping (at three different levels of fluorination, Figs. 5.41 and 5.42) on its hydrophobicity and the underlying barriers for adsorption and diffusion of water vapor and CO_2 in the fluorinated and

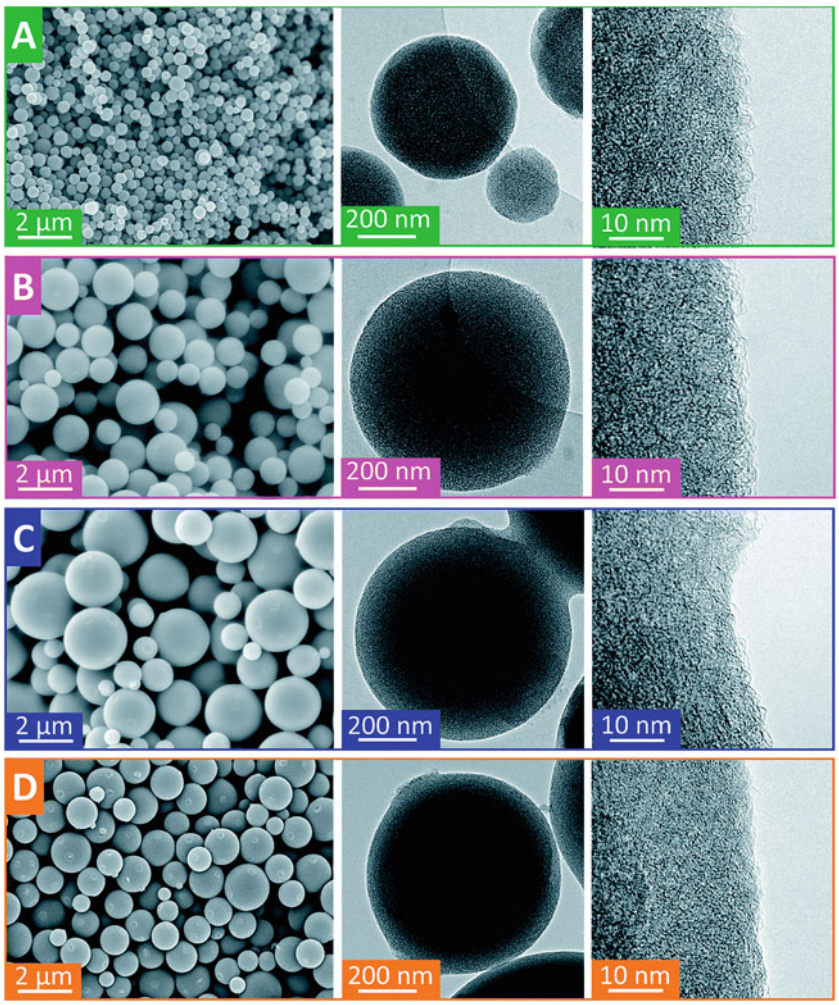

Fig. 5.37 Scanning and transmission electron micrographs of Vi-SiOC-CDC (**a**), $Ph_{0.25}Vi_{0.75}$-SiOC-CDC (**b**), $Ph_{0.5}Vi_{0.5}$-SiOC-CDC (**c**), and $Ph_{0.75}Vi_{0.25}$-SiOC-CDC (**d**). (Polymer composites of polyorganosilsesquioxanes with different ratios of phenyl (Ph) and vinyl (Vi) functional groups were used). (Reproduced with permission of the *Royal Society of Chemistry*)

nonfluorinated structures were studied by calculation of activation energy barriers using MD simulations and analysis of the free energy map of the unit cells [99]. In particular, it was proved that while fluorination generates more hydrophilic carbon surfaces, they actually act as more hydrophobic structures due to enhanced energy barriers in the disordered network of microporous carbon. Fluorination decreases the pore volume, surface area, and mean pore diameter of SiCDC. Indeed, apparently dual effect of fluorination takes place: while fluorination generates more hydrophilic carbon surfaces, they effectively act as more hydrophobic structures. In addition, the fluorination leads to reduction of CO_2 uptake.

Current and possible applications of CDCs include their uses as molecular sieves, sorbents for gas chromatography, soil detoxification, dehumidification, catalysis (as supporting materials), long-cycle supercapacitors, graphene-based electronic devices, hydrogen and methane [100], (natural gas) storage,[9] removal of toxins and cytokines from human blood, tribological coatings, purification of noble gases, manufacturing of CDC electrodes, capacitive water desalination, powerful selective sorbent for various molecules (in particular, proteins) or CO_2 [101], and actuator materials [102], among others. Here we show below selected representative applications of CDCs. Thus, in respect of CO_2 adsorption mentioned above, a series of CDCs with different surface oxygen contents were prepared from TiC powder by chlorination and followed by HNO_3 oxidation [103]. It was shown that the oxidation process led to an increase in *CO_2 adsorption capacity* of the porous carbons; the adsorbability of the CDCs is not directly associated with its microporosity and specific surface area. It was also found that the

[9]For example, the hydrogen storage at ambient pressure for TiC-CDCs varied from 1.4 wt.% to 2.8 wt.%. The highest methane uptake was 46 cm^3/g (3.1 wt.%) at 25 °C and atmospheric pressure (*carbon*, **44**(12), 2489–2497 (2006)).

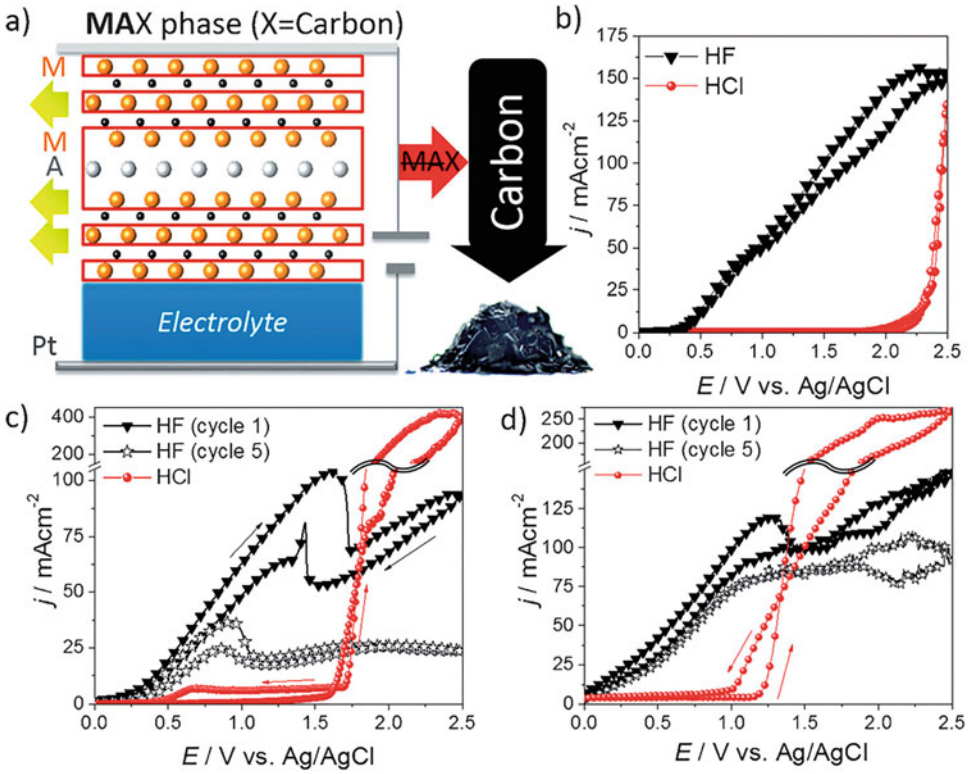

Fig. 5.38 (**a**) Schematic representation of the room-temperature CDC synthesis from MAX phase. (**b–d**) Cyclic voltammograms obtained in HF (green) and HCl (circles) when (b) Ti_3SiC_2, (c) Ti_3AlC_2, and (d) Ti_2AlC were used as anodes. For the case of HF, cycles 1 (triangles) and 5 (stars) are shown. (Reproduced with permission of the *Wiley*)

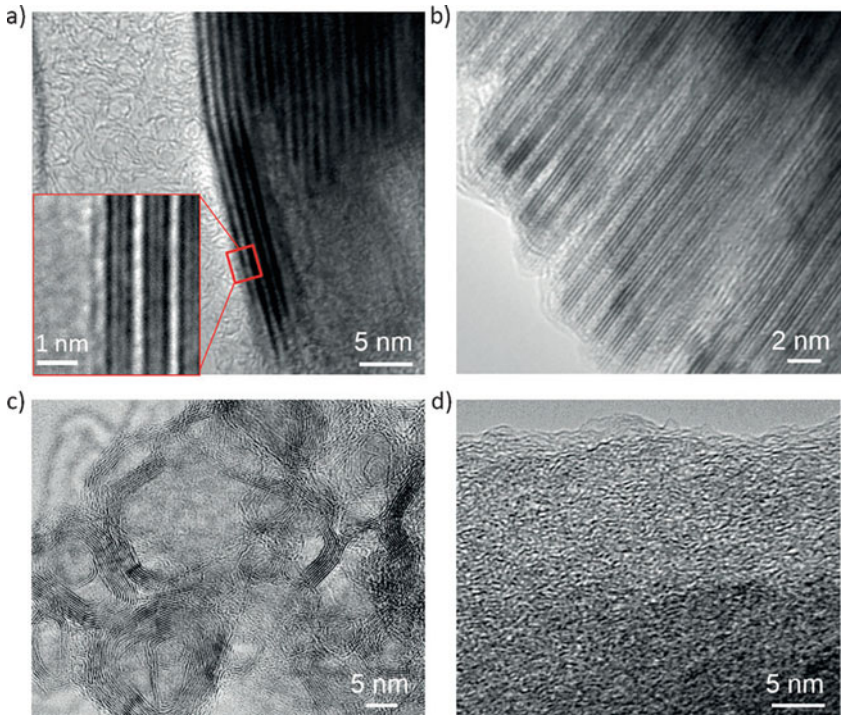

Fig. 5.39 TEM micrographs of CDCs produced by electrochemical etching of Ti_3AlC_2 in 5 wt.% HF. (**a**) CDC/Ti_3AlC_2 interface region. Inset shows a higher magnification of the area confined by the rectangle. (**b**) Same as (**a**) but at a higher magnification. (**c**) Ordered and (**d**) amorphous CDC structures. (Reproduced with permission of the *Wiley*)

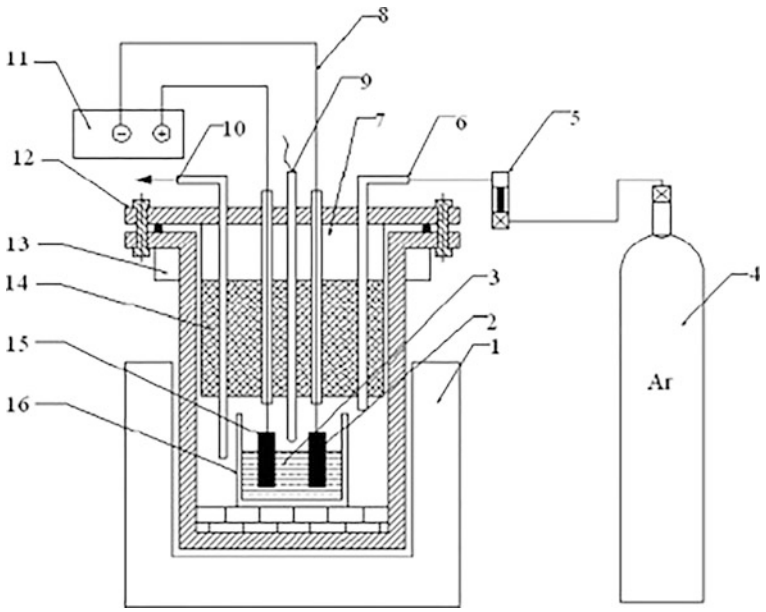

Fig. 5.40 The schematic configuration of the equipment: (1) electric furnace, (2) cathode, (3) molten salt, (4) Ar gas, (5) flow meter, (6) Ar gas inlet, (7) cooling water, (8) electrode extension, (9) thermocouple, (10) Ar gas outlet, (11) regulated DC power source, (12) reactor, (13) cooling water, (14) thermal insulation layer, (15) anode, and (16) corundum crucible. (Reproduced with permission of the *Elsevier Science*)

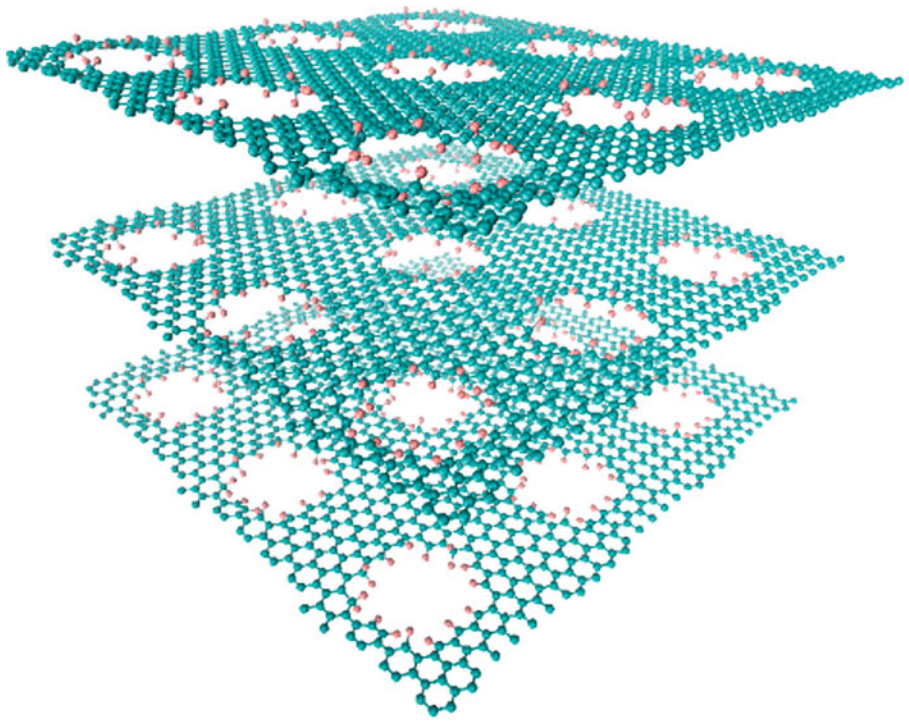

Fig. 5.41 Fluorinated sheet of graphene with embedded defects in the form of pores. (Reproduced with permission of the *American Chemical Society*)

introduction of O atoms into the carbon surface facilitates the hydrogen bonding interactions between the carbon surface and CO_2 molecules. Presence of hydrogen bonding interactions between the carbon in CDC-50 and CO_2 molecules were proved by FT-IR spectra (Fig. 5.43) in both N_2 and CO_2 atmospheres.

CDCs with incorporated highly dispersed nanoparticles transition metal nanoparticles (2.5 nm; Ru, Pd, Pt nanoparticle sizes can be controlled by changing the microemulsion composition) were prepared (Figs. 5.44 and 5.45) using a

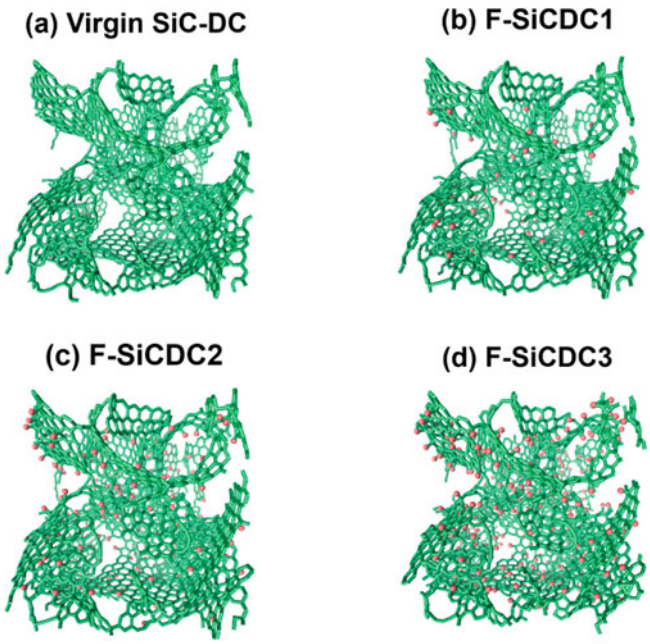

Fig. 5.42 Virgin and fluorinated models of SiC-DC. (**a**) Virgin SiC-DC, (**b**) F-SiCDC1, (**c**) F-SiCDC2, (**d**) F-SiCDC3. (Reproduced with permission of the *American Chemical Society*)

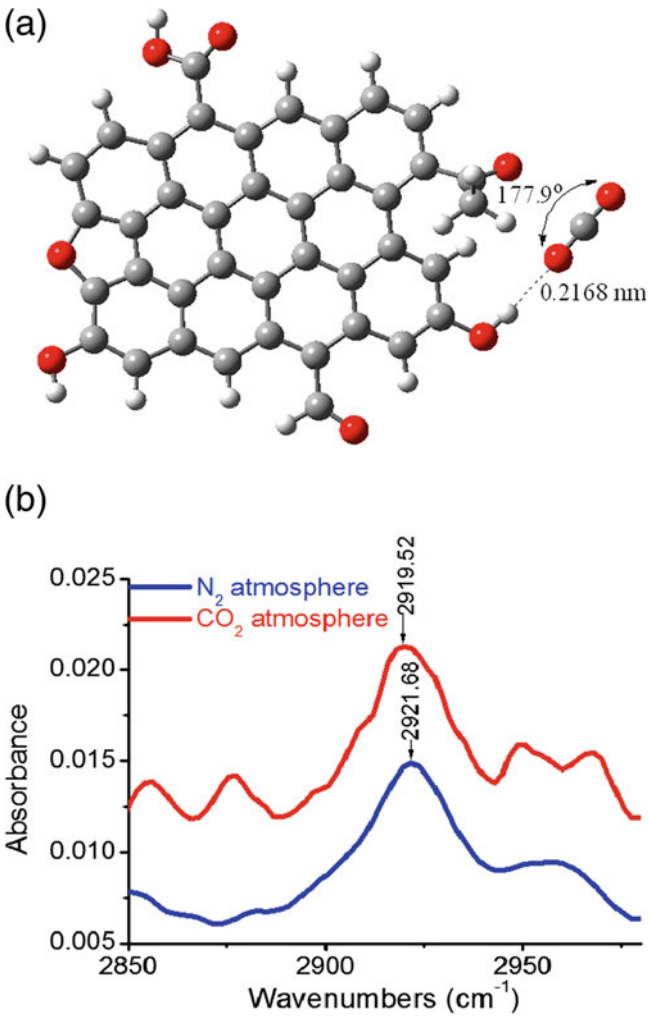

Fig. 5.43 Hydrogen bonding interaction and FT-IR spectra. (**a**) The interaction between the theoretical model of CDC surface and CO_2 molecule and (**b**) FT-IR spectra of CDC-50 measured under different atmospheres. (Reproduced with permission of the *Springer*)

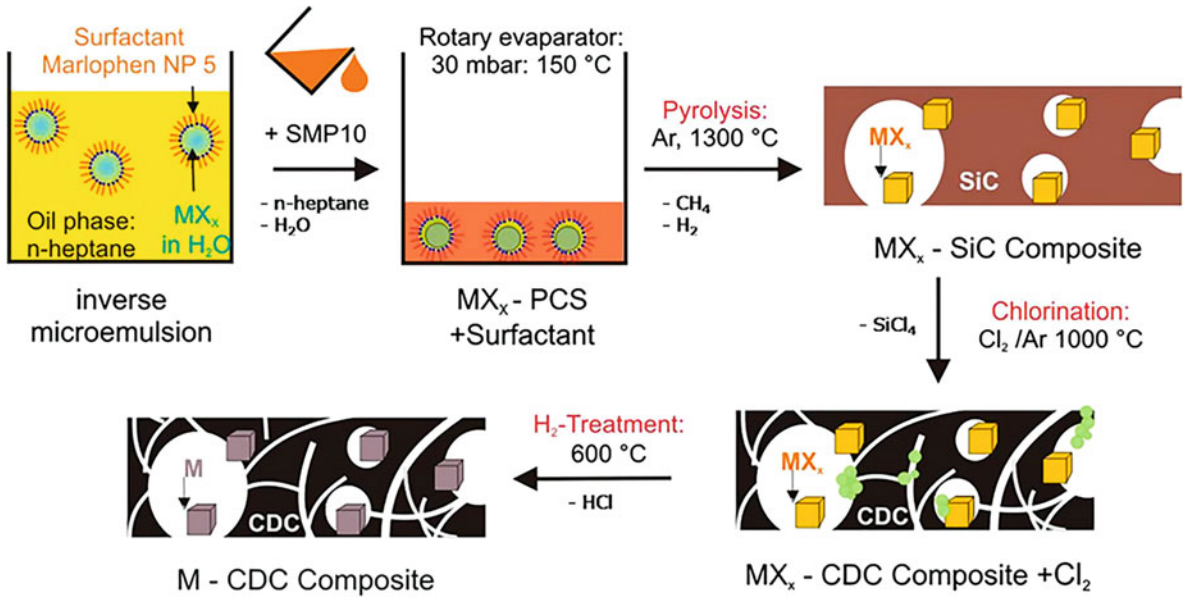

Fig. 5.44 Synthesis strategy for the preparation of metal containing polymeric PCS (M = Ru, Pd, Pt), ceramic SiC, and carbonaceous CDC composites synthesized by inverse microemulsion method, pyrolysis, chlorination, and hydrogen treatment, respectively. (Reproduced with permission of the *Elsevier Science*)

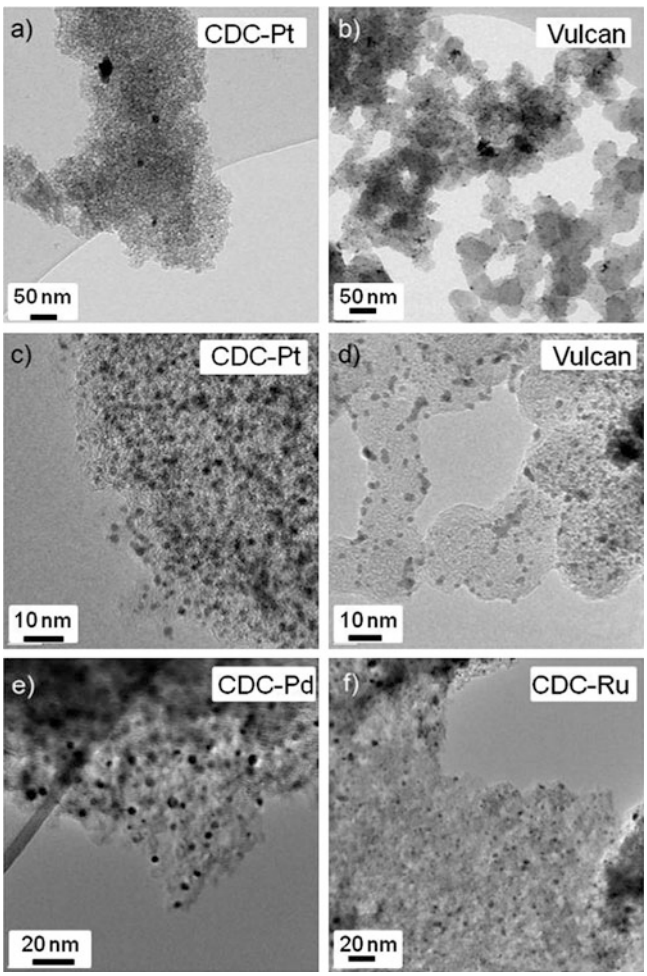

Fig. 5.45 TEM image for CDC–Pt catalyst (**a**) 50 nm scale, (**c**) 10 nm scale, commercial Pt/Vulcan XC 72R catalyst (**b**) 50 nm scale, (**d**) 10 nm scale, CDC–Pd catalyst, (**e**) 20 nm scale, and CDC–Ru catalyst (**f**) 20 nm scale. (Reproduced with permission of the *Elsevier Science*)

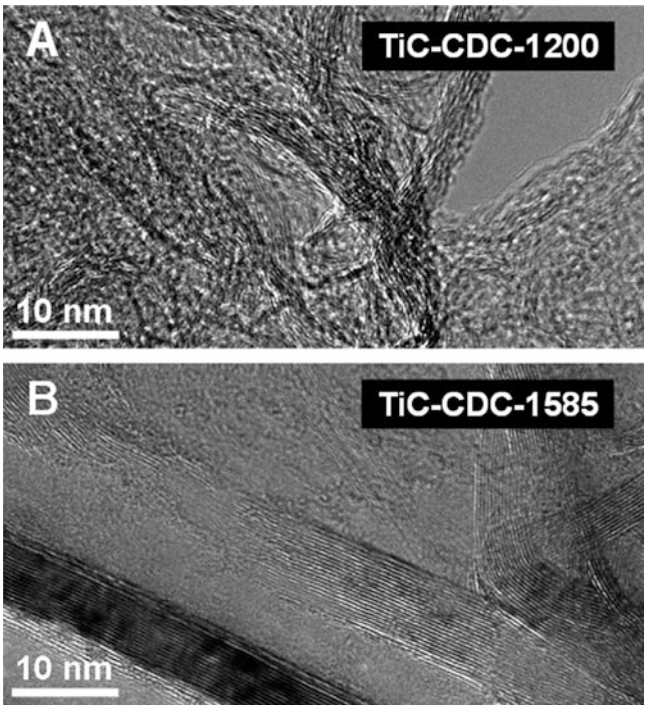

Fig. 5.46 TEM images of various samples of TiC-CDC. (**A, B**) TEM images of various samples of TiC CDC. (Reproduced with permission of the *American Chemical Society*)

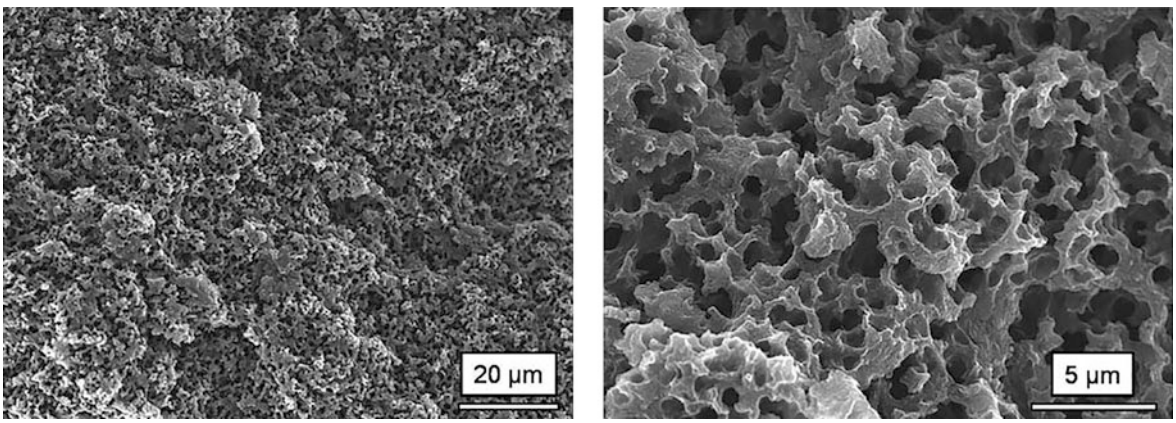

Fig. 5.47 SEM micrographs of the CDC monoliths. (Reproduced with permission of the *Royal Society of Chemistry*)

microemulsion approach [104]. It was found that the metal nature has a considerable influence on sorption properties of resulting metal–CDC composites, which were tested as heterogeneous catalysts for ORR (in the *partial oxidation of methane*). Pt-based material is a promising alternative support material for fuel cell cathode catalysts.

Mesoporous graphitic carbon powders with mean pore diameter of up to 8 nm, pore volumes of up to 0.90 $mL \cdot g^{-1}$, and graphite crystallite sizes exceeding 25 nm were synthesized on the basis of the reactive extraction of metal from titanium carbide [105] at 1300–1585 °C and used for *dehydrogenation of ethylbenzene* to styrene at 550 °C with exceptional styrene selectivities of up to 95%. High-temperature TiC-CDCs (Fig. 5.46) showed low deactivation and adequate oxidation stability; reactivation by burning deposited coke was found to be possible.

Uniform nanocomposites of Se and ordered mesoporous silicon CDC (OM-SiC-CDC) were fabricated by diffusing Se into the CDC pores at 260 °C and following heat treatment at 300 °C for 3 h studied as cathodes for *lithium–selenium (Li–Se) batteries* [106]. Se–CDC showed significantly better performance characteristics than Se-activated carbon nanocomposites with similar physical properties, better rate performance, and cycle stability, compared to S–CDC for Li/S batteries. CDC monoliths (CDC-Ms, Fig. 5.47) containing a multimodal arrangement with high volumes of micro-, meso-, and macropores were prepared by direct nanocasting of silica monoliths with polycarbosilane precursors [107] and used for *gas filtration*.

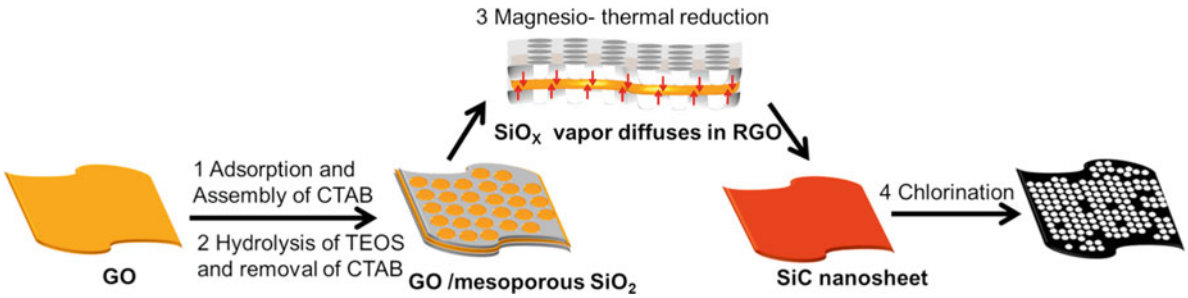

Fig. 5.48 Synthetic mechanism from 2D sandwiched SiO_2/C nanocomposites to SiC nanosheets and finally graphene-like CDCs: the self-assembling and hydrolysis (1 and 2) of CTAB/TEOS moieties at GO surface leading to 2D sandwiched SiO_2/GO nanosheets, the topotactic conversion as SiC nanosheets by magnesio-thermal reduction (3) thanks to SiO_x vapors diffusion into RGO layers, and the silicon oxidation/extraction by chlorination (4) opening micropores in corresponding graphene-like CDCs. (Reproduced with permission of the *Elsevier Science*)

Specific surface areas of >2600 $m^2\ g^{-1}$ and overall pore volumes as high as 3.14 $cm^3\ g^{-1}$ were detected. This material can be considered as advanced adsorbent for *the removal of volatile organic compounds* from gas mixtures. In addition to the CDC applications above, the field of supercapacitors remains to be attractive for the use of carbon allotropes. Thus, two carbide-derived carbons, CDC-Gs, were produced [108] by chlorination of graphene-like SiC nanosheets with conservation of graphene-like morphologies of carbide precursors. The synthesis mechanism is shown in Fig. 5.48. Evaluating them as *supercapacitor electrode materials*, a remarkable high-power capability with 76% of retention of the initial capacity at scan rates up to 3 V s^{-1} was revealed.

5.5 MOF-Derived Carbon

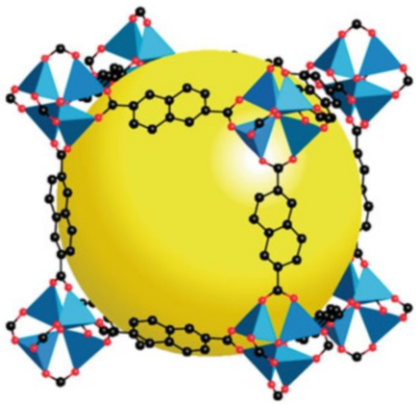

Metal–organic frameworks (MOF) are multidimensional nanoporous structures composed of metal ions (or clusters) coordinated to rigid organic molecules (linkers). The choice of the metal ion and linker species completely determines the structure and functionality of the resulting MOF. Common organic linkers include bidentate carboxylics (e.g., HOOC–COOH), tridendate carboxylates (e.g., $C_9H_6O_6$), 1,4-benzenedicarboxyalte (BDC), and azoles (e.g., $C_2H_3N_3$) molecules. The great freedom with which the linkers and metal ions can be chosen and combined is reflected in the more than 20,000 MOF species that have been reported in the last two decades. Numerous MOF composites have been prepared by assembling MOFs and functional species, including graphene and carbon nanotubes [109]. At the same time, the MOFs built from metal ions and polyfunctional organic ligands (Fig. 5.49) have proved to be promising self-sacrificing templates and precursors for preparing various carbon-based nanomaterials, possessing high BET surface areas, abundant metal/organic species, large pore volumes, and extraordinary tunability of structures and compositions [110]. In comparison with other carbon-based catalysts, MOF-derived carbon-based nanomaterials have great advantages in terms of tailorable morphologies, hierarchical porosity, and easy functionalization with other heteroatoms and metal/metal oxides, which make them highly efficient as catalysts (Fig. 5.50) directly or as catalyst supports for numerous important reactions. Among most recent reviews in this area, we note MOF-derived heteroatom-doped carbon-based electrocatalysts, including nonmetal (such as N, S, B, and P)- and metal (such as Fe and Co)-doped carbon materials [111]. In addition to the catalysis, as it will be seen below, the uses of MOF-derived

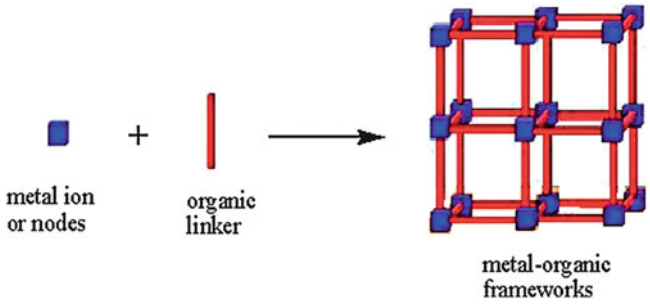

Fig. 5.49 Components and structure of MOFs. (Reproduced with permission of the *Royal Society of Chemistry* from Ref. [113])

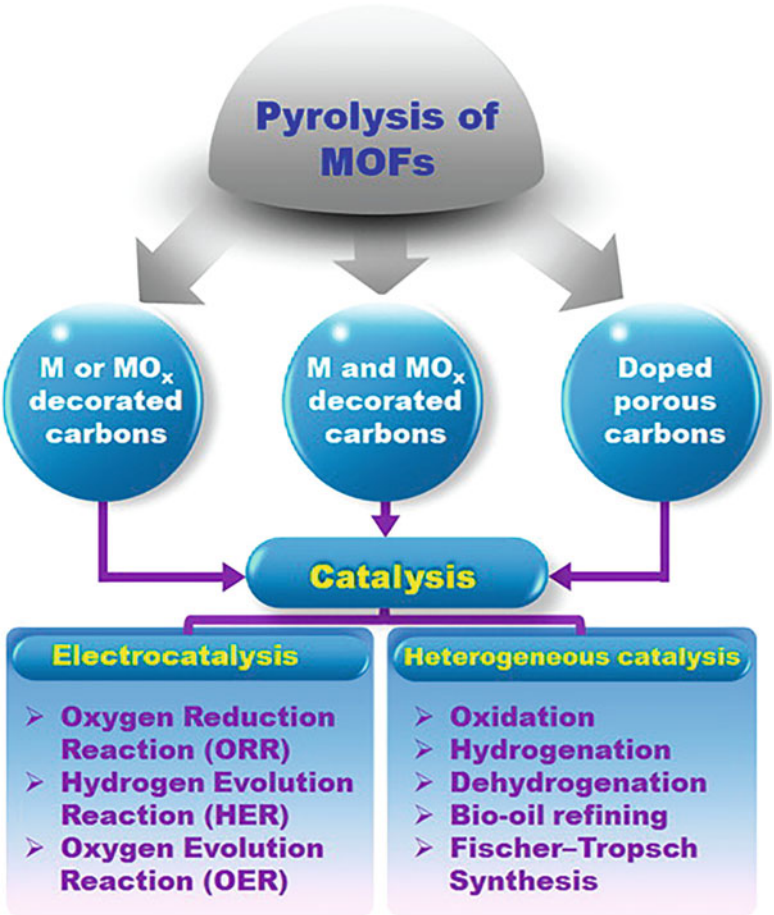

Fig. 5.50 Various carbon-based nanomaterials prepared by the pyrolysis of MOFs and their applications in numerous important reactions. (Reproduced with permission of the *American Chemical Society*)

carbons include other electrochemical applications, for example, for batteries. In whole, heat treatment of metal–organic frameworks, resulting MOF-derived carbons, belongs to green energy applications [112]. There are a lot of opportunities in creating novel metal-containing nanocarbons due to a variety of already existing multifunctional nanoporous MOFs (Fig. 5.51). In this section, we will examine most frequent Zn-, Co-, and Fe-containing MOFs, as well as some bimetallics.

For the fabrication of nanocarbons, we note that zinc-containing MOF precursors are obviously most common and represented mainly by MOF-5 and ZIF-8. As an example, five nanoporous carbons (pore size distribution about 3.9 nm) were prepared [115] by polymerizing and then carbonizing carbon precursor of furfuryl alcohol accommodated in a MOF-5, $[Zn_4O(bdc)_3]$, (bdc = 1,4-benzenedicarboxylate) template in a range of temperatures. The carbons obtained at higher temperature (about 1000 °C) were found to possess the best capacitor behaviors due to high mesoporosities and good

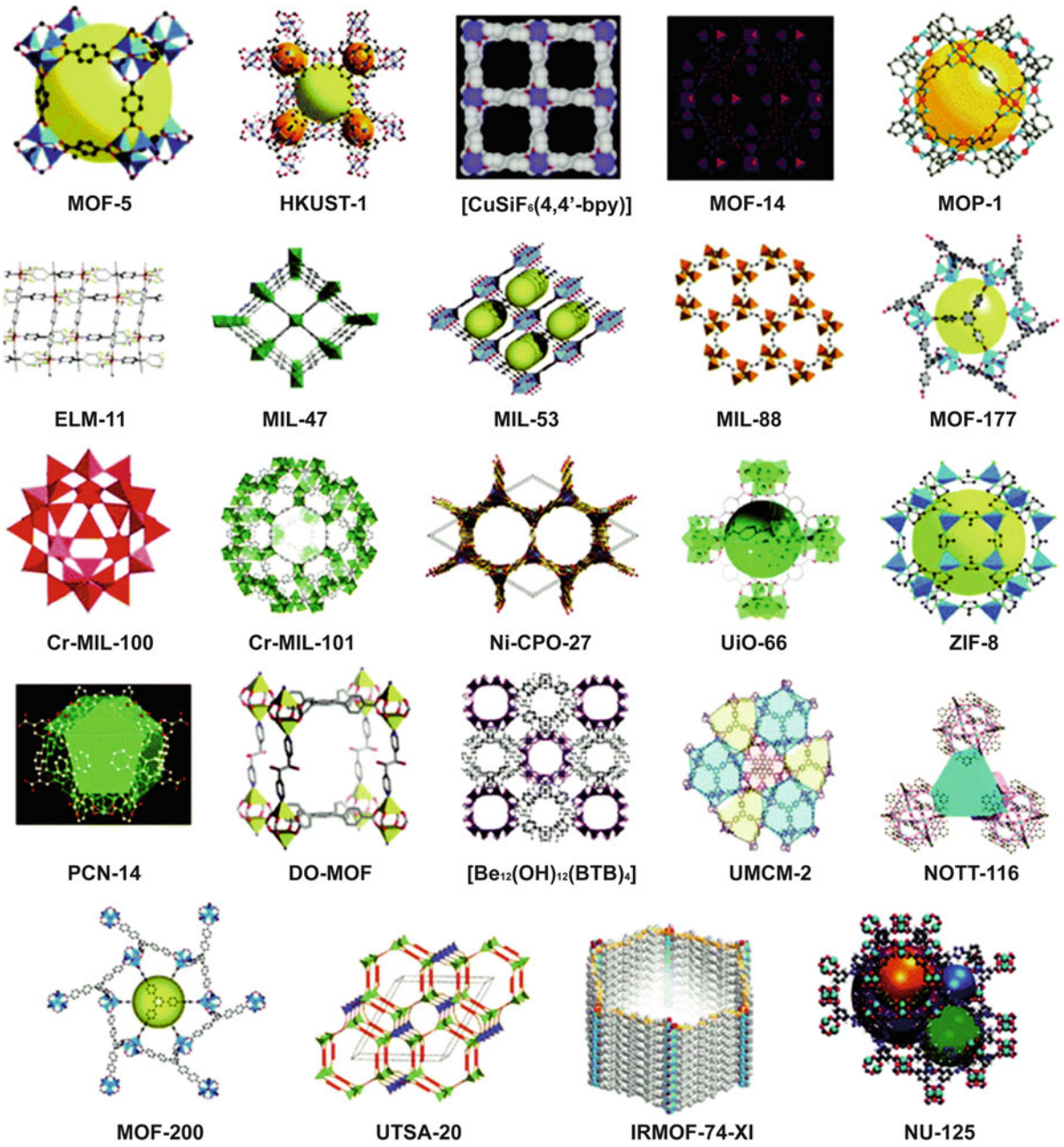

Fig. 5.51 Nanoporous structures of different MOFs. (Reproduced from [114] with permission from the *Royal Society of Chemistry*)

electrical conductivity, and those prepared at 530 °C showed poor electrochemical performance due to its poor electrical conductivity.

A variety of carbons have been obtained from the zeolitic imidazolate framework-8 (ZIF-8). Thus, nitrogen-rich porous carbons (NPCs), being the leading cathode materials for next-generation Zn–air and Li–S batteries, were prepared [116] by combining silica templating with in situ texturing of MOFs (Fig. 5.52; the design is based on combining silica templating with in situ N-generating and texturing of ZIF-8 as a self-template), showing crystal architecture of simultaneously record-high total pore volume (13.42 $cm^3 \cdot g^{-1}$), ultralarge surface area (2546 $m^2 \cdot g^{-1}$), and permeable hierarchical macro-meso-microporosity. In particular, the Zn–air battery reached a considerably high capacity of 770 $mAh \cdot g_{Zn}^{-1}$ at an unprecedentedly high rate of 120 $mA \cdot cm^{-2}$, with an ultrahigh power density of 197 $mW \cdot cm^{-2}$. Also, in situ synthesis of ZIF-8 following carbonization route was applied [117] (Fig. 5.53) to modulate the morphology of spherical activated carbon (SAC). The highly dispersed nanoparticles with the average size about 10.5 nm and bamboo-shaped carbon nanotubes (B-CNTs) with the average diameter

Fig. 5.52 (**a**–**c**) Schematic for the fabrication of bifunctional MOF-derived nitrogen-rich carbon photonic crystal architectures as cathode catalysts and sulfur host for Zn–air and Li–S batteries. (**d**) The corresponding structural colors of the silica photonic crystals (upper panel) and MOF-derived carbon photonic crystals (lower panel). (Reproduced with permission of *Wiley*)

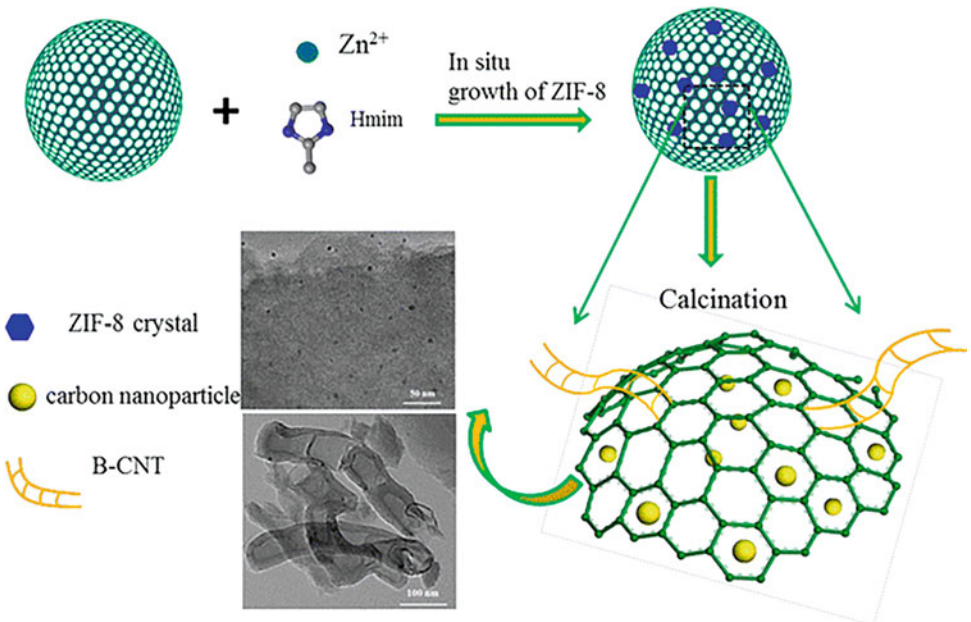

Fig. 5.53 Schematic illustration of the synthesis of ZIF-8/SAC composite. (Reproduced with permission of *Springer*)

of 40–80 nm appeared on the surface of the modified SAC. A superior catalytic performance toward acetylene hydrochlorination was observed, with the highest acetylene conversion of 81% and the selectivity to VCM above 99%, which was attributed to the formation of more active sites, which can efficiently access to the reactants of hydrogen chloride and acetylene in acetylene hydrochlorination.

A functional composite of ZnO nanoparticles embedded in N-doped nanoporous carbons was synthesized [118] by a one-step carbonization of ZIF-8 under a water stream atmosphere. It was noted that the introduction of water steam during the carbonization process holds the key to obtain the fine and homogeneously dispersed ZnO nanoparticles within the functionalized nanoporous carbon matrix. The composite exhibited a stronger interaction with CO_2 and was found to be more efficient to promote the photocatalytic degradation–adsorption of *methylene blue* under visible light than the composite

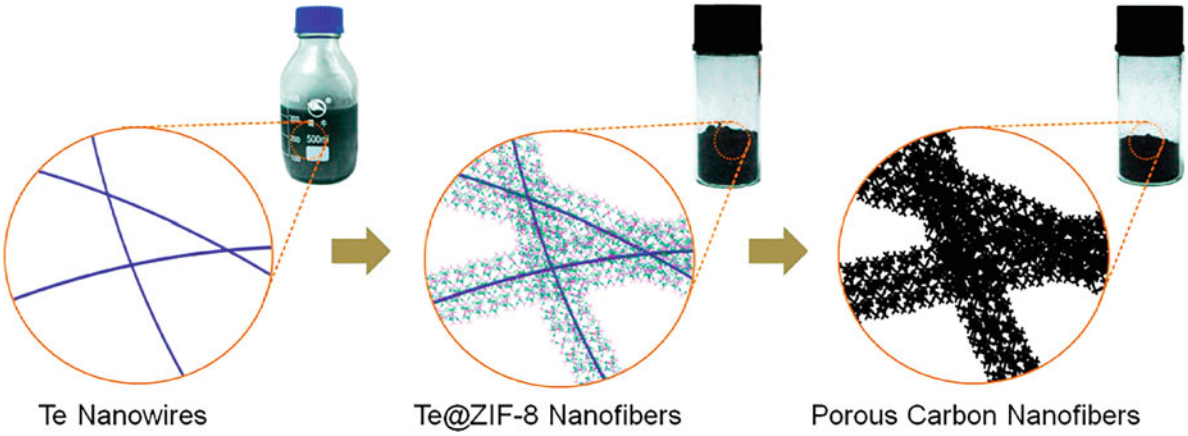

Fig. 5.54 Nanowire-directed templating synthesis of ZIF-8 nanofibers and derived porous doped carbon nanofibers. (Reproduced with permission of the *American Chemical Society*)

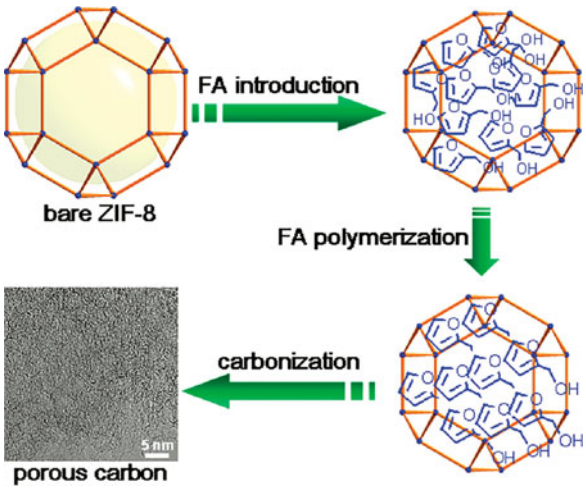

Fig. 5.55 Schematic illustration of the preparation procedure for nanoporous carbon (the cavity in ZIF-8 is highlighted in yellow). (Reproduced with permission of the *American Chemical Society*)

obtained without steam treatment. Highly porous doped carbon nanofibers (Fig. 5.54) were obtained [119] by calcination of ZIF-8 nanofibers, prepared by directed growth and assembly of ZIF-8 nanocrystals on tellurium nanowires. This carbon material with hierarchical pore structure and nanofibrous morphology can be used as efficient electrocatalyst for ORR (oxygen reduction reaction) in alkaline media, exhibiting excellent electrocatalytic activity and long-term durability as well as good resistance to methanol crossover effects. In addition, a nanoporous carbon material with an unexpectedly high surface area (3405 m^2/g) and considerable hydrogen storage capacity (2.77 wt.% at 77 K and 1 atm) was prepared using ZIF-8 [Zn $(MeIM)_2$; MeIM = 2-methylimidazole] as both a precursor and a template and furfuryl alcohol as a second precursor (Fig. 5.55) [120].

Structural Peculiarities MOF-derived carbons can possess distinct *dimensionality*. Thus, 2D ZIF-8-derived carbon nanosheets with a large surface area with hierarchical porosity were prepared [121] using a porous zinc oxide (ZnO) nanosheet solid as the self-sacrificial template and 2D nanostructure-directing agent. These composites can be applied as advanced electrode materials for electrochemical energy storage devices, demonstrating large ion-accessible surface area and high ion-/electron-transport rates. On the contrary, a 3D hierarchical sandwich-type graphene sheet–sulfur/carbon (GS–S/$C_{ZIF8\text{-}D}$) composite for use in a cathode for a lithium–sulfur battery, prepared by a one-step pyrolysis (Fig. 5.56) of zeolitic imidazolate framework-8 (ZIF-8) [122], showed excellent electrical conductivity and mechanical flexibility.

MOF-derived carbon particles can be formed in distinct *geometrical forms*. Thus, microporous carbon *polyhedrons* (MPCPs) with abundant and uniform micropores, derived from ZIF-8 polyhedrons ([$Zn(MeIM)_2$; MeIM = 2-methylimidazole]), were used as a model microporous carbon host for sulfur in Li–S batteries [123]. Their composites with sulfur (Fig. 5.57) exclusively embedded in micropores exhibited stable cycling performance with high Coulombic efficiency in both DOL/DME and EC/DEC electrolytes. In another report [124], very high surface area 3D carbon *cuboids* (Fig. 5.58), exhibiting a unique

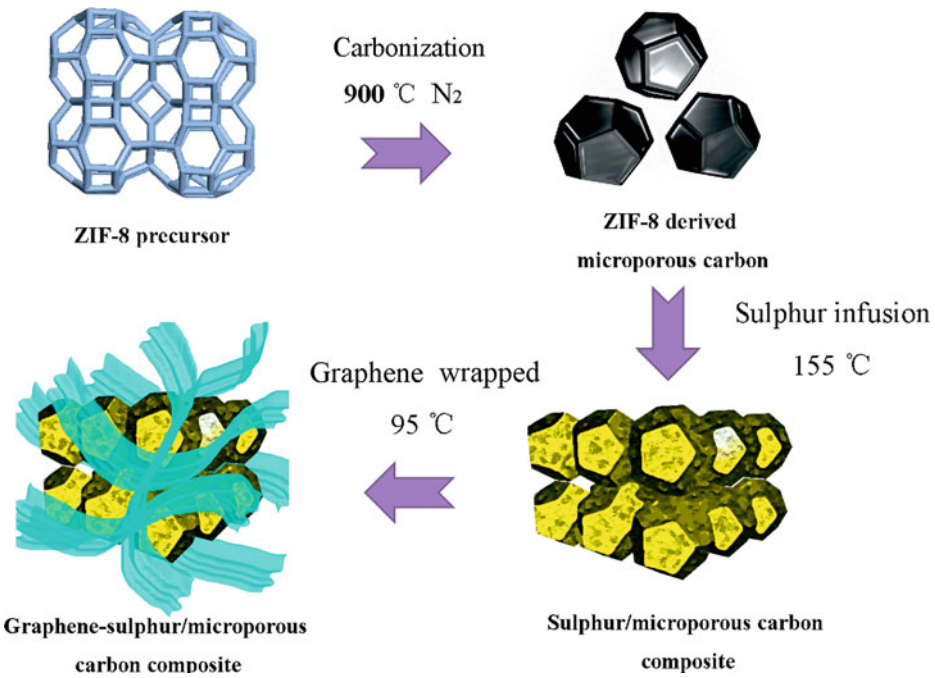

Fig. 5.56 Schematic illustration of the preparation of 3D hierarchically structured GS–S/$C_{ZIF8\text{-}D}$ composite. (Reproduced with permission of the *AIP Publishing*)

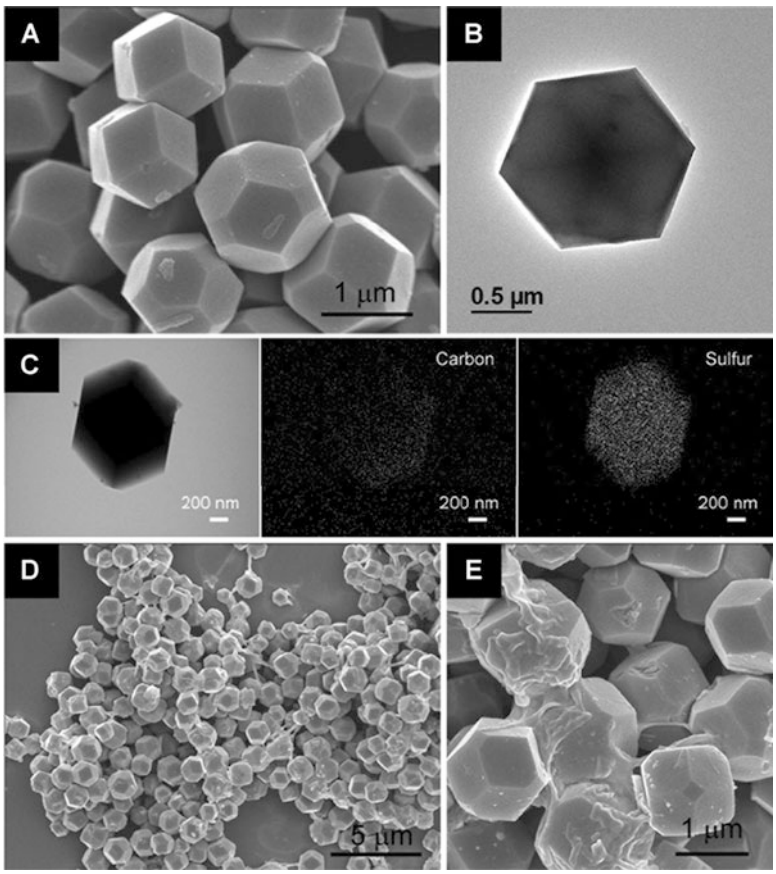

Fig. 5.57 (**a**) FESEM images, (**b**) TEM images, and (**c**) elemental mapping of MPCP-S-I. (**d**, **e**) FESEM images of MPCP-S-II. MPCP-S-I and MPCP-S-II composites with different sulfur contents. (Reproduced with permission of the *Wiley*)

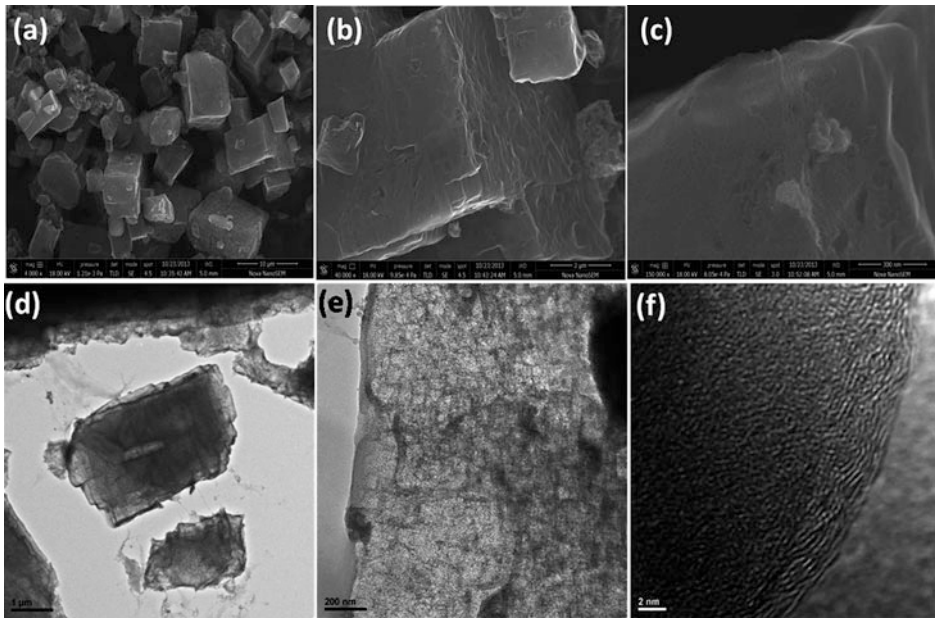

Fig. 5.58 (**a**–**c**) FESEM images of MOF-derived carbon (MOF-DC) at different magnifications; (d–f) HR-TEM images of MOF-DC at different magnifications. The HR-TEM images bring out a very interesting form of a self-similar hierarchical assembly of ultrathin sheets that are highly transparent to TEM electrons; (**d**) shows a peculiar cellular porous morphology with projections of a cuboid type form on various length scales; (**e**) makes this amply clear, where about 20 nm type cells are seen to assemble into 200 nm cells which then form the overall cuboid which is several microns in size; (**f**) brings out the ultrathin layered character of the sheet assembly. (Reproduced with permission of the *Royal Society of Chemistry*)

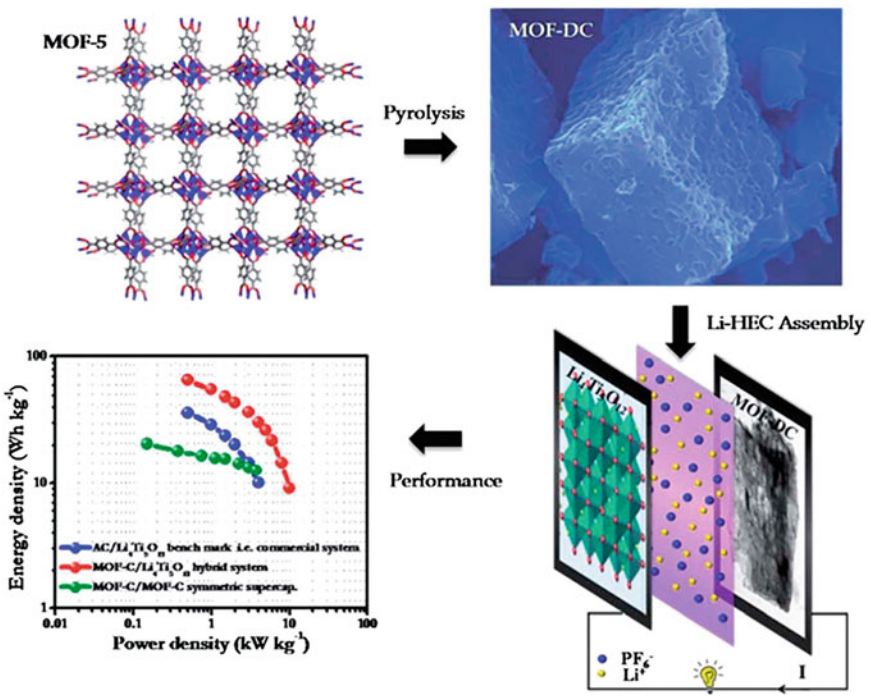

Fig. 5.59 Synthesis of cuboid carbon from MOF-5 and its application in Li-HECs. (Reproduced with permission of the *Royal Society of Chemistry*)

crumpled-sheet assembled porous morphology with the desired levels of micro- and mesoporosity, were synthesized (Fig. 5.59) from a zinc-based MOF-5 as a cathode material with $Li_4Ti_5O_{12}$ and used as the anode for high-performance Li-HECs (hybrid electrochemical capacitors). The MOF-DC-based Li-HEC exhibited outstanding cyclability (10,000 cycles) and retained 82% of the initial value.

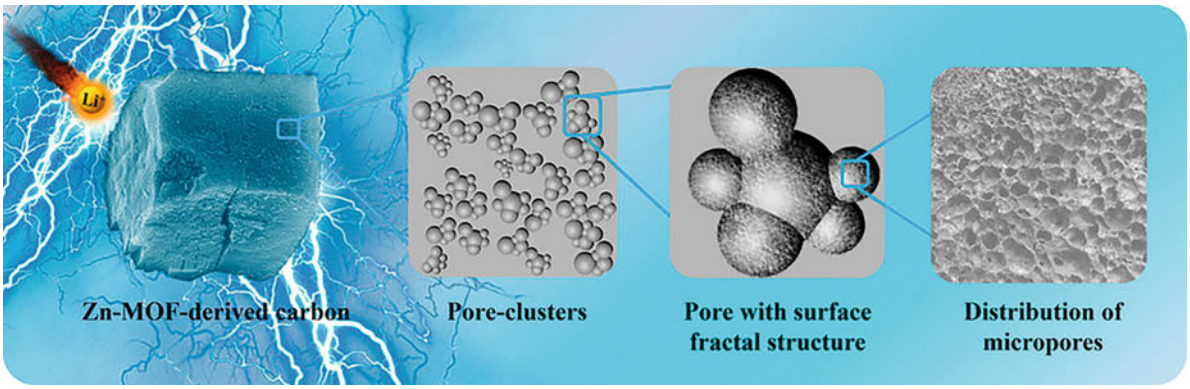

Fig. 5.60 Schematic illustration of the multifractal structure of MOF-derived porous carbon (FPC (sample pyrolyzed under normal pressure) and VFPC (sample pyrolyzed in vacuum)). (Reproduced with permission of *Nature*)

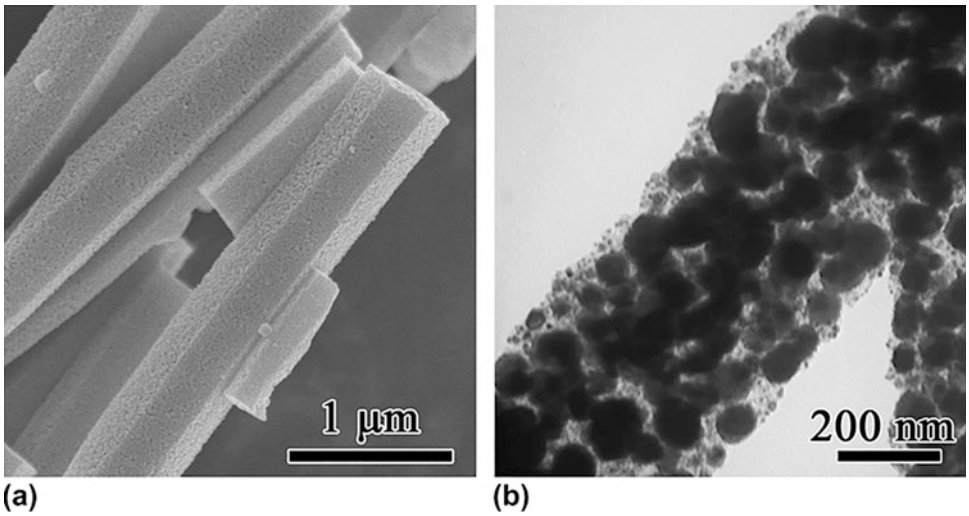

Fig. 5.61 (**a**) SEM and (**b**) TEM images of Co@C, prepared at calcination temperature 800 °C. (Reproduced with permission of the *Materials Research Society*)

Conditions of Pyrolysis The pore structure and surface area of the MOFs can be tuned by changing the *calcination temperature* (600–1000 °C) [125]. The resultant carbon structures possessed high surface areas and differing hydrogen storage capacities, as, for example, in case of carbonized MOF-5 (surface area increased from 835 $m^2 \cdot g^{-1}$ to 2393 $m^2 \cdot g^{-1}$ and also H_2 storage capacity enhanced from 1.9 to 2.7 wt.%). However, in case of metal-doped MOFs, their carbonization does not always lead to an improvement of these characteristics: in case of Cr-MOF, the carbonized samples showed a decrease in both the surface area and hydrogen uptake due to the presence chromium oxide and carbide in the pores. In addition to temperature, *type of pyrolysis* (in vacuum or inert gas) is also important. Thus, a highly porous pure carbon material with multifractal structures was prepared [126] by the vacuum carbonization of a zinc-based MOF (Fig. 5.60), showing an ultrahigh lithium storage capacity of 2458 mAh g^{-1}. The vacuum pyrolysis process was found to induce the formation of multi-fractal structure of porous carbon and more closed pores. The macropores and mesopores offer short path of lithium ions by optimizing the conditions for electrolyte penetration.

Lesser number of reports is devoted to magnetic metals, such as cobalt and iron, whose MOF-derived carbons also have a series of applications. For instance, porous Co@C (surface area of 195.2 m^2/g) composed of uniformly dispersed cobalt metal nanoparticles in *hexagonal-shaped prisms* carbon matrix (Fig. 5.61) and having a strong magnetic response, fabricated by in situ pyrolysis of hexagonal-shaped prismatic Co-MOF-74 crystals [127], showed a superior catalytic activity for reduction of 4-nitrophenol to 4-aminophenol and can be recycled retaining catalytic activity. Co- and N-doped carbon microtubular structures composed of nanoscale hollow spheres and nanotubes were prepared (Fig. 5.62) from cobalt oxalate microtubes serving simultaneously as the solid cobalt precursor for the in situ conversion reaction to MOF (ZIF-67) and self-templates for

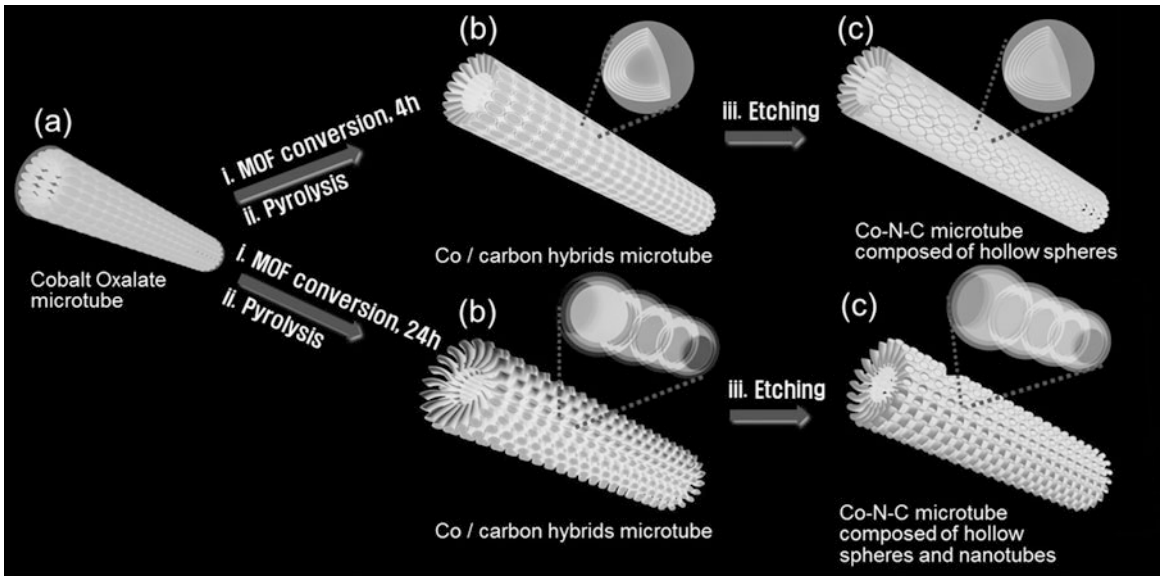

Fig. 5.62 Schematic illustration of the synthesis method for the Co–N–C microtubular structure composed of hollow nanospheres and nanotubes. (**a**) Cobalt oxalate microtube, which is used as both the solid precursor and the self-template. (**b**) Co/C hybrids microtube after a conversion reaction to ZIF-67 microtube and a subsequent pyrolysis process at 800 °C for 3 h under argon flow (inset: inactive Co core@Co–N–C shells). (**c**) Co–N–C microtube composed of hollow subunits, nanospheres, and nanotubes after an acid etching process (inset: Co–N–C hollow subunits). (Reproduced with permission of the *Wiley*)

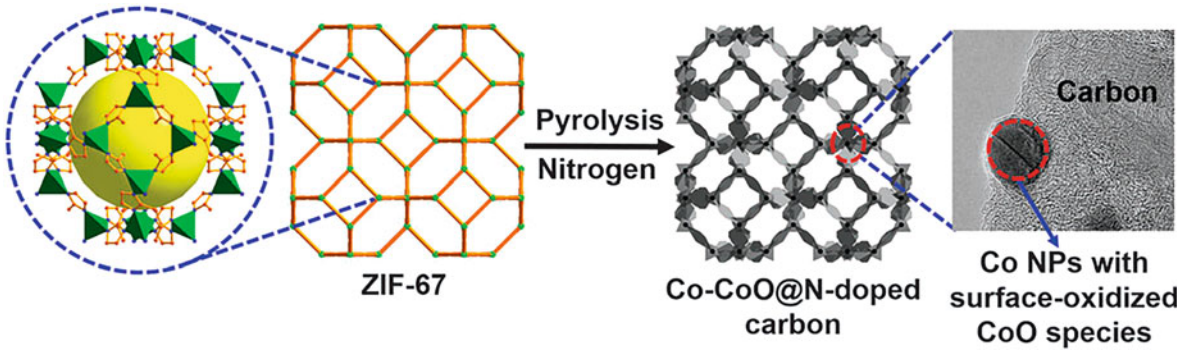

Fig. 5.63 Schematic illustration of the synthesis of Co–CoO@N-doped porous carbon nanocomposites via the pyrolysis of ZIF-67. (Reproduced with permission of the *Royal Society of Chemistry*)

the 1D tubular structure [128]. The crucial role of cobalt oxalate microtubes is twofold: a) the self-template providing a microtubular structure as well as nanoscale hollow subunits by confined conversion to ZIF-67 (cobalt-based zeolitic imidazole framework) and b) the solid precursor providing the cobalt species to react with 2-methylimidazole or the confined in situ growth of ZIF-67 shells surrounding cobalt oxalate nanoparticles. The same Co-based MOF, ZIF-67, was used as a self-template (Fig. 5.63) to afford N-doped porous carbon incorporating Co nanoparticles (Fig. 5.64) with surface-oxidized CoO species, exhibiting excellent catalytic activity, selectivity, and magnetic recyclability toward the direct oxidation of alcohols to esters with O_2 (Fig. 5.65) [129]. It was shown that Co, C, N, and O are detectable on the product surface and the Co is composed of Co^0, Co^{2+}, and Co–OH species.

Carbonization of a self-assembly of ZIF-67 and melamine sponge yielded a Co-MOF-derived magnetic carbon sponge (MCS) [130], exhibiting macroporous properties from carbon sponge, and nanoscale porosity and catalytic sites derived from the immobilized MOFs. Such capabilities as separation of floating oil from water, removal of oil droplets from oil/water emulsions, environmental catalysis, and catalytic H_2 production were noted for the product (Fig. 5.66). Co-containing nanoporous carbon particles (Fig. 5.67), possessing a strong magnetic response, were synthesized by one-step carbonization of ZIF-67 crystals [131], conserving the original ZIF-67 shapes. The nanoporous carbons showed a high surface area and well-developed graphitized walls, contributing to fast molecular diffusion of *methylene blue* molecules with excellent adsorption performance.

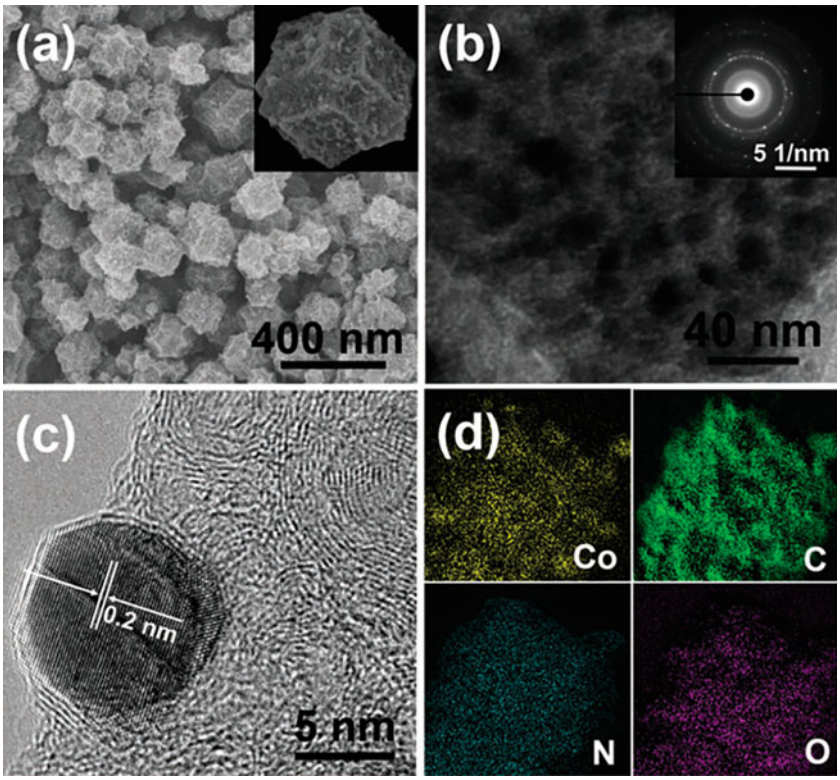

Fig. 5.64 Microstructure observation for nanocarbons obtained at 700 °C for 3 h. (**a**) SEM image (inset: enlarged particle). (**b**) TEM image with inset SAED pattern. (**c**) HRTEM image showing lattice fringes of the crystalline Co nanoparticles and the graphitic layer domains. (**d**) Elemental mapping showing the uniform dispersion of Co, C, N, and a small amount of O elements. (Reproduced with permission of the *Royal Society of Chemistry*)

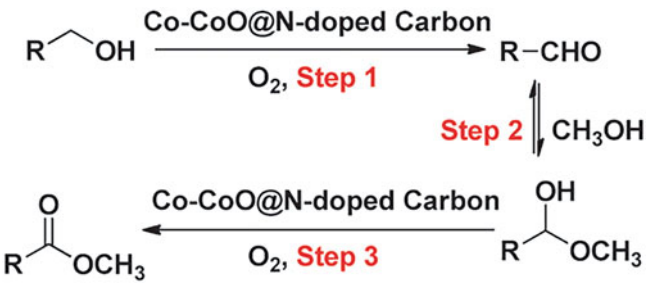

Fig. 5.65 Proposed mechanism for direct oxidative esterification of alcohols over Co–CoO@N-doped porous carbon. (Reproduced with permission of the *Royal Society of Chemistry*)

In case of iron MOFs, a composite material, ferrous hierarchically porous carbon was prepared by high-temperature activation of MIL-100 (Fe) and applied as the cathode in the electro-Fenton system for efficient PFOA (pentadecafluorooctanoic acid, persistent, bioaccumulative, dangerous to humans) degradation [132]. The H_2O_2 and the •OH were detected to confirm the dominating contribution of electro-Fenton degradation mechanism. In addition, an interesting effect was observed using Fe precursor. Thus, graphitic carbon and carbon nanotubes were prepared [133] by heating in reflux for 5 days at reaction temperatures as low as 110 °C from $Fe(COT)_2$ in common solvents (reaction 5.12). This process, being indeed unusual due to mild conditions, is slow; only after 12 h a sufficient amount of graphitic carbon was observed. In addition, in absence of DMSO or Fe source no carbon product was formed. The role of possibly formed Fe nanoparticles or Fe_3O_4 is being elucidated.

$$Fe(COT)_2 + DMSO + DME = Fe_3O_4 + \text{graphite} \tag{5.12}$$

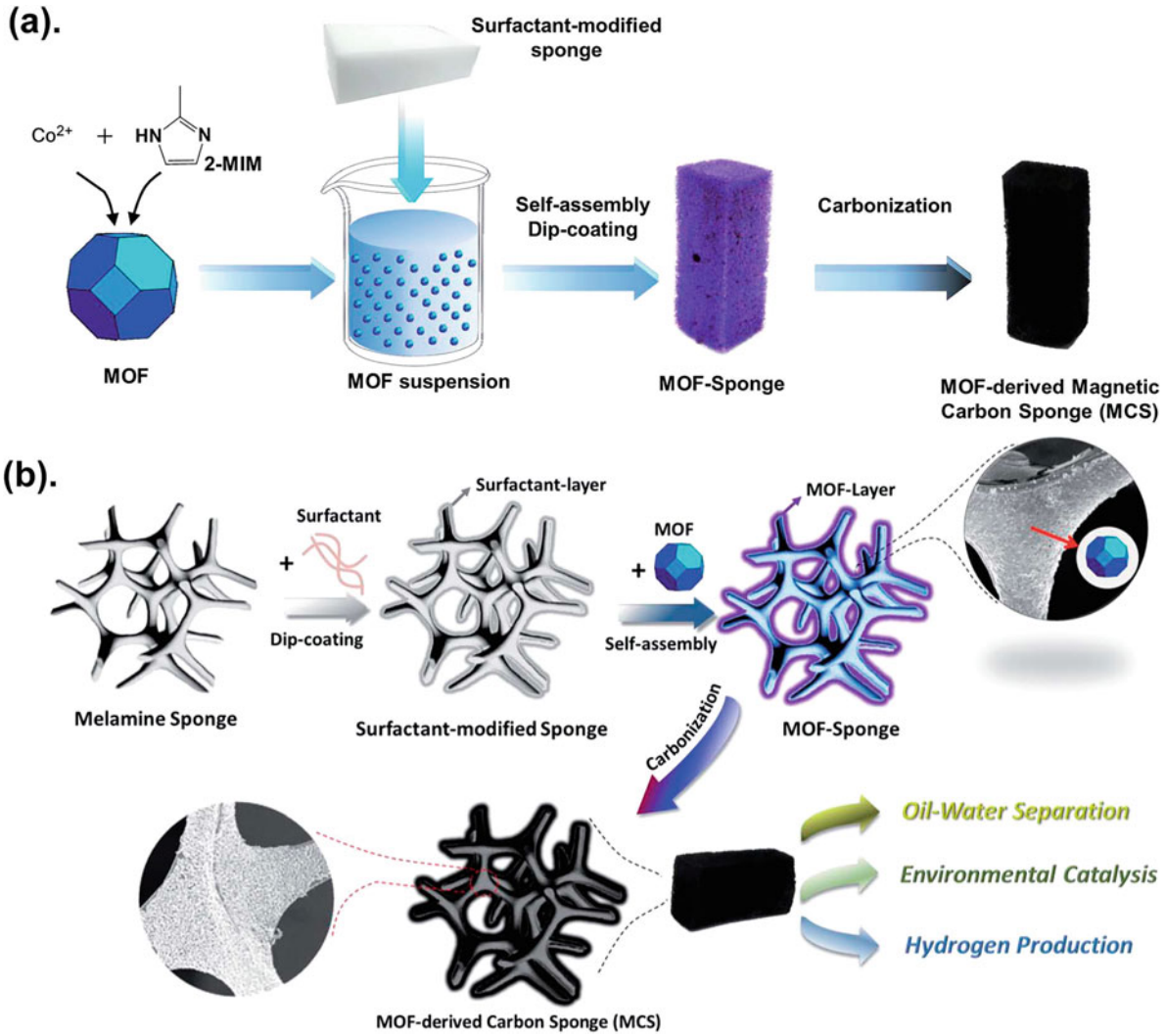

Fig. 5.66 Preparation scheme (**a**) and illustration of surface modification (**b**) of MCS (magnetic carbon sponge). (Reproduced with permission of the *Royal Society of Chemistry*)

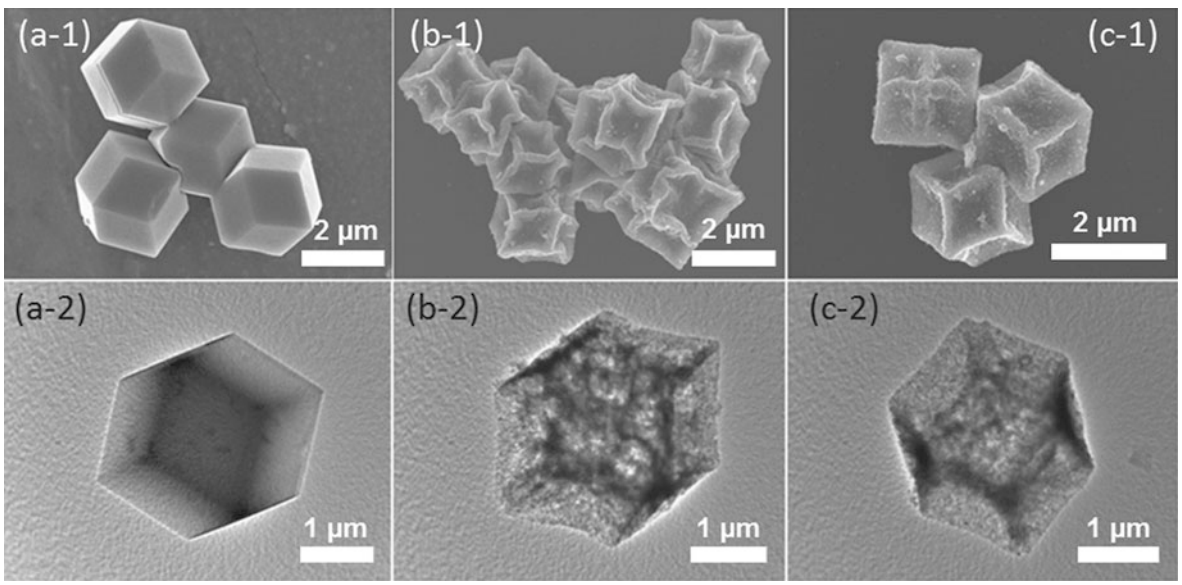

Fig. 5.67 SEM and TEM images of (**a**) ZIF-67 crystals, (**b**) Co/NPC-600, and (**c**) Co/NPC-800. (Reproduced with permission of *Wiley*)

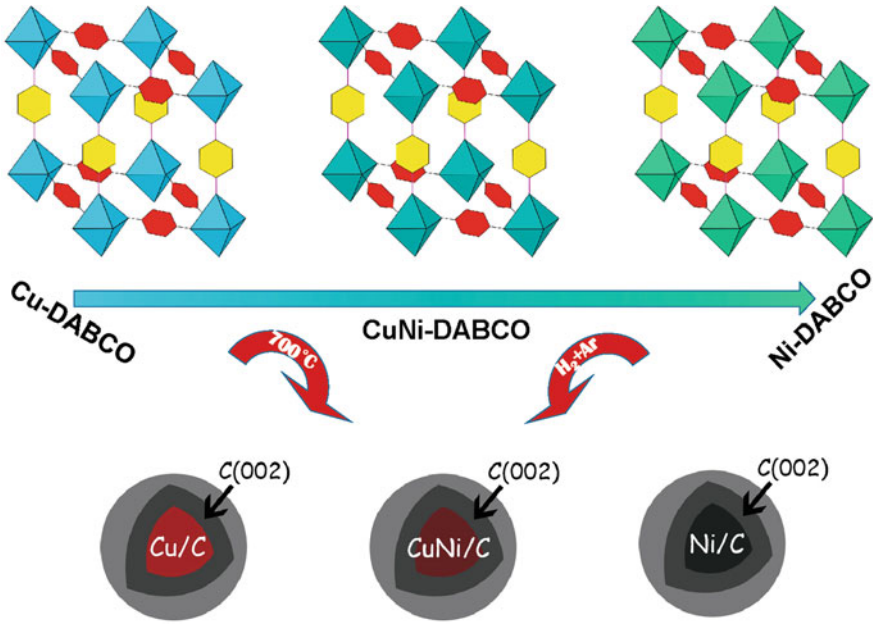

Fig. 5.68 Schematic illustration of the synthesis procedure of the CuNi/C-n. (Reproduced with permission of the *Springer*)

Bimetallic MOF-Derived Carbons Some MOFs have been used to synthesize non-precious bimetallic carbon nanocomposites, for instance, those of CuNi-DABCO-n (Fig. 5.68, DABCO = 1,4-diazabicyclo[2.2.2]octane) with a series of molar ratios Cu:Ni, used as efficient ORR catalysts [134], since both metals can improve catalytic activity. Their extraordinary stability in alkaline was found to be superior to that of commercially available Pt-based materials. These MOF-derived CuNi/C obtained a nanoscale particle size, high surface area, and graphitic carbon from the precursor, which benefits subsequent ORR catalytic activity. Also, magnetic porous carbon-based sorbent (MPCS) with core-shell structure was prepared from the pyrolysis of Fe-III-modified MOF-5 [135]. Studies of its sorption behavior of five organic micropollutants (atrazine, carbamazepine, bisphenol A, norfloxacin, and 4-nitrophenol) showed the adsorption capacities in the order of 4-nitrophenol > norfloxacin > bisphenol A > carbamazepine > atrazine.

Bimetallic Zn/Co-based ZIFs coated on tellurium nanotubes were pyrolyzed, generating a structure with high surface area, hierarchical pore structure, abundant Co–N_x active sites, and a 1D tubular graphitic carbon framework [136]. Such hierarchically porous Co- and N-doped CNTs are highly efficient electrocatalysts for both oxygen and triiodide reduction reactions. We note (see above a Zn-based example of ZIF-8 on Te nanowires) that tellurium nanowires or nanotubes are frequently used as ZIF-8 supports for further formation of nanocarbons. Other Zn-/Co-containing nanocarbons, the C–$ZnCo_2O_4$–ZnO nanorod arrays (NRAs), were rational designed (Fig. 5.69) and synthesized via a facile template-based solution route on Ti foil substrate and used as high-performance anode for lithium–ion batteries (LIBs) [137]. The MOF-derived carbon layers (Fig. 5.70) on the $ZnCo_2O_4$–ZnO nanorods surface can serve as a conductive substrate as well as buffer layer to restrain volume expansion during charge–discharge process. When used as LIBs anode materials, the C–$ZnCo_2O_4$–ZnO NRAs showed excellent electrochemical performance with high capacity and superior cycling stability.

Role of N-Doping N-doped nanocarbons are common and the presence of nitrogen frequently contributes to useful properties. In addition to examples throughout the text, the nitrogen-doped carbon sponges composed of hierarchical microporous carbon layers were prepared from MOFs via carbonization at high temperature under Ar and NH_3 flow [138], and then Se was impregnated into 0.4–0.55 nm micropores by melting-diffusion and infiltration methods (Fig. 5.71). Nitrogen doping was found to improve the electrical conductivity of carbon matrix and to facilitate rapid charge transfer, making the carbon sponge a highway for charges involved in redox reactions. These large-surface rodlike N-doped carbon sponges with hierarchical porosity could be potential candidates in the related energy storage systems, having excellent electrochemical performance. Schematic discharge–charge mechanism of the composite cathode on their basis is shown in Fig. 5.72.

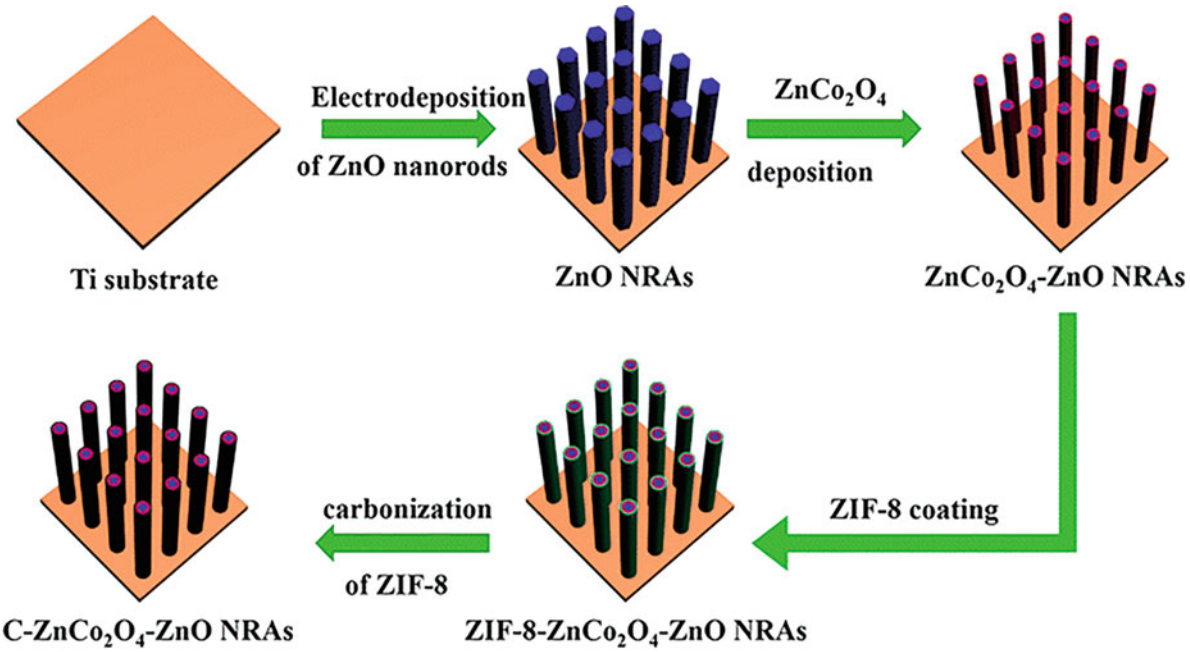

Fig. 5.69 Schematic illustration for the formation of the C–$ZnCo_2O_4$–ZnO NRAs electrode. (Reproduced with permission of *Springer*)

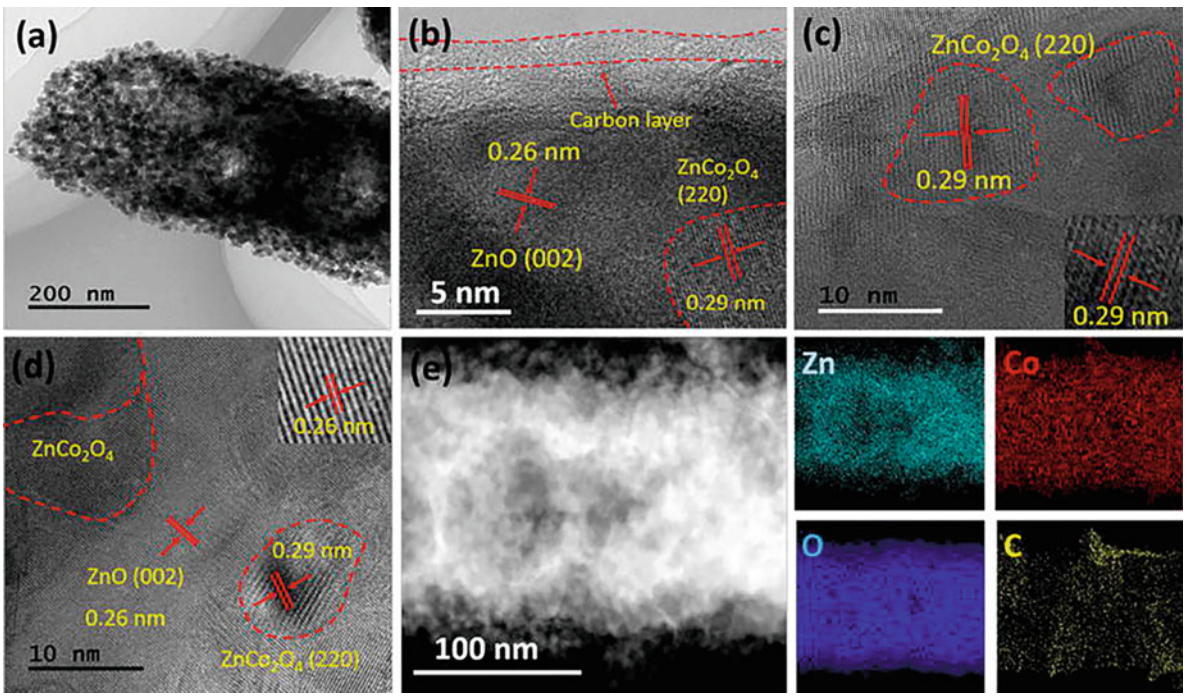

Fig. 5.70 (**a**) TEM image, (**b–d**) HRTEM lattice images (the inset figures in **c** and **d** can be ascribed to crystal lattice of $ZnCo_2O_4$ and ZnO, respectively), and (**e**) elemental mapping images (Zn, Co, O, and C) of the C–$ZnCo_2O_4$–ZnO. (Reproduced with permission of *Springer*)

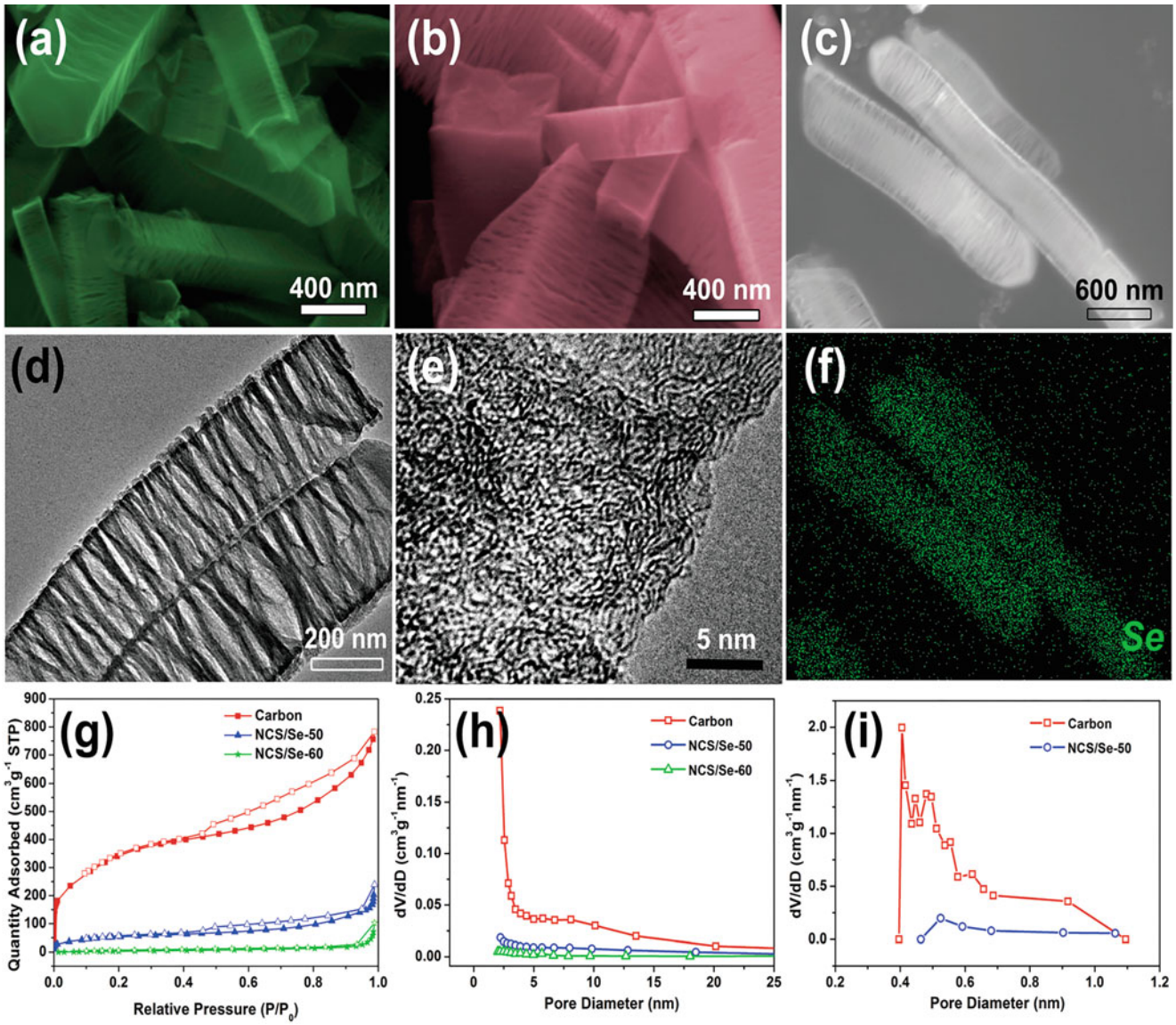

Fig. 5.71 (**a**, **b**) FESEM images, (**d**–**e**) TEM and high-resolution TEM images, (**c** and **f**) Se elemental mapping results of the NCS/Se-50 composites. (**g**) N_2 adsorption–desorption isotherms, (**h**) pore (>2 nm) size distribution, and (**i**) micropore size distribution of NCS and NCS/Se composites. (Reproduced with permission of the *Royal Society of Chemistry*)

Applications of MOF-derived nanoporous carbons are very promising and include [139] CO_2 capture, catalysis (in that number, magnetically recoverable supported catalysts) and photocatalysis, fabrication of pseudo-capacitance electrodes, adsorbents for removal of heavy metals and toxic species from drinking water, drug delivery carriers, electrolyte/membrane materials for fuel cells, sulfur hosts for lithium–sulfur batteries, etc. As a specific case, on the basis of analysis [140] of applications of MOF-derived nanostructures in electrochemical energy storage, catalysis, sensing, and other industries, it can be concluded that ZIF-8-derived carbon materials generally have the highest surface area, which is desirable for electrochemical energy storage. As an example of sensing applications, a GO hybrid with Co-based MOFs (Co-MOFs@GO) was prepared by the hydrothermal process [141] and was found to have outstanding hydrogen sensing (stable, repeatable, and selective responses and recovery times below 12 s at 15 °C), after improvement by sputtering platinum (Pt) as a catalyst (Figs. 5.73 and 5.74). This hybrid was offered a promising material for industrial application in hydrogen sensing.

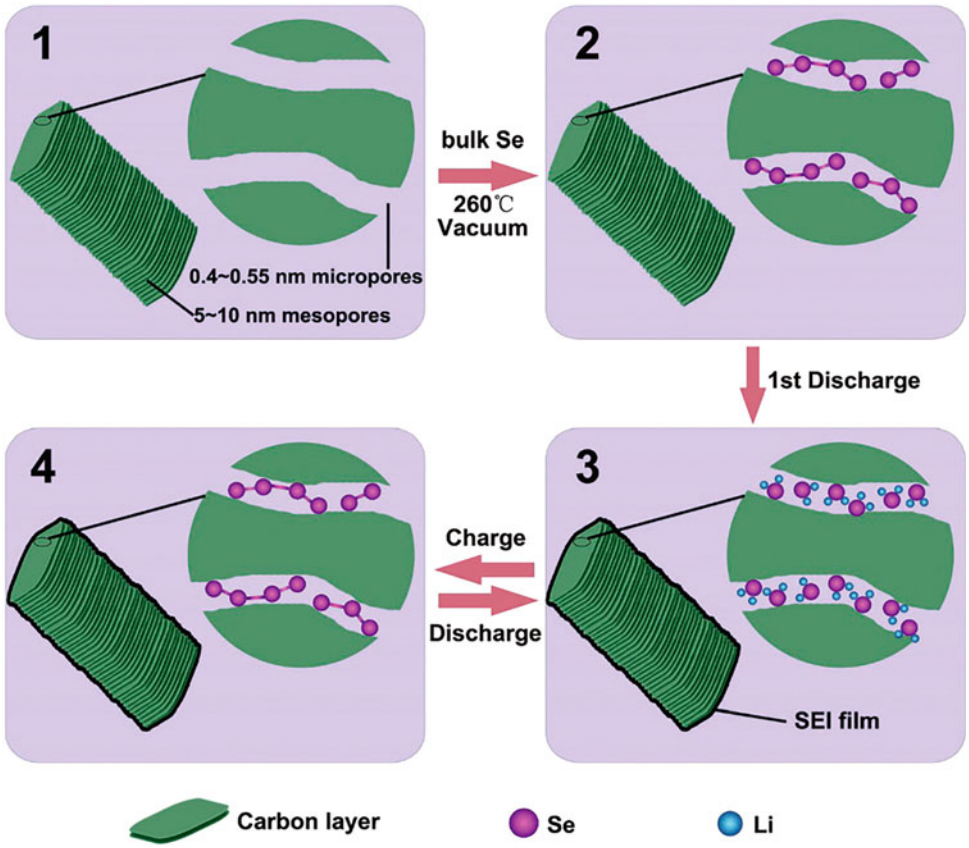

Fig. 5.72 Schematic discharge–charge mechanism of the NCS/Se-50 composite cathode. (Reproduced with permission of the *Royal Society of Chemistry*)

Several other application examples in different areas are as follows. Thus, a versatile strategy for the controllable synthesis of 3D MOF hybrid arrays by utilizing semiconducting nanostructures as self-sacrificing templates was developed [142]. These MOF-hybrid-array-derived carbon-based composites with well-aligned hierarchical morphology and self-supporting structure can be directly applied to both anodes and cathodes for water splitting. Nanoporous carbon particles of approximately 50-nm diameter, prepared [143] by direct carbonization of ZIF-8, exhibited very high biocompatibility and, hence, are promising as intracellular drug delivery carriers. Also, solvent exfoliation was applied to prepare exfoliated porous carbon (EPC) from an isoreticular MOF-8 (IRMOF-8, $Zn_4O(ndc)_3$, ndc = naphthalene-2,6-dicarboxylate)-derived porous carbon [144]. The obtained product with high surface area (1854 $m^2\ g^{-1}$) and improved dispersibility was used as electrode modifier for glassy carbon electrode in square-wave voltammetry detection of chloramphenicol. In addition, a rational strategy (Fig. 5.75) to improve sodium storage performance of red phosphorus was offered by confining nanosized amorphous red P into

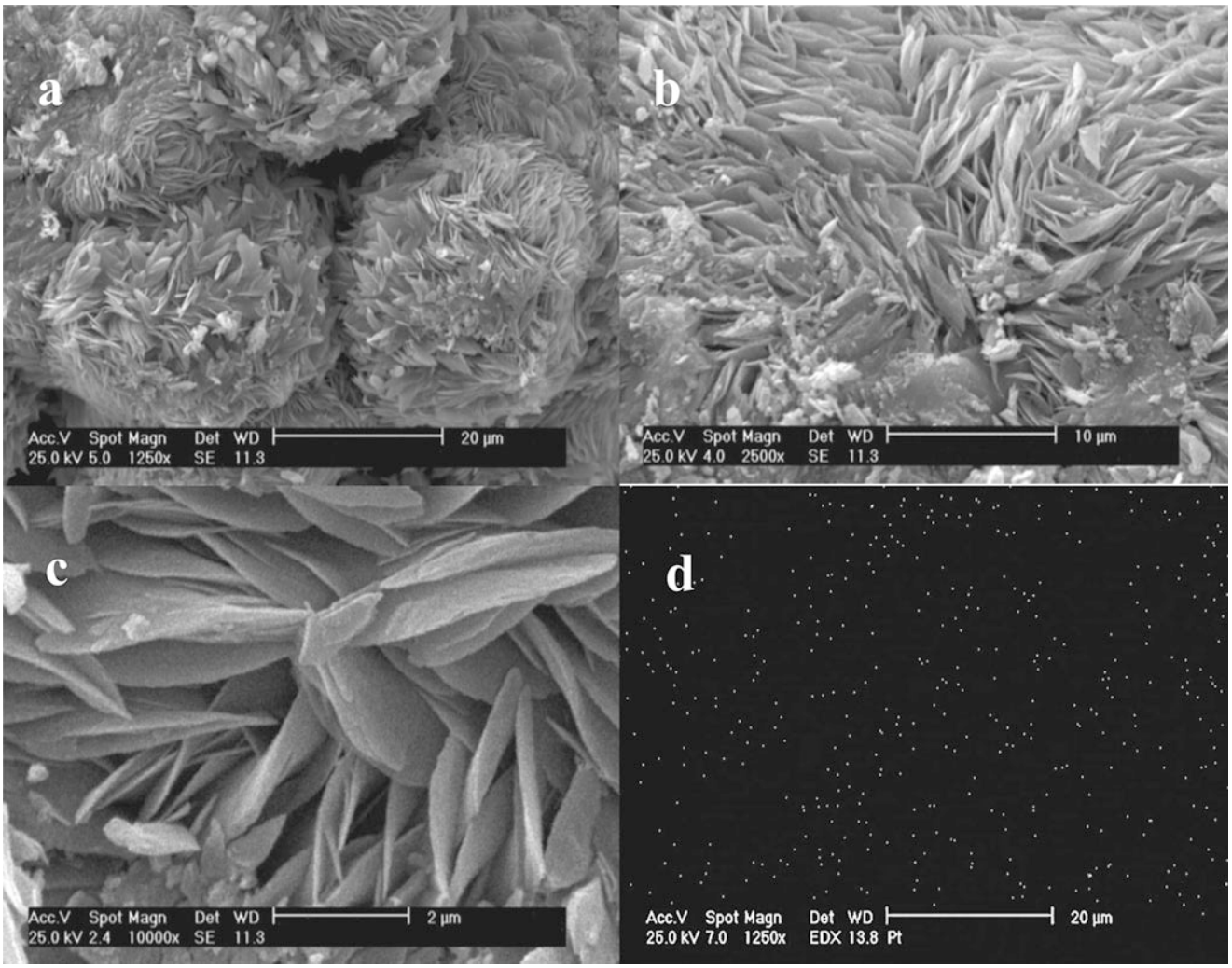

Fig. 5.73 SEM images of Pt-sputtered GO hybrid with Co-based MOFs (Co-MOFs@GO) in flowerlike structure (**a**–**c**), Pt elemental mapping (**d**). (Reproduced with permission of the *IOP Publishing*)

ZIF-8-derived nitrogen-doped microporous carbon matrix (P@N-MPC) [145]. The N-doped porous carbon with sub-1 nm micropore was found to facilitate the rapid diffusion of organic electrolyte ions and improves the conductivity of the encapsulated red phosphorus. Oxygen reduction reactions (ORR) are also a promising field of applications of MOF-derived carbons (see other examples above) [146].

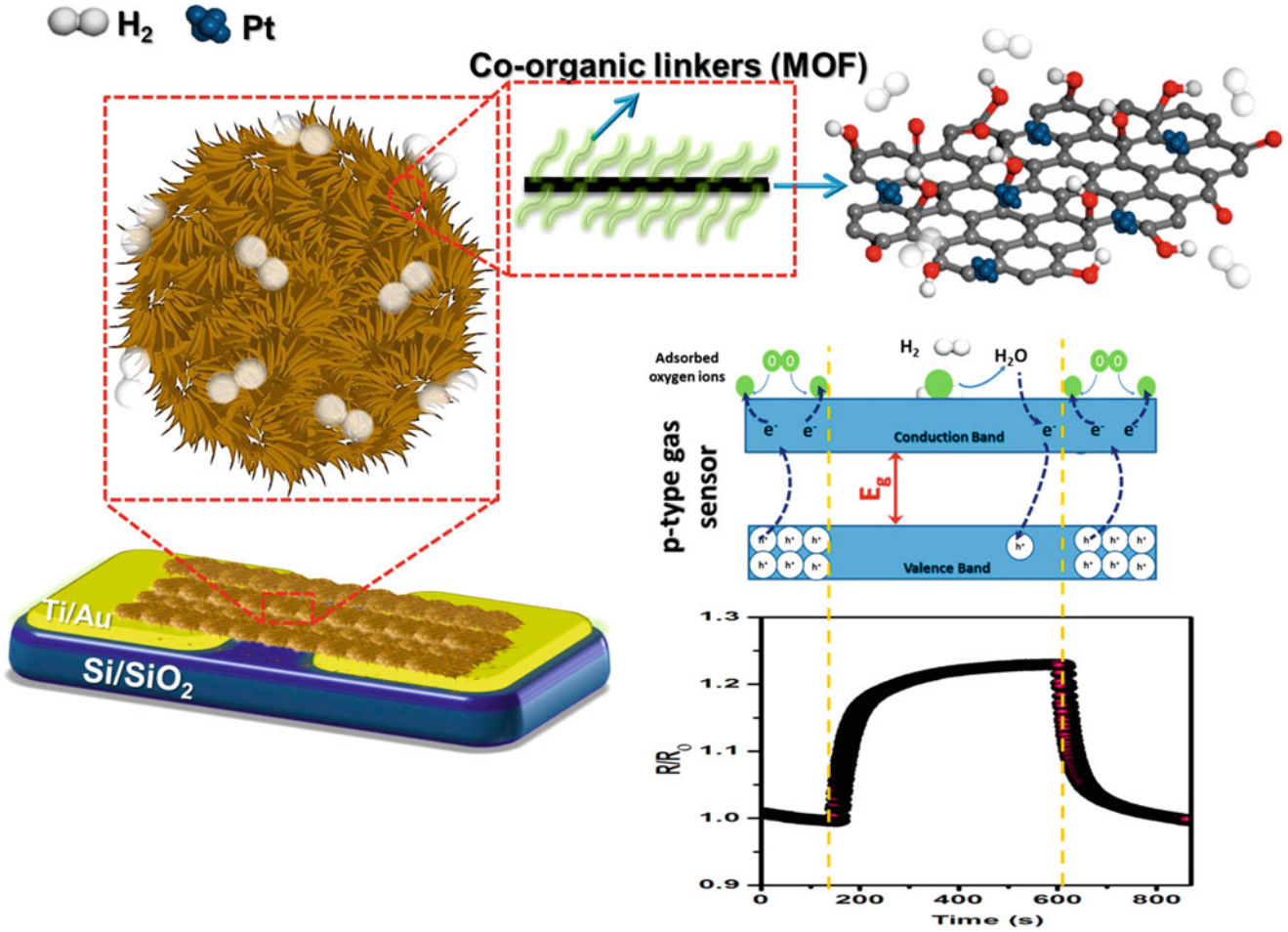

Fig. 5.74 Schematic illustration of H_2 reaction with Pt-sputtered Co-MOFs@GO. (Reproduced with permission of the *IOP Publishing*)

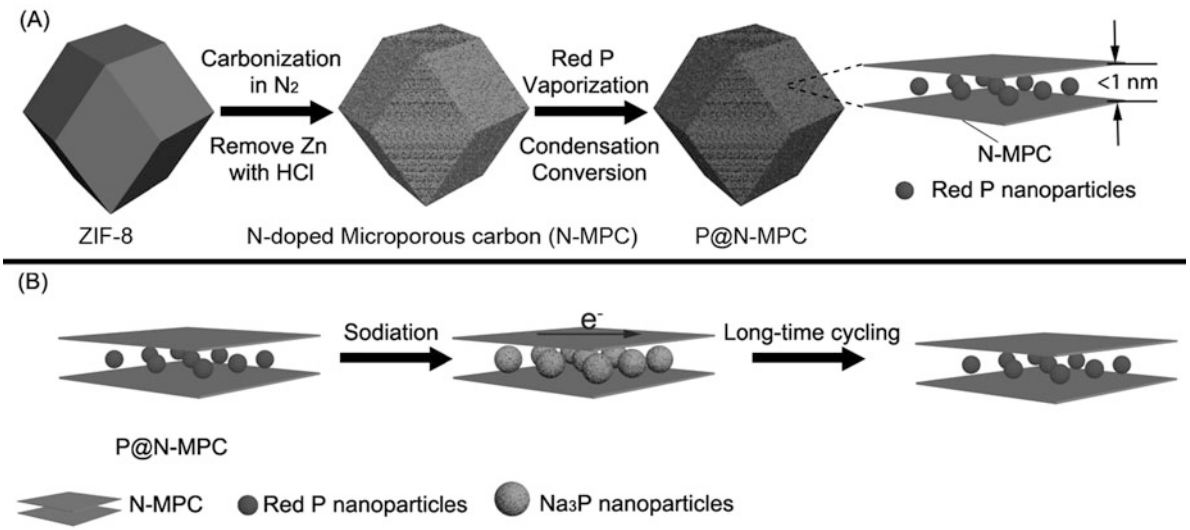

Fig. 5.75 Schematic illustration of the preparation process for (**a**) P@N-MPC and (**b**) sodiation process of P@N-MPC. (Reproduced with permission of the *Wiley*)

5.6 Lonsdaleite

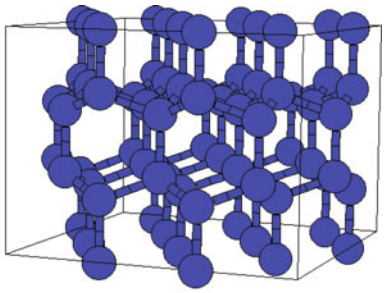

Lonsdaleite (hexagonal diamond) is a carbon allotrope with a hexagonal lattice. It was observed in nature in places, where meteorites striked the Earth, and also it was artificially synthesized from graphite. Both processes involve high pressures and heating, transforming the graphite into diamond, but conserving hexagonal crystal lattice of graphite. Occurrences of lonsdaleite and nanometer-sized diamonds have been speculated to serve as a marker for meteorite impacts, having also been connected to the Tunguska explosion in Russia, the Ries crater in Germany, the Younger Dryas event in sites across North America, and more [147]. Main features of lonsdaleite are as follows:

- Lonsdaleite was first described almost 50 years ago from the Canyon Diablo iron meteorite.
- The lonsdaleite (both natural and artificial) is usually observed in small amounts inside the diamond crystals.
- Lonsdaleite was obtained under 13 GPa of pressure at 1270 K in 1967.
- Lonsdaleite has never been produced or described as a separate, pure material.
- A 2H polytype of sp^3-carbon.
- Can be synthesized in the laboratory by CVD or thermal decomposition of poly(hydridocarbyne).
- Is translucent, brownish-yellow.
- Refraction index 2.40.
- The theoretical density of lonsdaleite is 3.51 $g{\cdot}cm^{-3}$, the same as for cubic diamond.
- Harder than cubic diamond (58% more).
- Can be considered as "stacking disordered diamond."
- The stiffest quasi-2D films with lonsdaleite structure can potentially exist [148].

Lonsdaleite has a hexagonal unit cell (Fig. 5.76) [149]. Hexagonal diamond differs from the cubic one (3C) by the layers stacking. Crystal lattice of cubic diamond represents itself a sequence of atomic layers ABCABC..., whereas lonsdaleite lattice represents ABAB... stacking [150]. Some diffraction features attributed to lonsdaleite are shown in Fig. 5.77 [151]. The calculated strength and stiffness properties of lonsdaleite, based on a first-principles method, showed [152] that lonsdaleite exhibits excellent mechanical properties, as follows: a) the maximum stiffness coefficient of lonsdaleite is 1324.57 GPa, the maximum Young's modulus is 1324.57 GPa, and the maximum compressive strength is 727.16 GPa, which are all above the corresponding values for diamond; b) the bulk modulus of lonsdaleite is 437.09 GPa, which is as good as the bulk modulus of diamond; and c) the maximum tensile strength of lonsdaleite is 130.23 GPa, which is close to that of diamond. The three key crystallographic axes of lonsdaleite are the [2 1 1 0], [0 1 $^{-}$1 0], and [0 0 0 1] orientations (Fig. 5.78).

Artificially, the lonsdaleite can be produced from graphite by shock compression. Thus, unprecedented in situ X-ray diffraction measurements of diamond formation on nanosecond timescales by shock compression of pyrolytic as well as polycrystalline graphite to pressures from 19 GPa up to 228 GPa (Fig. 5.79) were shown [153]. The direct formation of lonsdaleite was observed above 170 GPa for pyrolytic samples only. In a related report [154], applying high-temperature and high-pressure treatment of graphite, it was found that the synthesized material contains not only diamond nanoparticles but also some relatively large (up to several nanometers) fragments of lonsdaleite (Fig. 5.80). It was supposed that the formation of these polytypes and lonsdaleite layers is caused by the propagation and interaction of phonon waves in the crystal during

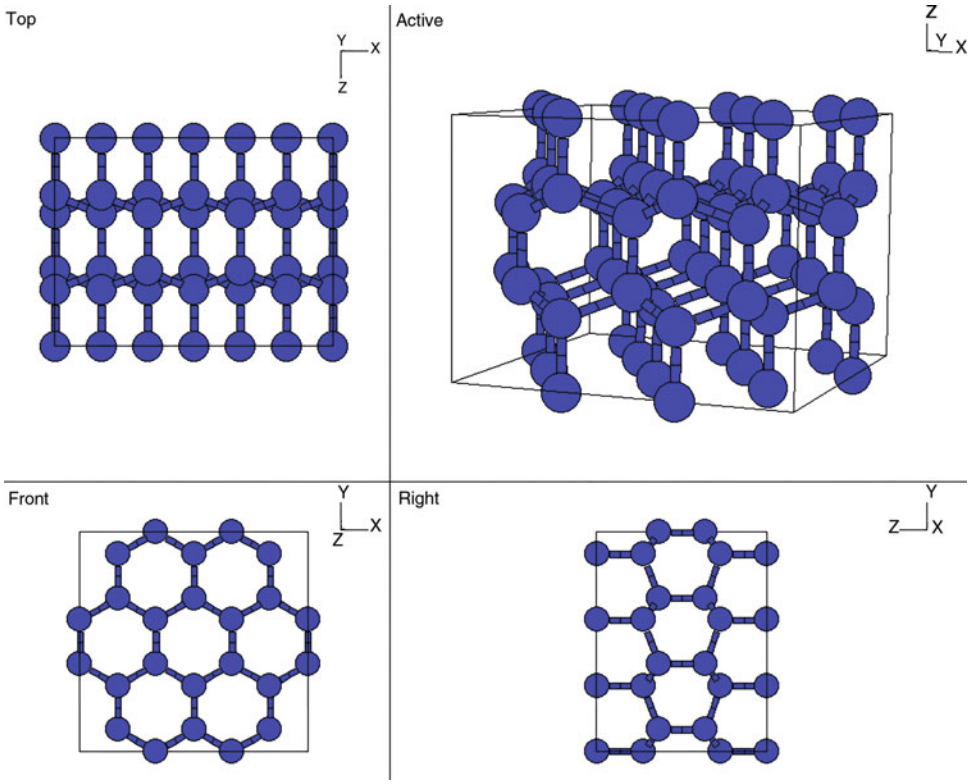

Fig. 5.76 Hexagonal unit cell of lonsdaleite

the high-temperature treatment when the phonon wavelength has a value of approximately several interplanar distances in a diamond lattice. Apparently, deformational twinning was also responsible for the formation of polytypes and lonsdaleite. The transformation of graphite to lonsdaleite and diamond was also found to be initiated by sliding of hexagonal carbon planes of graphite along the [210] of the graphite structure [155], suggesting that lonsdaleite and diamond in ureilites formed directly from graphite through boat-type buckling and chair-type puckering of hexagonal carbon planes of graphite, respectively. In addition, in Raman spectra of carbonaceous rocks excavated from the Popigai crater (Siberia), the most intensive band at 1292–1303 cm^{-1} was ascribed to $_{A1g}$ vibration mode of lonsdaleite, whereas the less intense band at 1219–1244 cm^{-1} was attributed to E_{2g} vibration mode [156]. This correlation permits a rough estimation of lonsdaleite/diamond phase ratio in sp^3-bonded carbon samples in the impact rocks. For the Fe-doped lonsdaleite, it was shown [157] that the Fe ions act as the luminescent center, while other K, Ca, Mg, Zn, and Tl dopants or C vacancy can induce widely distributed hole traps that can contribute to the remarkably prolonged decay time. Also, it was predicted that Cr and Mn ions in lonsdaleite may even give more favorable persistent luminescence property.

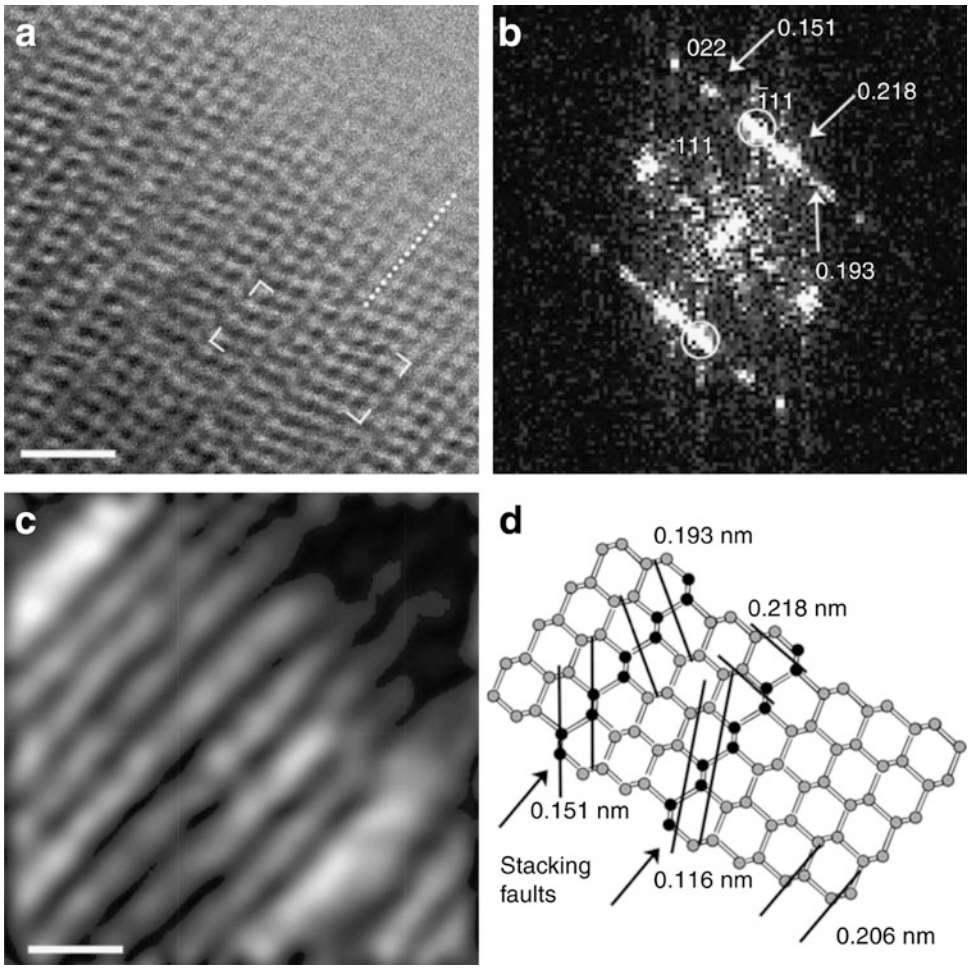

Fig. 5.77 Stacking faults provide an explanation for the reflections and *d*-spacings of "lonsdaleite." (**a**) <011> STEM image from the Canyon Diablo sample; one of many {111} stacking faults is indicated by the dotted white line. (**b**) FFT calculated from **a**. White arrows indicate spacings (0.218, 0.193, and 0.151 nm) that have been attributed to "lonsdaleite." (**c**) Amplitude image calculated from the {−111} set of diamond reflections (white circles in **b**). Bright regions indicate domains two to four layers across separated by {111} stacking faults. (**d**) Structure model of the region marked with white corners in **a**. Stacking faults (black layers of atoms) result in *d*-spacings that are absent in single-crystal diamond and give rise to the broad X-ray and electron-diffraction features. Scale bars mark 1 nm for **a**, **c**. (Reproduced with permission of *Nature*)

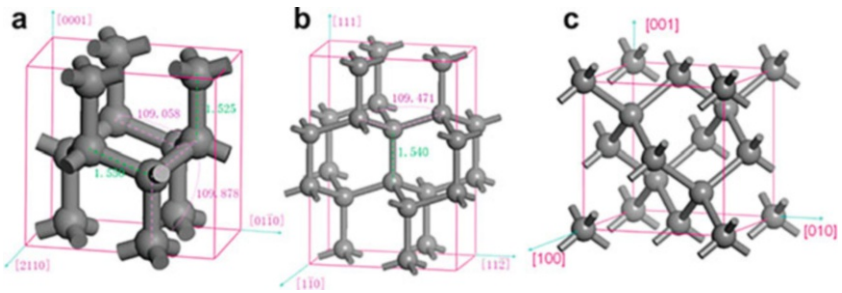

Fig. 5.78 The supercell and coordinate system for lonsdaleite and diamond. (**a**) Rectangular solid supercell in the redefined orthorhombic coordinate system for the [2 1 1 0], [0 1 $\bar{1}$ 0], [0 0 0 1] orientations of lonsdaleite. (**b**) Rectangular solid supercell in the redefined orthorhombic coordinate system for the [1 1 $\bar{2}$], [1 $\bar{1}$ 0], and [1 1 1] orientations of diamond. (**c**) Cubic supercell in the redefined cubic coordinate system for diamond with [1 0 0], [0 1 0], and [0 0 1] orientations. (Reproduced with permission of the *Elsevier Science*)

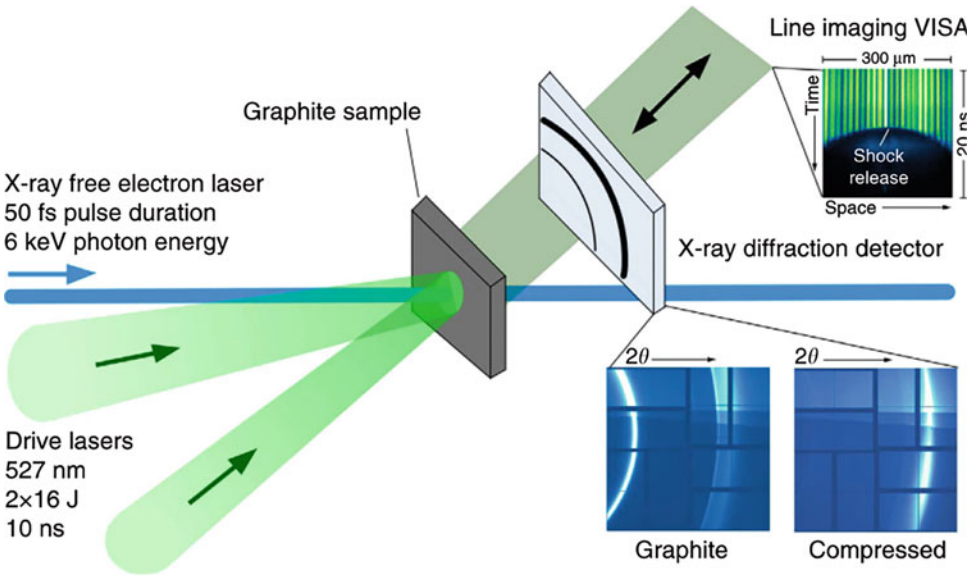

Fig. 5.79 Schematic of the experimental setup at the Matter at Extreme Conditions endstation of the Linac Coherent Light Source. Two high-energy laser beams drive shock waves into graphite samples generating pressures from 20 to 230 GPa. The shock transit times of few nanoseconds are recorded by a VISAR system, which detects the shock-induced reflectivity drop of a 100-nm thick aluminum coating when the shock exits on the target rear side. The microscopic state is probed by a single X-ray pulse with 6 keV photon energy and 50 fs pulse duration. X-ray diffraction is recorded by a large-area X-ray detector. (Reproduced with permission of *Nature*)

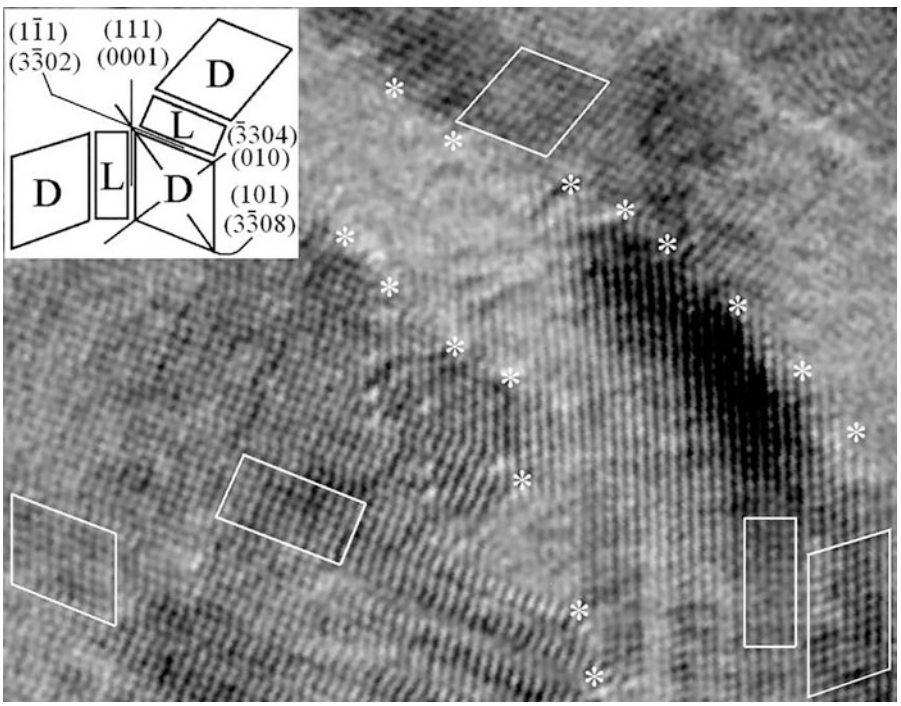

Fig. 5.80 A high-resolution image of a particle containing the diamond and lonsdaleite lattice inclusions, zone axis <110>. Asterisks indicate the long incoherent boundaries of the twinned areas. Fragments of the diamond lattice are shown in parallelograms, and fragments of the lonsdaleite lattice are shown in rectangles. The left-upper corner inset shows the scheme of the whole structure. Three orientations of diamond lattice and two orientations of lonsdaleite are shown there. Twinning planes (111) and (111) of diamond correspond to (0001) and (3302) of lonsdaleite. Two fragments of lonsdaleite shown in the scheme are oriented as twins with respect to planes (010) and (101) of diamond. These two planes correspond to ($\bar{3}$304) and (3$\bar{3}$08) of lonsdaleite. (Reproduced with permission of *Wiley*)

5.7 Chaoite

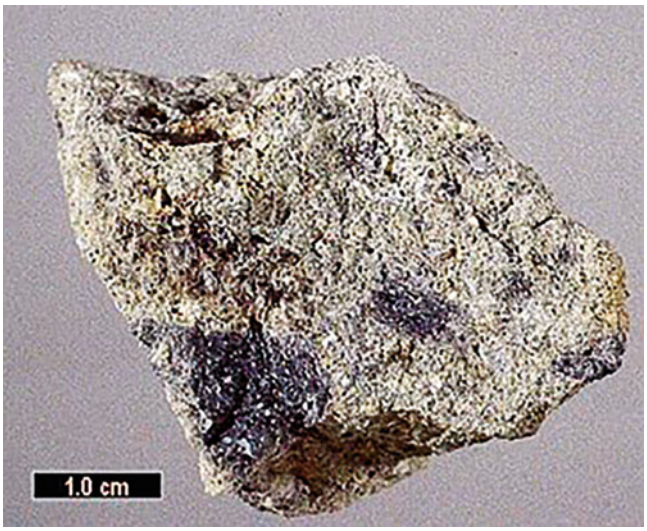

Chaoite ("white carbon," colored from gray to white) was discovered in shock-fused graphite gneiss from the Ries crater in Bavaria in 1969. It is hexagonally stacked by cross-linking linear carbyne chains with *sp*-hybridized carbon atoms, so this phase belongs to the carbyne–diamond group. Chaoite is a less studied member among the known crystalline carbon phases and its existence is still under disputes. Chaoite is sometimes attributed as a part of "possible carbon forms." Its main features are as follows:

- Slightly harder than graphite (between talc and gypsum).
- It is considered to have a carbyne structure. Indeed, atomic-scale wires comprised of *sp*-hybridized carbon atoms represent ideal 1D systems to potentially downscale devices to the atomic level [158].
- It can be prepared from graphite by sublimation at 2700–3000 K or by irradiating it with a laser in high vacuum.
- It occurs in shock-metamorphosed graphite gneisses and in ureilite meteorites.
- It crystallizes in hexagonal crystal system with cell dimensions *a*, 8.948; *c*, 14.078; *Z*, 168; *V*, 976.17; and space group, P6/mmm.
- Chaoite can be converted to other carbon phases [159].

Synthesis methods are not well-developed for this carbon allotrope. Thus, a solid large-surface paramagnetic Si/C/O/N nanocomposite was obtained [160] by silica etching by laser-photolytic products of pyridine decomposition and found to be paramagnetic and composed of amorphous CN bonds containing poly(oxocarbosilane)-containing crystalline nanoregions of rare chaoite. Heating this product to 650 °C, chaoite regions are depleted revealing regions of crystalline silica. The carbon–cobalt films were deposited by pulsed anodic electric arc system, using graphite rod electrode [161], exhibiting amorphous and crystallized zones corresponding to different phases of carbon (graphite, chaoite, and fullerene, Fig. 5.81).

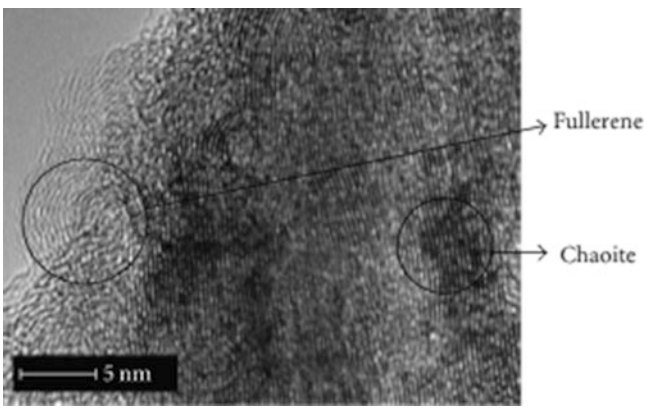

Fig. 5.81 HRTEM image obtained for 0.3% cobalt-doped carbon thin film. Regions with curved fringes of fullerene-like graphitic layers and chaoite structure can be seen. (Reproduced with permission of *Hindawi*)

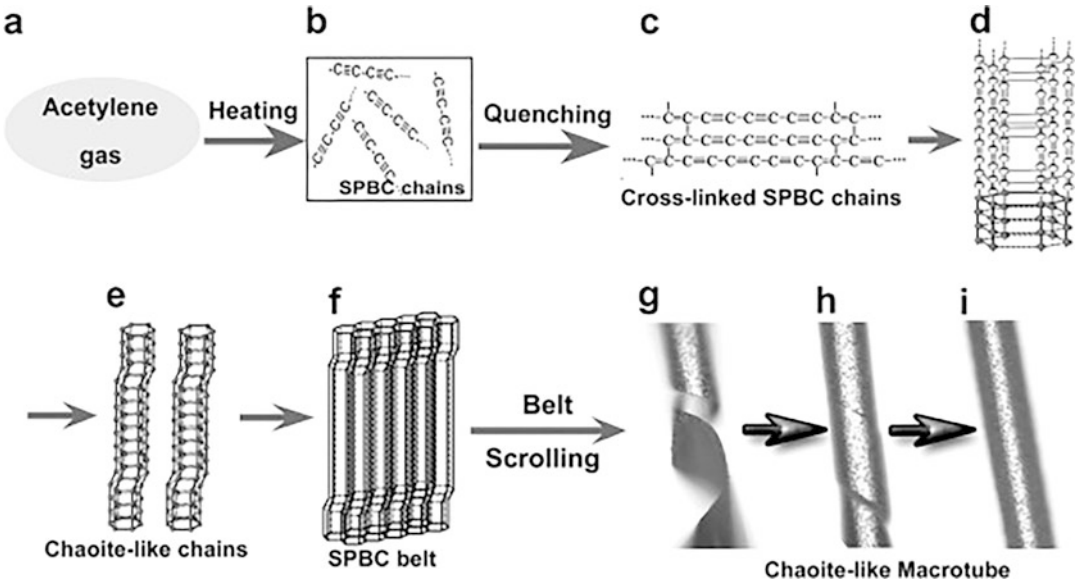

Fig. 5.82 Chaoite-like carbon was prepared by quenching the pyrolysate of acetylene gas at 873 K and ambient pressure. (Reproduced with permission of the *Elsevier Science*)

Milder conditions for chaoite formation are of interest for researchers [162]. Thus, chaoite phase was synthesized by quenching the pyrolysate of acetylene gas at low temperature (873 K) and pressure (1 atm) [163, 164], having typical morphology of a tube with 20–60 μm in diameter and more than 8 mm in length (chaoite-like multicrystals, which are formed by cross-linking the kinked *sp*-bonded carbon chains, Fig. 5.82). These carbon macrotubes also possessed unexpected clear intrinsic ferromagnetism, indicating that the *sp*-hybridized structure may be an origin of ferromagnetism. A belt scrolling model was proposed for explaining the formation process of CMTs, including:

(a) During heating, acetylene gas molecules are pyrolyzed into linear chains.
(b) During cooling, the linear chains are parallel arranged to form hexagonal structure with the chain along the crystallographic c-axis. At the same time, cross-linking reaction between adjacent chains occurs to some extent to form belts with various cross-linking degree.
(c) The belts are then scrolled tighter and tighter to form macrotubes due to thermal stress and/or anisotropic microstructure of tubes.

5.8 Graphane[10] and Graphone

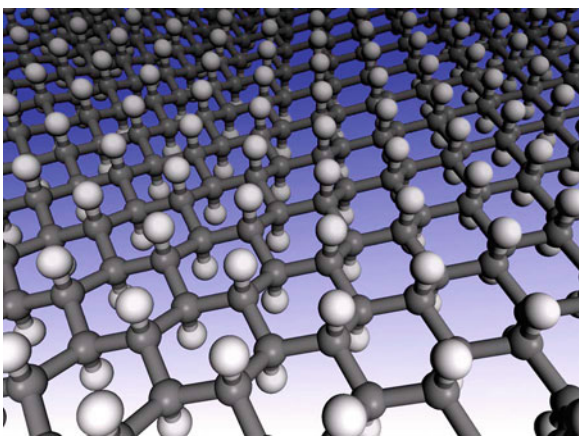

[10]Graphane image is reproduced with permission of *APS Physics* (*Phys. Rev. B*, **2007**, *75*, 153,401).

In addition to *graphene*, *graphyne*, and *graphdiyne*, the 2D materials also include *graphone* and *graphane* (strictly, having hydrogen, they cannot be considered as carbon allotropes), which are hydrogenated forms of graphene [165, 166]. According to *Novoselov* [167], although graphite is known as one of the most chemically inert materials, the graphene can react with atomic hydrogen, which transforms this highly conductive zero-overlap semimetal into an insulator. Graphane is a hydrogenated sheet of graphene, where a primitive graphane cell contains two carbon atoms and two hydrogen atoms. The difference in this case is that the graphene sheet is 100% hydrogenated as opposed to 50% hydrogenated graphone. However, the structural parameters are similar. There is roughly a 5° difference in the C–C–C bond angle, while there is less than 0.1 Å difference in the C–C bond lengths. Unlike graphone, graphane has been successfully synthesized using a couple of different methods. Main features of graphane are as follows:

- This (single layer) is a 2D polymer of carbon and hydrogen with the formula unit $(CH)_n$ where n is large (a form of hydrogenated graphene, a 2D form of carbon alone).
- It is the fully saturated version of graphene. Ideally, every carbon atom of the graphene layer is covalently bonded to a hydrogen atom.
- Carbon bonds in graphane are in sp^3 configuration (graphene has sp^2 bond configuration), thus graphane is a 2D analog of cubic diamond.
- The length of the C–H bonds is about 1.10 Å which is typical for such bonds as found in organic chemistry.
- The average length of the C–C bonds is close to the ideal single C–C bonds in diamond.
- Graphane is a semiconducting material with a substantial direct electronic band gap about 3.5 eV [168].
- Room temperature ferromagnetism was observed in partially hydrogenated graphene.
- The transition from graphene to graphane is that of an electrical conductor, to a semiconductor, and ultimately to an electrical insulator.
- Hydrogenation of graphene on substrate affects only one side, preserving hexagonal symmetry.
- Hydrogenation can be accomplished (1) via low-pressure H_2 plasma, (2) in high-pressure H_2 atmosphere, or (3) via wet chemistry (solution)-based approaches. Typical graphene hydrogenation process is shown in Fig. 5.83.
- The hydrogenation occurs due to the hydrogen ions from the plasma and not due to the fragmentation of water adsorbates on the graphene surface by highly accelerated plasma electrons.
- Partially hydrogenated graphene can be produced using thermal exfoliation of graphite oxide in H_2 atmosphere under high pressure (60–150 bar) and temperature (200–500 °C).
- Hydrogenated graphene can be also further derivatized because of its extended reactivity in comparison with unmodified graphene.

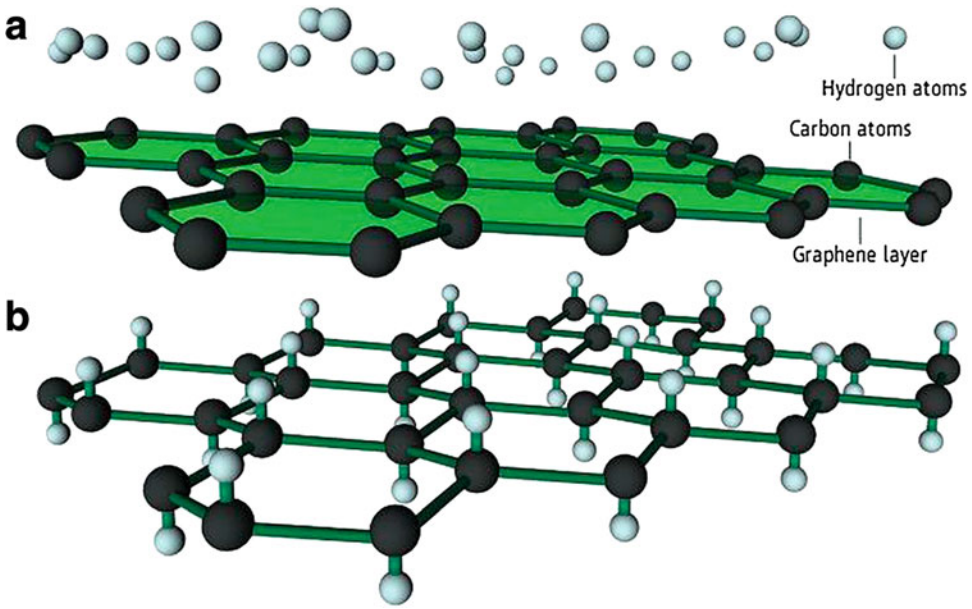

Fig. 5.83 Graphene hydrogenation progress. (**a**) A graphene layer, where delocalized electrons are free to move between carbon atoms, is exposed to a beam of hydrogen atoms. (**b**) In nonconductive graphane, hydrogen atoms bond to their electrons with electrons of carbon atoms and pull the atoms out of the plane [170]. (Reproduced with permission of *Springer*)

- Hydrogenation opens a band gap of up to 3.7 eV, depending on the hydrogenation level and conformation, leading to the fluorescence of highly hydrogenated graphene.
- The reaction of graphene with hydrogen is reversible, so that the original metallic state, the lattice spacing, and even the quantum Hall effect can be restored. The metallic character of graphene from graphane can be recovered by annealing graphane in Ar atmosphere at 450 °C.
- Dehydrogenation of graphane can be laser-induced [169].
- Applying an external electric field to a fully hydrogenated graphene can remove H atoms from one side of graphane, forming graphone.
- It is also possible to completely hydrogenate multilayer graphene to form stacked sequences of, e.g., *chair* isomers, or, alternatively, only the top and bottom layer are hydrogenated from one side, resulting in a thin diamond films.
- The wet chemical methods are based on the reduction of oxygen functionalities present on the graphene oxide surface, for instance, ketone and carboxylic acids can be reduced to hydroxyls together with carbon atom hydrogenation.

Varieties of Graphane Structures The three best-known and most stable graphane isomers are, namely, the chair, stirrup, and boat configuration, together with two other isomers (Fig. 5.84) [171]. The *stirrup* configuration (also called washboard or zigzag configuration; this is an interesting isomer of graphane, proposed on the basis of DFT calculations [172], in which the C–H bonds of a hexagon alternate in three-up–three-down fashion on either side of the sheet) is more stable than the so-called boat configuration. Also, a 2D nanomaterial (good electrical insulator having a high specific heat capacity), which is a form of hydrogenated penta-graphene and called *penta-graphane* (Fig. 5.85), was obtained by adding hydrogen atoms to the sp^2-bonded carbon atoms of penta-graphene (penta-graphene has sp^2- and sp^3-bonded carbon atoms) [173]. Penta-graphane has diamond-like structure with sp^3 hybridization. Also, graphanes can have various C/H ratios. A more promising case of single-side adsorption is C_4H (Fig. 5.86). This structure is built from H pairs in the very stable *para* configuration in which atoms are adsorbed on opposite C atoms in the graphene hexagons [174].

Multilayer Structures A hydrocarbon called hydrographite (a black solid thermally stable under ambient conditions, consisting of graphane sheets in the chair conformation stacked along the hexagonal c axis in the −ABAB− sequence, with hexagonal crystal structure, Fig. 5.87), with the composition close to CH, was shown to be formed from graphite and gaseous hydrogen at pressures above 2 GPa and temperatures from 450 to 700 °C [175]. Being heated in vacuum, it decomposes into graphite and molecular hydrogen at temperatures from 500 to 650 °C. Heating above 720–750 °C in an H_2 gas compressed to 7.5 GPa transforms hydrographite to methane and/or other light hydrocarbons.

Properties of Graphane Fully hydrogenated graphene contains only sp^3-hybridized C atoms with four bonding partners (3 C and 1 H), so the ideal graphane isomers are not expected to show any interesting magnetic properties. Magnetism only occurs

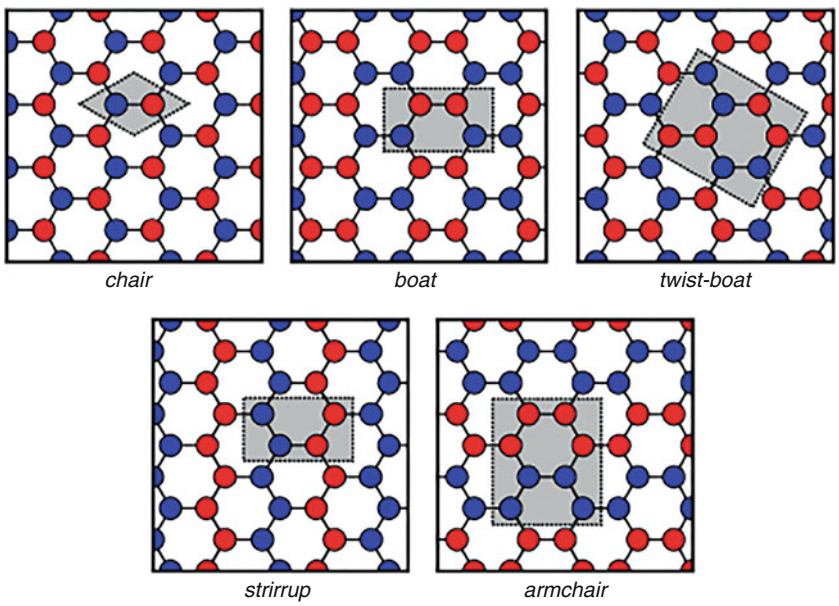

Fig. 5.84 Five isomers of graphane in which every C atom is equivalent. Blue and red colors indicate H adsorption, respectively, above and below the graphene layer. (Reproduced with permission of *Wiley*)

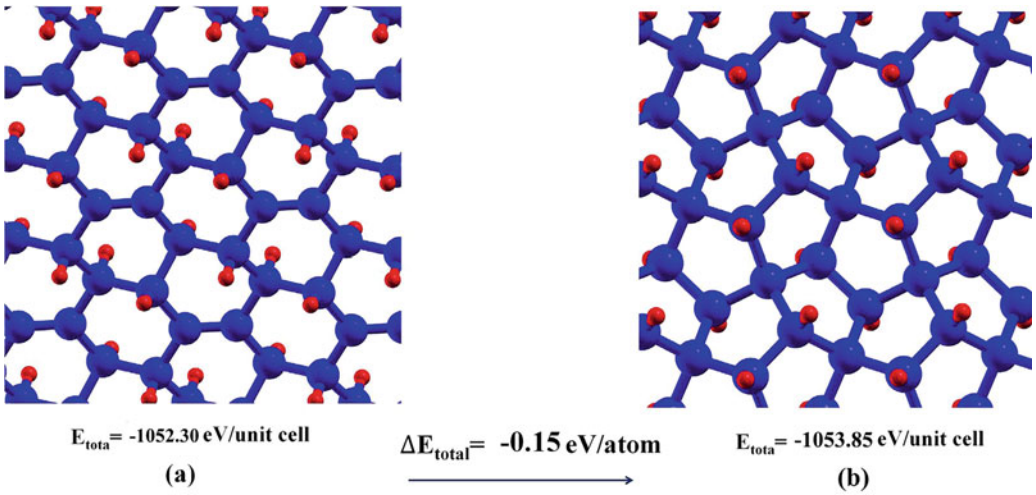

Fig. 5.85 Total energy of (**a**) C_6H_4 (not fully hydrogenated graphane) and (**b**) penta-graphane. Blue and red spheres represent carbon and hydrogen atoms, respectively. (Reproduced with permission of *Taylor and Francis*)

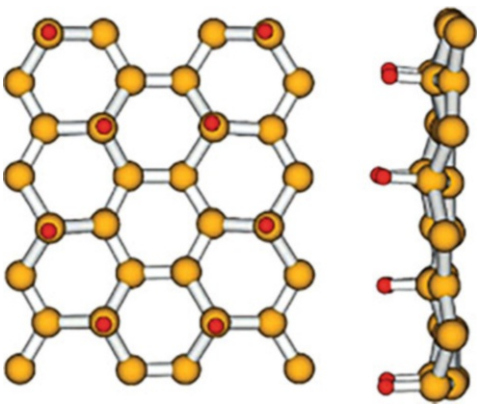

Fig. 5.86 Top and side view of the C_4H crystal structure. (Reproduced with permission of *Wiley*)

at defect sites (missing H atoms) and in partially hydrogenated graphene. In respect of mechanical properties, the hydrogenation reduces the strength of graphene because the strong aromatic bond network is replaced with single σ bonds. Experimental values for Young's modulus of graphane are not available at present, but they are expected to be lower than the theoretical value due to the presence of defects. The 2D nature of graphane has a significant impact on its optical properties and reduces the optical band gap significantly. In case of graphane nanoribbons, their optical properties were found to be independent of their edge shapes and widths. In addition, the vibrational properties of graphene fluoride and graphane were studied, showing that both sp^3-bonded derivatives of graphene have different phonon dispersion relations and phonon densities of states [176].

Vacancies and Foreign Atoms/Groups The properties of graphane can be controlled by its interaction with various metallic ions [177]. Graphane can be further doped with Fe, Li, Ca, or Ge or functionalized with –OH, -F, or $-NH_2$ groups. Potentially many derivatives of graphane can be fabricated by changing the substrate atoms (like C, Si, Ge, P) and the surface atoms (like H, –OH, $-NH_2$, He, Li, Fe, Mn, and all the VIIA element). The impurities can be utilized for the modification of electronic and magnetic properties of graphane. In particular, fluorine-doped graphane is very sensitive to the doping configuration. In addition, the strong covalent bonds of graphene can be broken, and various vacancies are formed due to, e.g., continuous exposure to the high-energy electron beam or irradiation with low-energy Ar^+.

Electronic and magnetic properties of graphene can be modulated by various techniques such as synthesis of graphanes with different C/H ratios, formation of vacancies, application of strain, and dimensional reduction. Studies of the electronic structure of graphane with hydrogen vacancies, which are supposed to occur in the process of hydrogenation of graphene (it is always possible that a small amount of H vacancies remains after a hydrogenation process or occurs by means of physical or chemical desorption), revealed that a continuous chain-like distribution of hydrogen vacancies results in conduction of linear

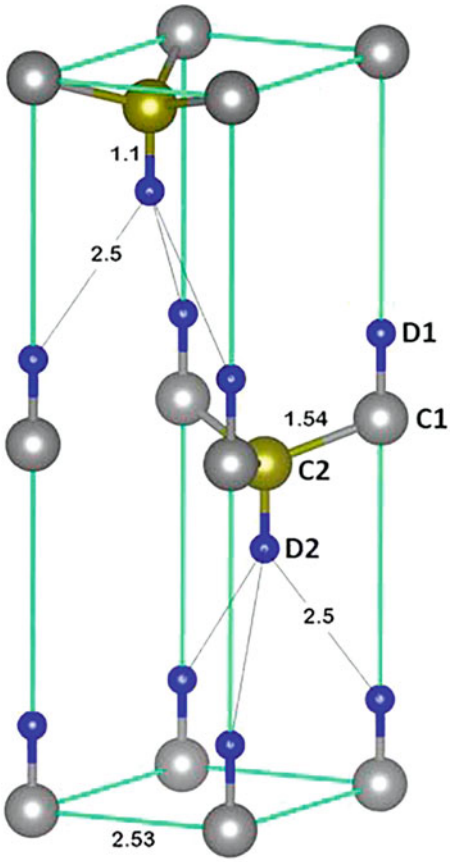

Fig. 5.87 The $P6_3mc$ structure of a graphane crystal. Large spheres represent C atoms; small spheres stand for D atoms. The atoms labeled C1 and D1 sit on the 2a positions; those labeled C2 and D2 are on the 2b positions. Numbers indicate the interatomic distances in Angstroms. (Reproduced with permission of the *Elsevier Science*)

dispersion, much like the transport on a superhighway cutting through the jungle of hydrogen [178]. H vacancies in graphane produce defect states that appear in the graphane bandgap. Magnetic moments can also be generated depending on whether there are unpaired electrons in the configuration. Studies of the role of H frustration (this is a configuration where the sequence of alternating up and down H atoms is broken (frustrated)) in graphane-like structures showed that a significant percentage of uncorrelated H frustrated domains are formed in the early stages of the hydrogenation process leading to membrane shrinkage and extensive membrane corrugations [179]. The net result is a decrease of the carbon–carbon distances in relation to the ideal graphane values.

A certain attention is also paid to combined graphane/graphene composites, i.e., containing distinct grades of hydrogenation in different zones; for instance, electronic transport properties of zigzag graphane/graphene nanoribbons [180] and magnetic properties of graphene superlattices, modeled with a repeated structure of pure and hydrogenated graphene-graphane strips, were DFT-studied [181]. As graphene is charged, localized regions of graphene are transformed from sp^2 bonded into sp^3 bonded, giving rise to hydrogen-less graphane, which, if experimentally realized, may lead to a way of combining graphene and graphane in the same material [182]. It was suggested that the combination of graphene and graphane might be the basis of future electronic devices.

Potential Applications Graphane may found applications in various fields such as hydrogen storage, piezoelectricity, spintronics, thermoelectrics, explosive detection, and sensing and biosensing devices. Thus, DFT was used to investigate the sensing property of graphane toward CO, H_2O, and NO_2 gas molecules [183]. Curiously, the pristine graphane sheet was found not to have sufficient affinity toward the mentioned gas molecules; the defected sheet (removing few surface H atoms) had a strong affinity toward the gas molecules. While CO and H_2O are weakly physisorbed, the NO_2 molecules are strongly chemisorbed to the defected graphane sheet. Various N-substituted/grafted graphanes can also adsorb CO_2. It was found that the presence of co-adsorbed H_2O on the surface promotes CO_2 adsorption on both N and NH_2 sites, with highly exothermic adsorption energies [184]. In case of other inorganic gases, neither a pristine graphane sheet nor the sheet defected by removing a few surface H atoms has sufficient affinity for either H_2S or NH_3 gas molecules [185]. However, a graphane sheet doped with Li adatoms shows a strong sensing affinity for both mentioned gas molecules.

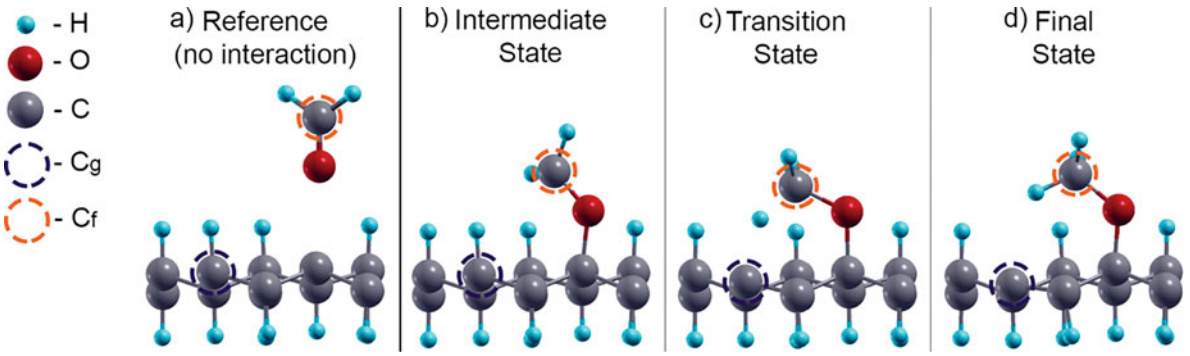

Fig. 5.88 (**a**) The zero-energy state (substrate and molecule with no interaction), (**b**) formaldehyde attached to the surface (intermediate state), (**c**) transition state (hydrogen abstraction), and (**d**) final state, hydrogen attachment to the molecule. (Reproduced with permission of *Elsevier Science*)

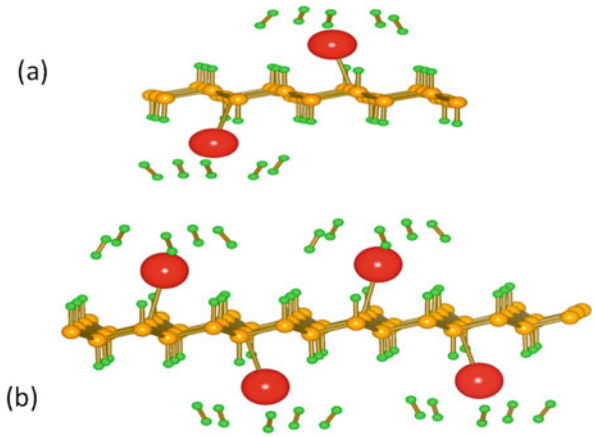

Fig. 5.89 (**a**) The optimized structure of the fully hydrogenated CHCa with maximum number of hydrogen molecules adsorbed around each Ca atom. (**b**) The extended structure of relaxed CHCa with adsorbed hydrogen molecules. (Reproduced with permission of the *AIP Publishing*)

Organic molecules can also be sensed by graphane. Thus, the process of adsorption of a formaldehyde molecule on a hydrogenated graphene substrate was calculated to be a free radical-initiated reaction [186], beginning at a hydrogen vacancy on the graphane layer, in which the oxygen atom of the formaldehyde molecule attaches (Fig. 5.88). Then, the nearest hydrogen atom is abstracted by the carbon atom of the formaldehyde, forming a stable molecule and leaving behind a new dangling bond on the graphane substrate. The energy barrier for the entire process was found to be 0.56 eV.

The advantage of using graphane as H_2 storage material is its nano-size, large stability, and relatively stronger graphane-metal binding. It was predicted that with a doping concentration of 11.11% of Ca on graphane sheet (Fig. 5.89), a reasonably good H_2 storage capacity of 6 wt. % could be attained [187]. Also, the detection of explosives is one of the main concerns for a secure and safe society. Toxic trinitrotoluene (TNT), main component in explosives, can be detected in seawater using partially hydrogenated graphene and graphene. Spintronics is another possible application area [188].

Graphone (first predicted in 2009) is the midpoint between *graphene* and *graphane* in which the graphene sheet is only partially hydrogenated. Unlike graphane (100% hydrogenation) and graphene (0% hydrogenation), graphone is a graphene sheet with 50% hydrogenation and stoichiometry C_2H. Additionally, the hydrogen atoms are only on one side of the carbon sheet, resulting in a mixture of hybridized sp^2 and sp^3 carbon atoms. Many intermediate forms can also exist.

Main features of graphone are as follows:

- Graphone is a graphene sheet with 50% hydrogenation and stoichiometry C_2H.
- The hydrogen atoms are only on one side of the carbon sheet, resulting in a mixture of hybridized sp^2 and sp^3 carbon atoms.
- Graphone is a ferromagnetic semiconductor with an indirect band gap of 0.43 eV.
- The stability of graphone is very weak, because the H atoms try to form pairs. However, graphone is considered as a stable structure at room temperature.
- Graphone has a small in-plane stiffness (74%) as well as Poisson ratio (67%) compared to graphene, but similar to those of graphane.
- The effect of hydrogenation on the mechanical properties is saturated when the graphene is only 50% hydrogenated.
- Graphone still has yet to be synthesized easily.

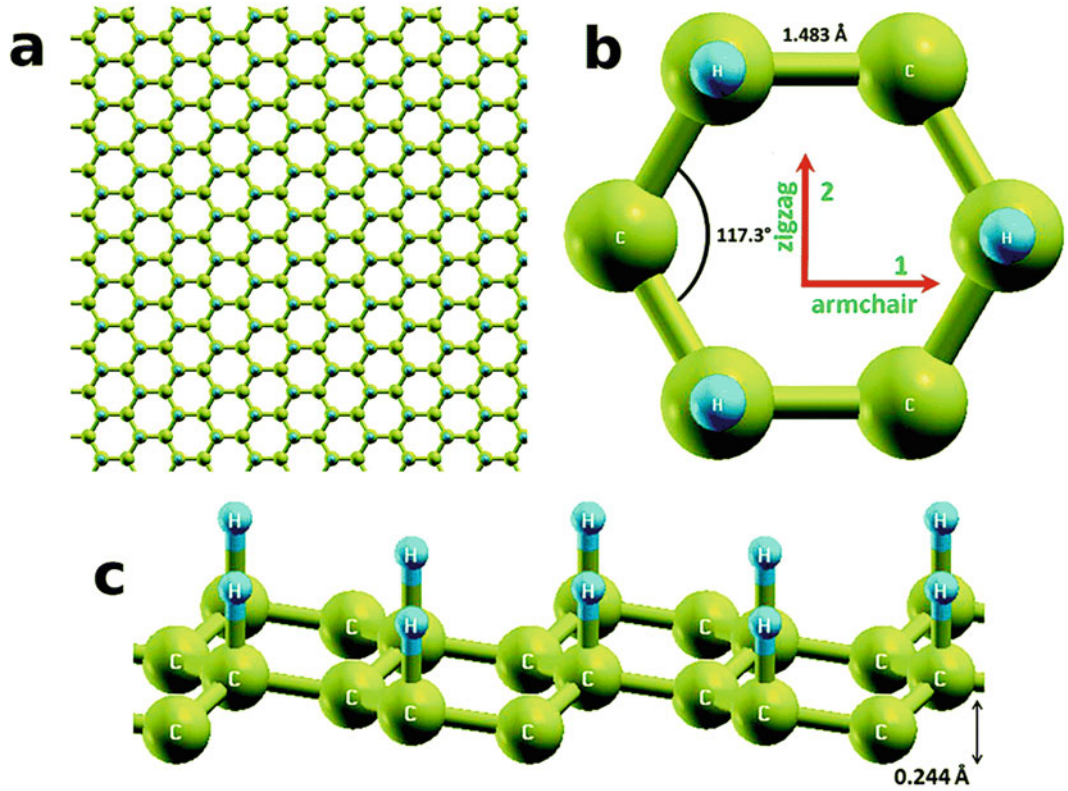

Fig. 5.90 Configurations of graphone. (**a**) Graphone plane; (**b**) top view and directions; (**c**) side view. (Reproduced with permission of the *Royal Society of Chemistry*)

The *synthesis* of graphone can be achieved by desorption of hydrogen from graphane, but a reliable method for synthesizing graphone is yet to be found. The synthesis of graphone bound to a Ni(111) surface showed that the hydrogenation of graphene with atomic hydrogen indeed leads to graphone, that is, a hydrogen coverage of 4.2 wt.% [189]. The dehydrogenation of graphone reveals complex desorption processes that are attributed to coverage-dependent changes in the activation energies for the associative desorption of hydrogen as molecular H_2.

Structural Peculiarities [190] It was stated [165] that when half of the carbon atoms are hydrogenated, strong σ bonds are formed between the carbon and hydrogen atoms. These σ bonds not only disrupt the usual π bonding network of graphene that leads to the metallic and nonmagnetic two-dimensional sheet but also cause the electrons on the carbon atoms not bonded to hydrogen to become localized and unpaired. Graphone possesses a graphene-like honeycomb structure where there are two typical directions named "armchair" and "zigzag" (Fig. 5.90) [191]. The instability of a free-standing boatlike and armchairlike one-sided hydrogenated/fluorinated graphene nanoribbon (Fig. 5.91), i.e., graphone/fluorographene, was studied using *ab initio*, semiempirical, and large-scale molecular dynamics simulations [192]. The packed, spiral structures exhibit an unexpected localized highest occupied molecular orbital and lowest occupied molecular orbital at the edges with increasing energy gap during rolling. These rolled hydrocarbon structures are stable beyond room temperature up to at least $T = 1000$ K within the simulation time of 1 ns.

Other properties and possible applications. The temperature dependence of the characteristic time of disordering of graphone via hopping of hydrogen atoms to neighboring carbon atoms was established directly [193]. The activation energy of this process was determined at $E_a = (0.05 \pm 0.01)$ eV. This small value of *Ea* is indicative of the extremely low thermal stability of graphone, making this nanocarbon material unpromising for practical use in electronic devices. On the contrary, the DFT modellings performed showed that fluorinated graphone is rather more stable than the hydrogenated one [194], which makes it more suitable for further applications in electronic and spintronic devices. Graphone were examined as a possible material for FETs and organic ferroelectrics.

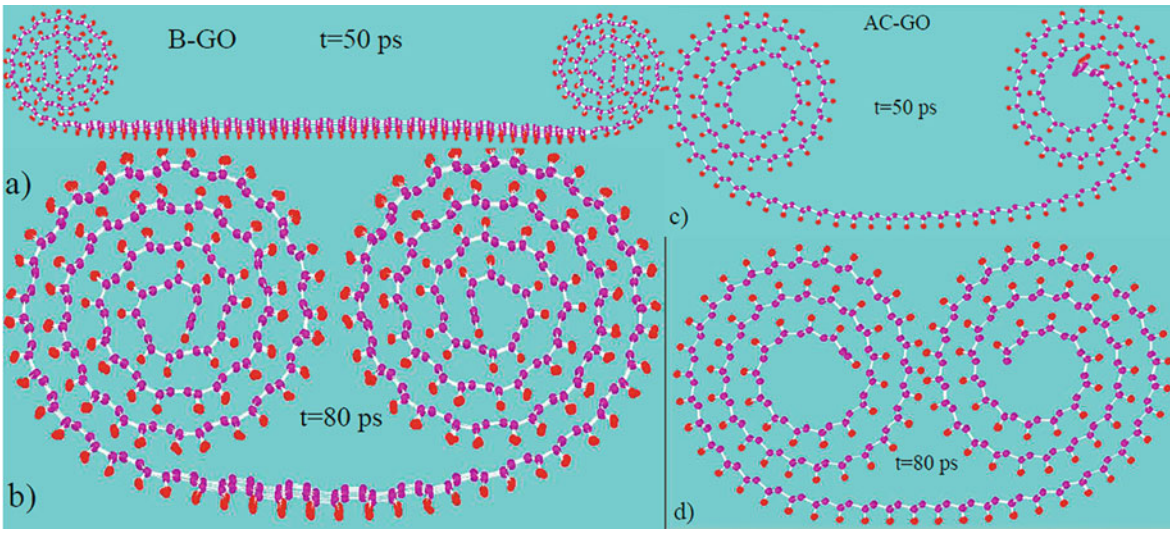

Fig. 5.91 The rolled boatlike (left) and armchairlike (right) graphone nanoribbons after (**a**), (**c**) t = 50 ps and (**b**), (**d**) t = 80 ps. These systems are stable up to at least 1000 K. (Reproduced with permission of *APS Physics*)

5.9 M-Carbon[11]

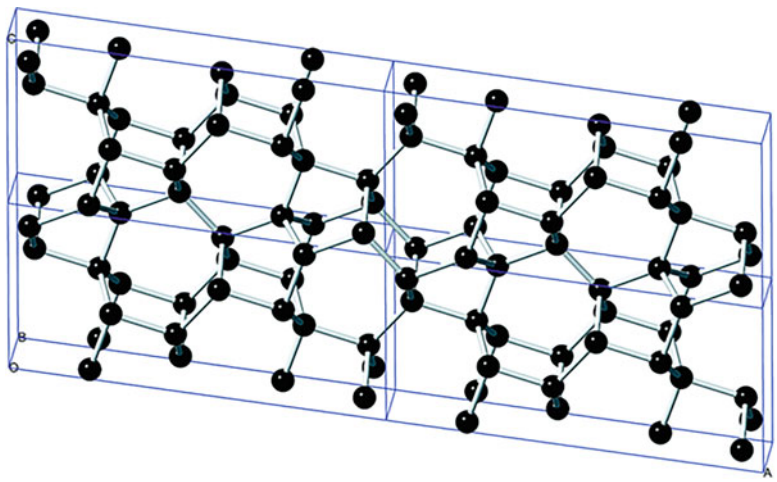

Despite that the news about monoclinic C-centered carbon (M-carbon) appeared as far back as in 1963, passing a series of intermediate studies, the possibility of existence of this structure and formation from graphite by its overcompressing at room temperature were proven in 2012. Main features of the M-carbon are as follows [195]:

- A monoclinic C2/*m* structure (8 atoms/cell).
- It is stable over cold-compressed graphite above 13.4 GPa.
- The hardness and bulk modulus of M-carbon are known to be 83.1 and 431.2 GPa, respectively, which are comparable to those of diamond.

There are several distinct reports on M-carbon varieties. In particular, it was shown that the monoclinic phase carbon allotrope, *C*2/*m*-16 carbon, is a potential superhard material with a hardness of 59.5 GPa and a semiconductor with a wide and indirect band gap of 4.20 eV [196]. *C*2/*m*-20 carbon (containing sp^3-hybridized covalent bonds) is mechanically stable and dynamically stable at 0 GPa and 100 GPa. *C*2/*m*-20 carbon has a larger bulk modulus of 412 GPa, a larger shear modulus of 463 GPa, a larger Young's modulus of 1010 GPa, and a hardness of 70.6 GPa, which means that it is a superhard material with potential technological and industrial applications. In addition, *C*2/*m*-20 carbon is an indirect and wide semiconductor with a

[11]Reproduced with permission of the *Royal Society of Chemistry* (*RSC Adv.*, **2016**, *6*, 32,740–32,745).

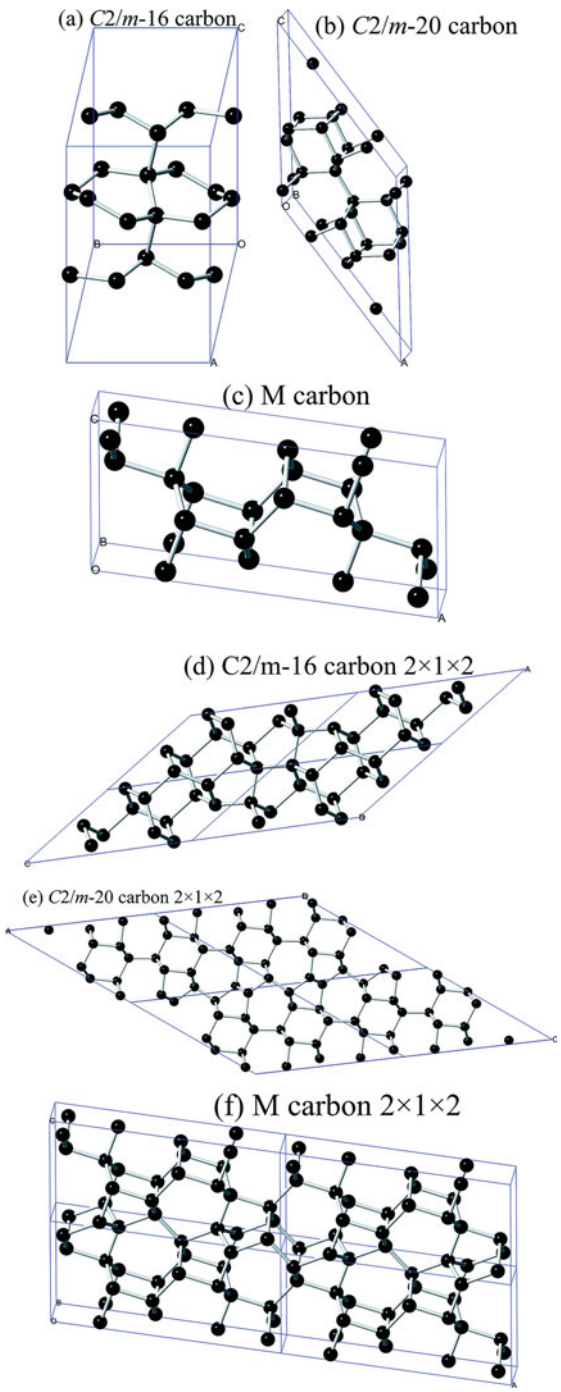

Fig. 5.92 The crystal structure of *C*2/*m*-16 carbon (**a**), *C*2/*m*-20 carbon (**b**), M-carbon (**c**), *C*2/*m*-16 carbon along the [010] direction (**d**), *C*2/*m*-20 carbon along the [010] direction (**e**), and M-carbon along the [010] direction (**f**). At zero pressure, *C*2/*m*-20 carbon contains five inequivalent crystallographic sites, occupying the 4i (0.07488, 0.0, −0.51860), 4i (−0.50848, 0.0, −0.33322), 4i (0.75150, 0.0, −0.04876), 4i (−0.99004, 0.0, −0.90598), and 4i (−0.36506, 0.0, −0.73151) positions, respectively. (Reproduced with permission of the *Royal Society of Chemistry*)

band gap of 5.10 eV. The most extraordinary thing is that the band gap increases with increasing pressure. The crystal structures of *C*2/*m*-20 carbon, *C*2/*m*-16 carbon, and M-carbon are illustrated in Fig. 5.92. *C*2/*m*-20 carbon, *C*2/*m*-16 carbon, and M-carbon all belong to the *C*2/*m* phase. In their crystal structures, six-membered carbon rings exist in *C*2/*m*-16 carbon and *C*2/*m*-20 carbon. In addition, *C*2/*m*-16 carbon and *C*2/*m*-20 carbon also have five-membered carbon rings and seven-membered carbon rings, while M-carbon only has five-membered carbon rings and seven-membered carbon rings.

In addition, an allotrope of carbon, a transparent, superhard material, called M_{10}-carbon (Fig. 5.93), with *P*2/*m* symmetry was identified during an ab initio minima-hopping structural search [197]. This structure, consisting purely of sp^3 bonds, was proposed to be more stable than graphite at pressures above 14.4 GPa. It has a high bulk modulus and is almost as hard as diamond.

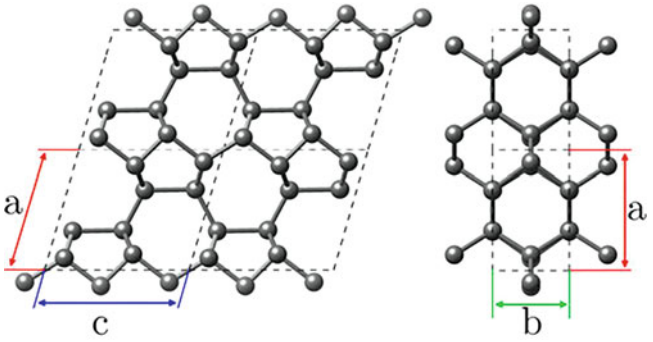

Fig. 5.93 The structure of *M*10-carbon from two different angles. The left panel shows the five- and seven-membered rings, while the right panel reveals the six-membered rings. (Reproduced with permission of *Springer*)

5.10 Q-Carbon[12]

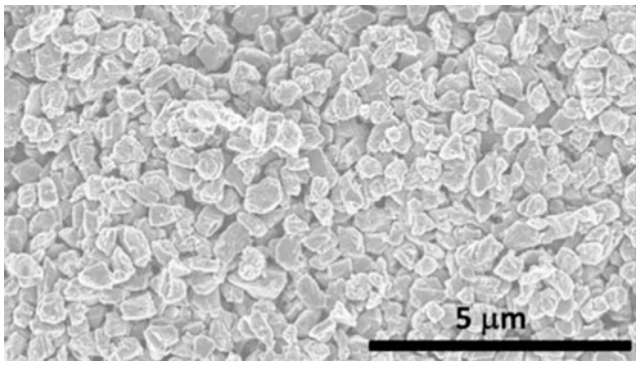

Q-carbon ("quenched") was discovered in 2015. The Q-carbon is formed as result of quenching amorphous carbon from super undercooled state by using high-power nanosecond laser pulses (nanosecond laser melting). Its main features are as follows [198]:

- Q-carbon is ferromagnetic (estimated Curie temperature of about 500 K and saturation magnetization value of 20 emu g^{-1}) and electrically conductive.
- Q-carbon possesses an amorphous structure, consisted of a mixture of sp^2 and sp^3 bonding (mostly sp^3, 75–85%).
- It can be obtained by carbon conversion using a high-powered laser pulses. The formation of Q-carbon is achieved, when amorphous carbon films are heated to about 4000 K and melted and quenched rapidly [199].
- Q-carbon was found to be 60% harder than diamond-like carbon.
- It can be used in creating artificial body components, improving instruments like deep water drills, and producing much brighter, long-lasting screens for televisions and cellphones.
- Nanodiamonds, microdiamonds, nanoneedles, microneedles, and thin films are readily formed from the Q-carbon depending upon the time allowed for growth during the quenching period.
- Sometimes it glows when exposed to low levels of energy.
- It is quite inexpensive to make, and maybe, it is a replacement of diamond.
- Q-carbon can be made to take multiple forms, from nanoneedles to large-area diamond films.
- It took researchers only 15 min to make 1 karat of Q-carbon.

Q-carbon could have a series of applications: high-powered electronic and photonic devices, high-speed machining, deep sea drilling, efficient field emission displays, medicinal purposes (like nanoneedles, microneedles, nanodots, and films), and sensor applications (biomedical sensing, single-photon sensors, nanoscale electronic and magnetic sensing, single-spin magnetic resonance and fluorescent biomarkers), among others [200].

[12]Reproduced from https://newatlas.com/q-carbon-new-phase-of-carbon/40668/ (Q-carbon film covered with microdiamonds).

5.11 T-Carbon[13]

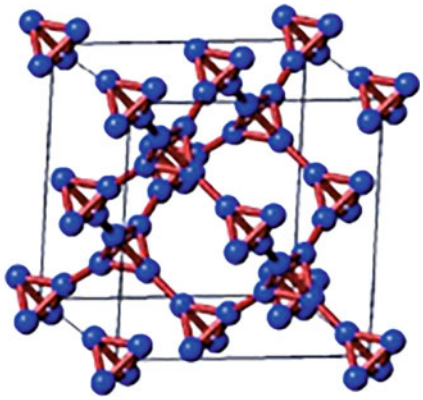

This carbon allotrope was first proposed in 2011. In the T-carbon, every carbon atom in diamond is replaced with a carbon tetrahedron (hence "T-carbon"). T-carbon possesses the same space group $Fd\bar{3}$ m as diamond [201]. Main features of T-carbon are presented as follows:

- Each unit cell of the T-carbon structure contains two tetrahedrons with eight carbon atoms.
- T-carbon has a density 1.50 g/cm^3.
- Semiconductor with a direct band gap about 3.0 eV has a Vickers hardness 61.1 GPa lower than diamond but comparable with cubic boron nitride.
- It would have wide applications in photocatalysis, adsorption, hydrogen and lithium storage (since it has large interspaces between atoms), and aerospace materials [202].
- T-carbon could have astronomical implications as a potential component of interstellar dust and carbon exoplanets.

T-carbon with a nanowire-like morphology was synthesized by picosecond-pulsed laser irradiation of a MWCNT suspension in methanol [203]. The diameters of most T-carbon NWs were found to be in the range 10–20 nm, similar to the diameter distribution of the starting shortened MWCNTs. sp^2 hybridization in MWCNTs was confirmed to be transformed to sp^3 hybridization. The structure is diamond-like with each carbon atom replaced by a carbon tetrahedron (Fig. 5.94), consistent with the theoretically predicted T-carbon with a lattice constant of 7.52 Å. Among other varieties of T-carbon, a

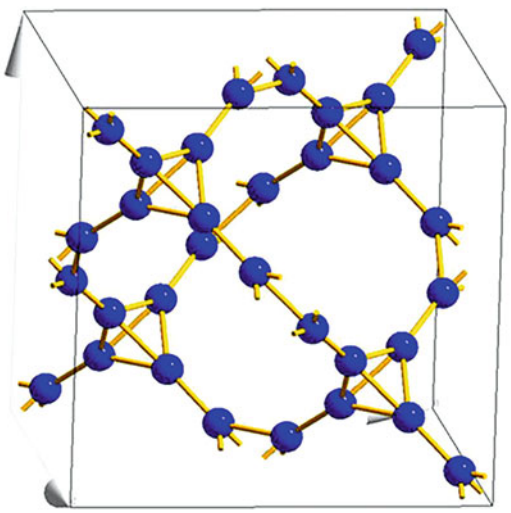

Fig. 5.94 Structural model of T-carbon ($Fd\bar{3}m$, lattice constant = 7.80 Å). (Reproduced with permission of *Nature*)

[13]Reproduced from https://www.nextbigfuture.com/2011/04/t-carbon-novel-carbon-allotrope.html.

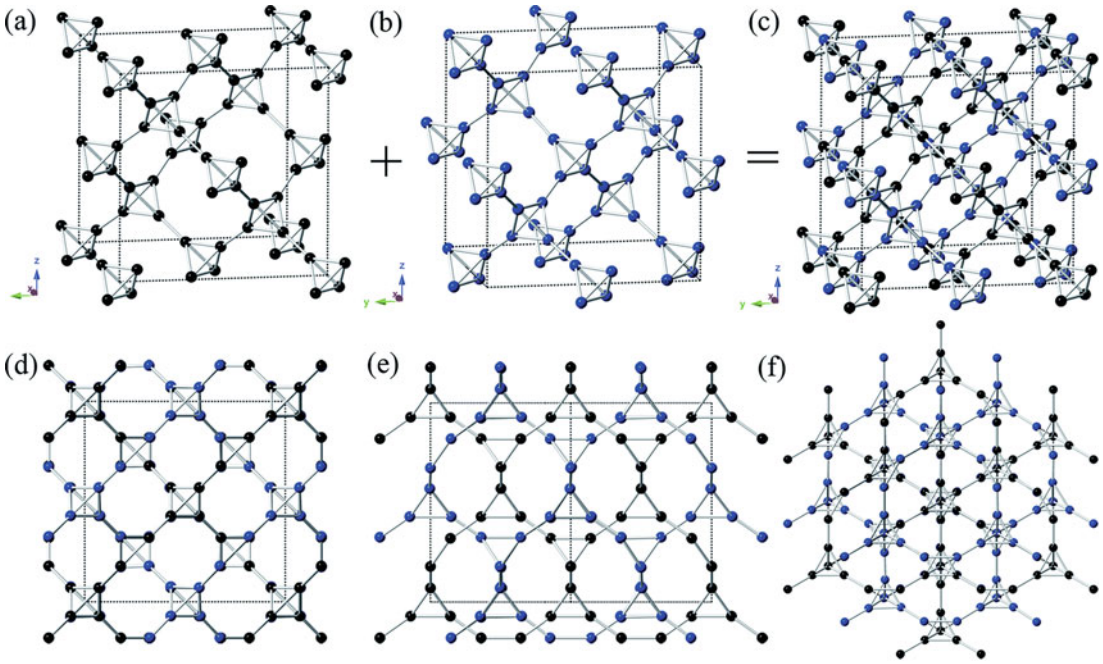

Fig. 5.95 (**a**) The crystal structure of T-carbon. (**b**) T-carbon moving 1/2 lattice vector along a axis. (**c**) The crystal structure of T-II carbon. (**d**–**f**) Views from [100], [110], and [111] directions of T-II carbon, respectively. (Reproduced with permission of the *Royal Society of Chemistry*)

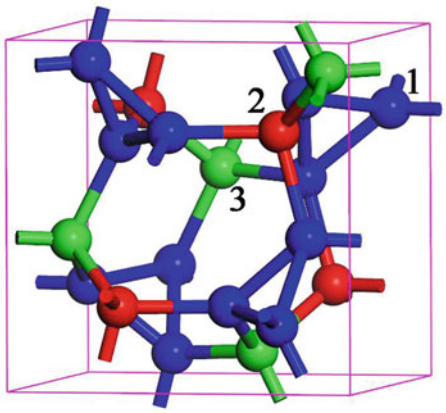

Fig. 5.96 Schematic depiction of the structure of C_{20}-*T*-carbon. C_{20}-*T*-carbon has $P2_13$ symmetry with a lattice constant of 4.945 Å. The carbon atoms occupy the 12b(0.4274, 0.7301, 0.8103), 4a(0.2694, 0.2307, 0.7694), and 4a(0.0894, 0.4106, 0.5894) Wyckoff positions, which are denoted by C_1(blue), C_2(red), and C_3(green), respectively. (Reproduced with permission of the *IOP Science*)

modulated T-carbon-like carbon allotrope (T-II carbon, structurally similar to T-carbon, having the smallest unit of T-carbon, Fig. 5.95) was predicted by means of first-principles calculations [204]. This structure has eight atoms in the unit cell, possesses the $Pn\bar{3}m$ space group, and can be derived by stacking up two T-carbons together. T-II carbon is a semiconductor with band gap 0.88 eV and has a higher hardness (27 GPa) than that of T-carbon (5.6 GPa). Also, a superhard carbon allotrope named C_{20}-T was also predicted [205], which belongs to a cubic T symmetry with space group $P2_13$ and possesses all sp^3-hybridized bonding network with 20 atoms in its primitive unit cell (Fig. 5.96). Interestingly, despite the fact that C_{20}-T-carbon has a porous structure with large cavities, the calculations identified its superhard properties with the Vickers hardness of 72.76 Gpa. This carbon phase has great potential for application in mechanical devices, hydrogen storage, and related fields.

References

1. M.P. Manoharan, H. Lee, R. Rajagopalan, H.C. Foley, M.A. Haque, Elastic properties of 4–6 nm-thick glassy carbon thin films. Nanoscale Res. Lett. **5**, 14 (2009)

2. K. Jurkiewicz, S. Duber, H.E. Fischerd, A. Burian, Modelling of glass-like carbon structure and its experimental verification by neutron and X-ray diffraction. J. Appl. Crystallogr. **50**, 36–48 (2017)
3. O.J.A. Schueller, S.T. Brittain, G.M. Whitesides, Fabrication of glassy carbon microstructures by pyrolysis of microfabricated polymeric precursors. Adv. Mater. **9**(6), 477–480 (1997)
4. J. Bauer, A. Schroer, R. Schwaiger, O. Kraft, Approaching theoretical strength in glassy carbon nanolattices. Nat. Mater. **15**, 438–443 (2016)
5. C.M. Lentz, B.A. Samuel, H.C. Foley, M.A. Haque, Synthesis and characterization of glassy carbon nanowires. J. Nanomater **2011**, (2011). Article ID 129298, 8 pp
6. A.F. Goncharov, Graphite at high pressures: Pseudomelting at 44 GPa. Sov. Phys. JETP **71**(5), 1025–1027 (1990)
7. M. Yao, X. Fan, W. Zhang, et al., Uniaxial-stress-driven transformation in cold compressed glassy carbon. Appl. Phys. Lett. **111**, 101901 (2017)
8. M. Hu, J. He, Z. Zhao, et al., Compressed glassy carbon: An ultrastrong and elastic interpenetrating graphene network. Sci. Adv. **3**, e1603213 (2017)
9. J. Csontos, Z. Toth, Z. Pápa, et al., Periodic structure formation and surface morphology evolution of glassy carbon surfaces applying 35-fs–200-ps laser pulses. Appl. Phys. A Mater. Sci. Process. **122**, 593 (2016)
10. M. Collaud Coen, Functionalization of graphite, glassy carbon, and polymer surfaces with highly oxidized sulfur species by plasma treatments. J. Appl. Phys. **92**, 5077–5083 (2002)
11. I. Emahi, M.P. Mitchell, D.A. Baum, Electrochemistry of pyrroloquinoline quinone (PQQ) on multi-walled carbon nanotube-modified glassy carbon electrodes in biological buffers. J. Electrochem. Soc. **164**(3), H3097–H3102 (2017)
12. F. Campanhã Vicentini, B.C. Janegitz, C.M.A. Brett, O. Fatibello-Filho, Tyrosinase biosensor based on a glassy carbon electrode modified with multiwalled carbon nanotubes and 1-butyl-3-methylimidazolium chloride within a dihexadecylphosphate film. Sens. Actuators B Chem. **188**, 1101–1108 (2013)
13. F. Chekin, S. Bagheri, S. Bee Abd Hamid, Glassy carbon electrodes modified with gelatin functionalized reduced graphene oxide nanosheet for determination of gallic acid. Bull. Mater. Sci. **38**(7), 1711–1716 (2015)
14. S. Robin Nxele, P. Mashazi, T. Nyokong, Surface functionalization of glassy carbon electrodes via adsorption, electrografting and click chemistry using quantum dots and alkynyl substituted phthalocyanines: a brief review. Fourth Conference on Sensors, MEMS, and Electro-Optic Systems, 2017, Proceedings Volume 10036, 100360D
15. M.L. Valenzuela, R. Cisternas, P. Jara-Ulloa, L. Rodriguez, Electroanalytical analysis of glassy carbon electrode modified with COOH- and NO_2- functionalized polyspyrophosphazenes. J. Chil. Chem. Soc. **62**(2), 3515–3518 (2017)
16. I. Kocak, Characterization of the reduction of oxygen at anthraquinone-modified glassy carbon and highly oriented pyrolytic graphite electrodes. Anal. Lett. **50**(9), 1448–1462 (2017)
17. J. Lv, Y. Tang, L. Teng, D. Tang, J. Zhang, Aminobenzene sulfonic acid-functionalized carbon nanotubes on glassy carbon electrodes for probing traces of mercury(II). J. Serb. Chem. Soc. **82**(1), 73–82 (2017)
18. P. Actis, G. Caulliez, G. Shul, et al., Functionalization of glassy carbon with diazonium salts in ionic liquids. Langmuir **24**(12), 6327–6333 (2008)
19. J. Liu, S. Dong, Grafting of diaminoalkane on glassy carbon surface and its functionalization. Electrochem. Commun. **2**(10), 707–712 (2000)
20. M. Balooei, J. Bakhsh Raoof, F. Chekin, R. Ojani, Novel sensor based on 3-mercaptopropyltrimethoxysilane functionalized carbon nanotubes modified glassy carbon electrode for electrochemical determination of Cefixime. Anal. Bioanal. Electrochem. **9**(3), 266–276 (2017)
21. R. Sakthivel, S. Dhanalakshmi, S.-M. Chen, et al., A novel flakes-like structure of molybdenum disulphide modified glassy carbon electrode for the efficient electrochemical detection of dopamine. Int. J. Electrochem. Sci. **12**, 9288–9300 (2017)
22. J. Marwan, T. Addou, D. Bélanger, Functionalization of glassy carbon electrodes with metal-based species. Chem. Mater. **17**(9), 2395–2403 (2005)
23. https://www.2spi.com/catalog/documents/glassy-vitreous-carbon-info.pdf. Accessed on 26 Oct 2017
24. C. Canales, L. Gidi, G. Ramírez, Electrochemical activity of modified glassy carbon electrodes with covalent bonds towards molecular oxygen reduction. Int. J. Electrochem. Sci. **10**, 1684–1695 (2015)
25. J. Miliki, N. Markicevi, A. Jovic, R. Hercigonja, B. Šljuki, Glass-like carbon, pyrolytic graphite or nanostructured carbon for electrochemical sensing of bismuth ion? Process. Appl. Ceramics **10**(2), 87–95 (2016)
26. Y.E. Seidel, R.W. Lindström, Z. Jusys, et al., Stability of nanostructured Pt/glassy carbon electrodes prepared by colloidal lithography. J. Electrochem. Soc. **155**(3), K50–K58 (2008)
27. Y. Jalit, M.C. Rodríguez, M.D. Rubianes, S. Bollo, G.A. Rivas, Glassy carbon electrodes modified with multiwall carbon nanotubes dispersed in polylysine. Electroanalysis **20**(15), 1623–1631 (2008)
28. S.E. Subramani, T.V. Vineesh, T. Priya, V. Kathikeyan, N. Thinakaran, Electrochemical detection of Pb(II) ions using glassy carbon electrode surface modified by functionalized mesoporous carbon. Sens. Lett. **15**(4), 320–327 (2017)
29. C. Sun, L. Rotundo, C. Garino, Electrochemical CO_2 reduction at glassy carbon electrodes functionalized by Mn^I and Re^I organometallic complexes. ChemPhysChem **18**(22), 3219–3229 (2017)
30. A. Braun, J. Ilavsky, S. Seifert, Highly porous activated glassy carbon film sandwich structure for electrochemical energy storage in ultracapacitor applications: Study of the porous film structure and gradient. J. Mater. Res. **25**(8), 1532–1540 (2010)
31. V.D. Chekanova, A.S. Fialkov, Vitreous carbon (preparation, properties, and applications). Russ. Chem. Rev. **1971**(40), 413–428 (1971)
32. C. Garion, Mechanical properties for reliability analysis of structures in glassy carbon. World J. Mech. **4**, 79–89 (2014)
33. N. Komarevskiy, V. Shklover, L. Braginsky, C. Hafner, J. Lawson, Potential of glassy carbon and silicon carbide photonic structures as electromagnetic radiation shields for atmospheric re-entry. Opt. Express **20**(13), 14189–14200 (2012)
34. J. Myalski, B. Hekner, A. Posmyk, The influence of glassy carbon on tribological properties in metal – ceramic composites with skeleton reinforcement. *Additional Conferences (Device Packaging, HiTEC, HiTEN, & CICMT),* 2015, *Vol. 2015*, No. CICMT, (2015) pp. 000121–000124
35. Y. Koval, A. Geworski, K. Gieb, I. Lazareva, P. Müller, Fabrication and characterization of glassy carbon membranes. Journal of Vacuum Science & Technology B, Nanotechnology and Microelectronics: Materials, Processing, Measurement, and Phenomena **32**, 042001 (2014)

36. M. Vomero, E. Castagnola, F. Ciarpella, E. Maggiolini, N. Goshi, E. Zucchini, S. Carli, L. Fadiga, S. Kassegne, D. Ricci, Highly stable glassy carbon interfaces for long-term neural stimulation and low-noise recording of brain activity. Sci. Rep. **7**, 40332 (2017)
37. https://www.alfa.com/es/glassy-carbon/ Accessed on 27 Oct 2017
38. S. Dadkhah, E. Ziaei, A. Mehdinia, T. Baradaran Kayyal, A. Jabbari, A glassy carbon electrode modified with amino-functionalized graphene oxide and molecularly imprinted polymer for electrochemical sensing of bisphenol a. Microchim. Acta **183**(6), 1933–1941 (2016)
39. J. Bakhsh Raoof, R. Ojani, M. Baghayeri, M. Amiri-Aref, Application of a glassy carbon electrode modified with functionalized multi-walled carbon nanotubes as a sensor device for simultaneous determination of acetaminophen and tyramine. Anal. Methods **4**, 1579–1587 (2012)
40. www.orioncarbons.com. Accessed on 31 Oct 2017
41. C.M. Long, M.A. Nascarella, P.A. Valberg, Carbon black vs. black carbon and other airborne materials containing elemental carbon: Physical and chemical distinctions. Environ. Pollut. **181**, 271–286 (2013)
42. https://en.wikipedia.org/wiki/Carbon_black. Accessed on 31 Oct 2017
43. http://www.climatecentral.org/news/black-carbon-second-only-to-co2-in-heating-the-planet-new-study-15465. Accessed on 31 Oct 2017
44. https://birlacarbon.com/learning-center/carbon-black/ Accessed on 31 Oct 2017
45. N. Probst, E. Grivei, Structure and electrical properties of carbon black. Carbon **40**, 201–205 (2002)
46. M. Ozawa, E. Ōsawa, Carbon blacks as the source materials for carbon nanotechnology. In: "*Carbon Nanotechnology*", **2006**, L. Dai. (Ed.), Chapt. 6, p. 127-151. Elsevier: Dordrecht
47. http://www.carbonblack.jp/en/cb/tokusei.html. Accessed on 31 Oct 2017
48. S. Lim, X. Faïn, P. Gino, et al., Black carbon variability since preindustrial times in the Eastern part of Europe reconstructed from Mt. Elbrus, Caucasus, icecores. Atmos. Chem. Phys. **17**, 3489–3505 (2017)
49. C. Garland, S. Delapena, R. Prasad, C. L'Orange, D. Alexander, M. Johnson, Black carbon cookstove emissions: A field assessment of 19 stove/fuel combinations. Atmos. Environ. **169**, 140–149 (2017)
50. A. Guha, B. De Kumar, P. Dha, et al., Seasonal characteristics of aerosol black carbon in relation to long range transport over Tripura in Northeast India. Aerosol Air Qual. Res. **15**, 786–798 (2015)
51. W. Min Hao, A. Petkov, B.L. Nordgre, et al., Daily black carbón emissions from fires in northern Eurasia for 2002–2015. Geosci. Model Dev. **9**, 4461–4474 (2016)
52. Ö. Gustafssona, V. Ramanathan, Convergence on climate warming by black carbon aerosols. PNAS **113**(16), 4243–4245 (2016)
53. V. Ramanathan, G. Carmichael, Global and regional climate changes due to black carbon. Nat. Geosci. **1**, 221–227 (2008)
54. O.A. Al-Hartomy, F. Al-Solamy, A. Al-Ghamdi, et al., Volume 2011. Article ID **521985**, 8 pp (2011)
55. http://www.asahicarbon.co.jp/global_site/product/cb/characteristic.html. Accessed on 31 Oct 2017
56. G. Datt, C. Kotabage, A.C. Abhyankar, Ferromagnetic resonance of $NiCoFe_2O_4$ nanoparticles and microwave absorption properties of flexible $NiCoFe_2O_4$–carbon black/poly(vinyl alcohol) composites. Phys. Chem. Chem. Phys. **19**, 20699–20712 (2017)
57. Q. Zhang, B.-Y. Zhang, Z.-X. Guo, J. Yu, Tunable electrical conductivity of carbon-black-filled ternary polymer blends by constructing a hierarchical structure. Polymers **9**, 404, 11 pp (2017)
58. S.K.H. Gulrez, S. Al-Assaf, G.O. Phillips. Hydrogels: methods of preparation, characterisation and applications. in *Progress in Molecular and Environmental Bioengineering. From Analysis and Modeling to Technology Applications*. ed. by A. Carpi, ISBN: 978-953-307-268-5 (InTech, London, UK, 2011)
59. L. Zuo, Y. Zhang, L. Zhang, Y.-E. Miao, W. Fan, T. Liu, Polymer/carbon-based hybrid aerogels: Preparation, properties and applications. Materials **8**, 6806–6848 (2015)
60. J. Shen, D.Y. Guan, Preparation and application of carbon aerogels, in *Aerogels Handbook. Advances in Sol-Gel Derived Materials and Technologies*, ed. by M. Aegerter, N. Leventis, M. Koebel, (Springer, New York, 2011)
61. X. Yao, Y. Zhao, Three-dimensional porous graphene networks and hybrids for Lithium-ion batteries and supercapacitors. Chem **2**, 171–200 (2017)
62. K.-S. Lin, Y.-J. Mai, S.-W. Chiu, J.-H. Yang, S.L I. Chan. Synthesis and rage. J. Nanomater. **2012**, Article ID 201584, 9 pp (2012)
63. K. Kreek, K. Kriis, B. Maaten, et al., Organic and carbon aerogels containing rare-earth metals: Their properties and application as catalysts. J. Non-Cryst. Solids **404**, 43–48 (2014)
64. C. Macias, G. Rasines, T.E. García, et al., Synthesis of porous and mechanically compliant carbon aerogels using conductive and structural additives. Gels **2**, 4 (2016)
65. B. Xue, M. Qin, J. Wu, et al., Electroresponsive supramolecular graphene oxide hydrogels for active Bacteria adsorption and removal. ACS Appl. Mater. Interfaces **8**(24), 15120–15127 (2016)
66. C. Shen, E. Barrios, M. McInnis, J. Zuyus, L. Zhai, Fabrication of graphene aerogels with heavily loaded metallic nanoparticles. Micromachines **8**, 47 (2017)
67. Y. Liu, H. Wang, D. Lin, J. Zhao, C. Liu, J. Xie, Y. Cui, A Prussian blue route to nitrogen-doped graphene aerogels as efficient electrocatalysts for oxygen reduction with enhanced active site accessibility. Nano Res. **10**(4), 1213–1222 (2017)
68. H. Guo, T. Jiao, Q. Zhang, W. Guo, Q. Peng, X. Ya, Preparation of graphene oxide-based hydrogels as efficient dye adsorbents for wastewater treatment. Nanoscale Res. Lett. **10**, 272 (2015)
69. Y. Hu, X. Tong, H. Zhuo, et al., 3D hierarchical porous N-doped carbon aerogel from renewable cellulose: An attractive carbon for high-performance supercapacitor electrodes and CO_2 adsorption. RSC Adv. **6**, 15788–15795 (2016)
70. M. Yu, Y. Han, J. Li, L. Wang, One-step synthesis of sodium carboxymethyl cellulose-derived carbon aerogel/nickel oxide composites for energy storage. Chem. Eng. J. **324**, 287–295 (2017)
71. J. Štefelová, M. Mucha, T. Zelenka, Cellulose acetate-based carbon xerogels and cryogels. WIT Transactions on Engineering Sciences **77**., WIT Press, 65–75 (**2013**)
72. P. Hao, Z. Zhao, J. Tian, et al., Hierarchical porous carbon aerogel derived from bagasse for high performance supercapacitor electrode. Nanoscale **6**, 12120–12129 (2014)
73. A. Feaver, S. Sepehri, P. Shamberger, A. Stowe, T. Autrey, G. Cao, Coherent carbon Cryogel-ammonia borane nanocomposites for H_2 storage. J. Phys. Chem. B **111**, 7469–7472 (2007)

74. C. Alegre, D. Sebastián, E. Baquedano, et al., Tailoring Synthesis Conditions of Carbon Xerogels towards Their Utilization as Pt-Catalyst Supports for Oxygen Reduction Reaction (ORR). Catalysts **2**, 466–489 (2012)
75. N. Mahata, A.R. Silva, M.F.R. Pereira, C. Freire, B. de Castro, J.L. Figueiredo, Anchoring of a [Mn(salen)Cl] complex onto mesoporous carbon xerogels. J. Colloid Interface Sci. **311**, 152–158 (2007)
76. W. Kicinski, M. Szala, M. Nita, Structurally tailored carbon xerogels produced through a sol–gel process in a water–methanol–inorganic salt solution. J. Sol-Gel Sci. Technol. **58**, 102–113 (2011)
77. W. Xia, B. Qiu, D. Xia, R. Zou, Facile preparation of hierarchically porous carbons from metal-organic gels and their application in energy storage. Sci. Rep. **3**, 1935, 7 pp (2013)
78. E. Kowsari, High-performance supercapacitors based on ionic liquids and a graphene nanostructure, in *Ionic Liquids – Current State of the Art*, (Intech, London, UK, 2015), pp. 505–542
79. G. Yushin, A. Nikitin, Y. Gogotsi, Carbide-derived carbon, in *Nanomaterials Handbook*, (Taylor & Francis Group, Boca Raton, 2006)
80. V. Presser, M. Heon, Y. Gogotsi, Carbide-derived carbons – From porous networks to nanotubes and graphene. Adv. Funct. Mater. **21**, 810–833 (2011)
81. P. Simon, Y. Gogotsi, Materials for electrochemical capacitors. Nat. Mater. **7**(11), 845–854 (2008)
82. V. Presser, L. Zhang, J.J. Niu, J. McDonough, C. Perez, H. Fong, Y. Gogotsi, Flexible Nano-felts of carbide-derived carbon with ultra-high power handling capability. Adv. Energy Mater. **1**(3), 423–430 (2011)
83. J. Chmiola, G. Yushin, Y. Gogotsi, C. Portet, P. Simon, P.L. Taberna, Anomalous Increase in Carbon Capacitance at Pore Sizes of Less Than 1 Nanometer. Science **313**(5794), 1760–1763 (2006)
84. S.H. Yeon, P. Reddington, Y. Gogotsi, J.E. Fischer, C. Vakifahmetoglu, P. Colombo, Carbide-derived-carbons with hierarchical porosity from a preceramic polymer. Carbon **48**, 201–210 (2010)
85. Y. Gogotsi, Not just graphene – The wonderful world of carbon and related nanomaterials. MRS Bull. **40**, 1110–1120 (2015)
86. M. Rose, Y. Korenblit, E. Kockrick, L. Borchard, M. Oschatz, S. Kaskel, G. Yushin, Hierarchical micro-and mesoporous carbide-derived carbon as a high-performance electrode material in supercapacitors. Small **7**(8), 1108–1117 (2011)
87. R. Dash, J. Chmiola, G. Yushin, Y. Gogotsi, G. Laudisio, J. Singer, J.E. Fischer, S. Kucheyev, Titanium carbide derived Nanoporous carbon for energy-related applications. Carbon **44**(12), 2489–2497 (2006)
88. M. Sevilla, R. Mokaya, Activation of carbide derived carbons: A route to materials with enhanced gas and energy storage properties. J. Mater. Chem. **21**, 4727–4732 (2011)
89. E.N. Hoffman, G. Yushin, B.G. Wendler, M.W. Barsouma, Y. Gogotsi, Carbide-derived carbon membrane. Mater. Chem. Phys. **112**(2), 587–591 (2008)
90. C. Portet, D. Kazachkin, S. Osswald, Y. Gogotsi, E. Borguet, Impact of synthesis conditions on surface chemistry and structure of carbide-derived carbons. Thermochim. Acta **497**, 137–142 (2010)
91. B. Krüner, C. Odenwald, A. Tolosa, A. Schreiber, M. Aslan, G. Kickelbick, V. Presser, Carbide-derived carbon beads with tunable nanopores from continuously produced polysilsesquioxanes for supercapacitor electrodes. Sustainable Energy Fuels **1**, 1588–1600 (2017)
92. S. Ishikawa, T. Saito, K. Kuwahara, Carbon Materials with Nano-sized Pores Derived from Carbides. Sei Technical Review **82**, 152–157 (2016)
93. M.R. Lukatskaya, J. Halim, B. Dyatkin, M. Naguib, Y.S. Buranova, M.W. Barsoum, Y. Gogotsi, Room-temperature carbide-derived carbon synthesis by electrochemical etching of MAX phases. Angew. Chem. **126**, 4977–4980 (2014)
94. H.S. Cheng, M.R. Shen, C.L. Mak, P.K. Lim. Liquid phase electrochemical route to carbon nanotubes at room temperature. Proceedings of the *1st IEEE International Conference on Nano/Micro Engineered and Molecular Systems*, January 18–21, 2006, Zhuhai, China. pp.484–487 (2006)
95. A. Shawky, S. Yasuda, K. Murakoshi, Room-temperature synthesis of single-wall carbon nanotubes by an electrochemical process. Carbon **50**, 4184–4191 (2012)
96. S.K. Mandal, S. Hussain, A.K. Pal, Growth mechanism of carbon nanotubes deposited by electrochemical technique. Ind. J. Pure Appl. Phys. **43**, 765–771 (2005)
97. K. Yamagiwa, J. Kuwano, Synthesis of highly aligned carbon nanotubes by one-step liquid-phase process: Effects of carbon sources on morphology of carbon nanotubes. Jap. J. Appl. Phys. **56**, 06GE05 (2017)
98. L. Zhang, X. Qina, G. Shaoa, Z. Ma, S. Liu, C. He, A new route for preparation of titanium carbide derived carbon and its performance for supercapacitors. Mater. Lett. **122**, 78–81 (2014)
99. A.H. Farmahini, D.S. Sholl, S.K. Bhatia, Fluorinated carbide-derived carbon: More hydrophilic, yet apparently more hydrophobic. J. Am. Chem. Soc. **137**(18), 5969–5979 (2015)
100. B. Li, H.-M. Wen, W. Zhou, J.Q. Xu, B. Chen, Porous metal-organic frameworks: Promising materials for methane storage. Chem **1**, 557–580 (2016)
101. S.K. Bhatia, T.X. Nguyen, Potential of silicon carbide-derived carbon for carbon capture. Ind. Eng. Chem. Res. **50**, 10380–10383 (2011)
102. Z. Zondaka, R. Valner, A. Aabloo, T. Tamm, R. Kiefer, Embedded carbide-derived carbon particles in polypyrrole for linear actuator. Proc. SPIE **9798**, 97981H-7 (2016)
103. W. Xing, C. Liu, Z. Zhou, J. Zhou, G. Wang, S. Zhuo, et al., Oxygen-containing functional group-facilitated CO_2 capture by carbide-derived carbons. Nanoscale Res. Lett. **9**, 189 (2014)
104. L. Borchardt, F. Hasche, M.R. Lohe, et al., Transition metal loaded silicon carbide-derived carbons with enhanced catalytic properties. Carbon **50**, 1861–1870 (2012)
105. J. Gläsel, J. Diao, Z. Feng, M. Hilgart, T. Wolker, D. Sheng Su, B.J.M. Etzold, Mesoporous and graphitic carbide-derived carbons as selective and stable catalysts for the dehydrogenation reaction. Chem. Mater. **27**, 5719–5725 (2015)
106. J. Tae Lee, H. Kim, M. Oschatz, D.-C. Lee, F. Wu, H.-T. Lin, et al., Micro- and mesoporous carbide-derived carbon–selenium cathodes for high-performance lithium selenium batteries. Adv. Energy Mater. **5**, 1400981 (2014)
107. W. Nickel, M. Oschatz, M. von der Lehr, M. Leistner, et al., Direct synthesis of carbide-derived carbon monoliths with hierarchical pore design by hardtemplating. J. Mater. Chem. A **2**, 12703 (2014)

108. P.-C. Gao, W.-Y. Tsai, B. Daffos, P.-L. Taberna, C.R. Pérez, Y. Gogotsi, P. Simon, F.G. Favier, Carbide derived carbon for high-power supercapacitors. Nano Energy **12**, 197–206 (2015)
109. H. Wang, Q.-L. Zhu, R. Zou, Q. Xu, Metal-organic frameworks for energy applications. Chem **2**, 52–80 (2017)
110. K. Shen, X. Chen, J. Chen, Y. Li, Development of MOF-derived carbon-based nanomaterials for efficient catalysis. ACS Catal. **6**(9), 5887–5903 (2016)
111. Q. Ren, H. Wang, X.-F. Lu, Y.-X. Tong, G.-R. Li, Recent Progress on MOF-derived heteroatom-doped carbon-based Electrocatalysts for oxygen reduction reaction. Adv. Sci. **5**(3), 1700515 (2018)
112. L. Lux, K. Williams, S. Ma, Heat-treatment of metal–organic frameworks for green energy applications. CrystEngComm **17**, 10–22 (2015)
113. A. Dhakshinamoorthy, H. Garcia, Catalysis by metal nanoparticles embedded on metal–organic frameworks. Chem. Soc. Rev. **41**, 5262–5284 (2012)
114. P. Silva, S.M.F. Vilela, J.P.C. Tome, F.A. Almeida Paz, Multifunctional metal–organic frameworks: From academia to industrial applications. Chem. Soc. Rev. **44**, 6774–6803 (2015)
115. B. Liu, H. Shioyama, H. Jiang, X. Zhang, Q. Xu, Metal–organic framework (MOF) as a template for syntheses of nanoporous carbons as electrode materials for supercapacitor. Carbon **48**, 456–463 (2010)
116. M. Yang, X. Hu, Z. Fang, et al., Bifunctional MOF-derived carbon photonic crystal architectures for advanced Zn–air and li–S batteries: Highly exposed graphitic nitrogen matters. Adv. Funct. Mater. **27**(36), 1701971 (2017)
117. X. Li, J. Zhang, Y. Han, M. Zhu, S. Shang, W. Li, MOF-derived various morphologies of N-doped carbon composites for acetylene hydrochlorination. J. Mater. Sci. **7** (2018). https://doi.org/10.1007/s10853-017-1951-3
118. B. Chen, G. Ma, D. Kong, Y. Zhu, Y. Xia, Atomically homogeneous dispersed ZnO/N-doped nanoporous carbon composites with enhanced CO_2 uptake capacities and high efficient organic pollutants removal from water. Carbon **95**, 113–124 (2015)
119. W. Zhang, Z.-Y. Wu, H.-L. Jiang, S.-H. Yu, Nanowire-directed templating synthesis of metal−organic framework nanofibers and their derived porous doped carbon nanofibers for enhanced Electrocatalysis. J. Am. Chem. Soc. **136**, 14385–14388 (2014)
120. H.-L. Jiang, B. Liu, Y.-Q. Lan, et al., From metal-organic framework to Nanoporous carbon: Toward a very high surface area and hydrogen uptake. J. Am. Chem. Soc. **133**(31), 11854–11857 (2011)
121. B. Ding, J. Wang, Z. Chang, G. Xu, et al., Self-sacrificial template-directed synthesis of metal–organic framework-derived porous carbon for energy-storage devices. Chem. Electro. Chem. **3**(4), 668–674 (2016)
122. R. Chen, T. Zhao, T. Tian, et al., Graphene-wrapped sulfur/metal organic framework-derived microporous carbon composite for lithium sulfur batteries. APL Materials **2**, 124109 (2014)
123. H. Bin Wu, S. Wei, L. Zhang et al. Embedding Sulfur in MOF-Derived Microporous Carbon Polyhedrons for Lithium–Sulfur Batteries. *Chemistry, a Eur. J.*, **2013**, *9*(33), 10804–10808
124. A. Banerjee, K.K. Upadhyay, et al., MOF-derived crumpled-sheet-assembled perforated carbon cuboids as highly effective cathode active materials for ultra-high energy density li-ion hybrid electrochemical capacitors (li-HECs). Nanoscale **6**(8), 4387–4394 (2014)
125. T. Segakwenga, N.M. Musyoka, J. Ren, et al., Comparison of MOF-5 and MIL-101 derived carbons for hydrogen storage application. Res. Chem. Intermed. **42**, 4951 (2015). https://doi.org/10.1007/s11164-015-2338-1
126. A. Li, Y. Tong, B. Cao, H. Song, et al. MOF-derived multifractal porous carbon with ultrahigh lithium-ion storage performance. Scientific Rep. **7**, Article number: 40574 (2017)
127. H. Li, L. Chi, C. Yang, L. Zhang, et al., MOF derived porous Co@C hexagonal-shaped prisms with high catalytic performance. J. Mater. Res. **31**(19), 3069–3077 (2016)
128. S. Hoon Ahn, A. Manthiram, Self-templated synthesis of co- and N-doped carbon microtubes composed of hollow Nanospheres and nanotubes for efficient oxygen reduction reaction. Small **13**(11), 1603437 (2017)
129. Y.-X. Zhou, Y.-Z. Chen, L. Cao, et al., Conversion of a metal–organic framework to N-doped porous carbon incorporating co and CoO nanoparticles: Direct oxidation of alcohols to esters. Chem. Commun. **51**, 8292–8295 (2015)
130. K.-Y.A. Lin, H.-A. Chang, B.-J. Chen, Multi-functional MOF-derived magnetic carbon sponge. J. Mater. Chem. A **4**, 13611–13625 (2016)
131. N.L. Torad, M. Hu, S. Ishihara, et al., Direct synthesis of MOF-derived nanoporous carbon with magnetic co nanoparticles toward efficient water treatment. Small **10**(10), 2096–2107 (2014)
132. X. Liu, X. Quan, Fe-MOF derived ferrous hierarchically porous carbon used as EF cathode for PFOA degradation. Journal of Geoscience and Environment Protection **5**(6), 9–14 (2017)
133. E.C. Walter, T. Beetz, M.Y. Sfeir, L.E. Brus, M.L. Steigerwald, Crystalline graphite from an organometallic solution-phase reaction. J. Am. Chem. Soc. **128**(49), 15590–15591 (2006)
134. W. Sisi, Z. Yinggang, H. Yifeng, et al., Bimetallic organic frameworks derived CuNi/carbon nanocomposites as efficient electrocatalysts for oxygen reduction reaction. Sci. China Mater. **60**(7), 654–663 (2017)
135. D.Z. Chen, C.Q. Chen, W.S. Shen, et al., MOF-derived magnetic porous carbon-based sorbent: Synthesis, characterization, and adsorption behavior of organic micropollutants. Adv. Powder Technol. ***28***(7), 1769–1779 (2017)
136. S. Hoon Ahn, M.J. Klein, A. Manthiram, 1D co- and N-doped hierarchically porous carbon nanotubes derived from bimetallic metal organic framework for efficient oxygen and tri-iodide reduction reactions. Adv. Energy Mater. **7**(7), 1601979 (2017)
137. Q. Gan, K. Zhao, S. Liu, Z. He, MOF-derived carbon coating on self-supported $ZnCo_2O_4$–ZnO nanorod arrays as high-performance anode for lithium-ion batteries. J. Mater. Sci. **52**(13), 7768–7780 (2017)
138. Z. Li, L. Yin, MOF-derived, N-doped, hierarchically porous carbon sponges as immobilizers to confine selenium as cathodes for li–se batteries with superior storage capacity and perfect cycling stability. Nanoscale **7**, 9597–9606 (2015)
139. W. Chaikittisilp, K. Ariga, Y. Yamauchi, A new family of carbon materials: Synthesis of MOF-derived nanoporous carbons and their promising applications. J. Mater. Chem. A **1**, 14–19 (2013)
140. M. Hui Yap, K. Loon Fow, G. Zheng Chen, Synthesis and applications of MOF-derived porous nanostructures. Green Energy Environ. **2**(3), 218–245 (2017)
141. S. Fardindoost, S. Hatamie, A. Iraji Zad, F. Razi Astaraei, Hydrogen sensing properties of nanocomposite graphene oxide/co-based metal organic frameworks (co-MOFs@GO). Nanotechnology **29**, 015501 (2018). (7 pp)

142. G. Cai, W. Zhang, L. Jiao, S.-H. Yu, H.-L. Jiang, Template-directed growth of well-aligned MOF arrays and derived self-supporting electrodes for water splitting. Chem **2**(6), 791–802 (2017)
143. T. Nagy, L. Yunq, I. Shinsuke, et al., MOF-derived nanoporous carbon as intracellular drug delivery carriers. Chem. Lett. **43**(5), 717–719 (2014)
144. L. Xiao, R. Xu, Q. Yuan, F. Wang, Highly sensitive electrochemical sensor for chloramphenicol based on MOF derived exfoliated porous carbon. Talanta **167**, 39–43 (2017)
145. W. Li, S. Hu, X. Luo, et al., Confined amorphous red phosphorus in MOF-derived N-doped microporous carbon as a superior anode for sodium-ion battery. Adv. Mater. **29**(16), 1605820 (2017)
146. S. Pandiaraj, H.B. Aiyappa, R. Banerjee, S. Kurungot, Post modification of MOF derived carbon via g-C_3N_4 entrapment for an efficient metal-free oxygen reduction reaction. Chem. Commun. **50**, 3363–3366 (2014)
147. Shock compression research shows hexagonal diamond could serve as meteor impact marker. https://www.llnl.gov/news/shock-compression-research-shows-hexagonal-diamond-could-serve-meteor-impact-marker. Accessed on 2 Nov 2017
148. A.G. Kvashnin, P.B. Sorokin, Lonsdaleite films with nanometer thickness. J. Phys. Chem. Lett. **5**, 541–548 (2014)
149. http://aflowlib.duke.edu/users/egossett/lattice/struk.picts/hexdia.s.png. Accessed on 2 Nov2017
150. Structure of the Diamond-lonsdaleite System. http://www.imaging-git.com/science/electron-and-ion-microscopy/structure-diamond-lonsdaleite-system. Accessed on 2 Nov 2017
151. P. Nemeth, L.A.J. Garvie, T. Aoki, N. Dubrovinskaia, L. Dubrovinsky, P.R. Buseck, Lonsdaleite is faulted and twinned cubic diamond and does not exist as a discrete material. Nat. Commun. **5**, 5447, 5 pp (2014)
152. L. Qingkun, S. Yi, L. Zhiyuan, Z. Yu, Lonsdaleite – A material stronger and stiffer than diamond. Scr. Mater. **65**, 229–232 (2011)
153. D. Kraus, A. Ravasio, M. Gauthier, D.O. Gericke, et al., Nanosecond formation of diamond and lonsdaleite by shock compression of graphite. Nat. Commun. **7**, 10970, 6 pp (2016)
154. B. Kulnitskiy, I. Perezhogin, G. Dubitskya, V. Blank, Polytypes and twins in the diamond–lonsdaleite system formed by high-pressure and high-temperature treatment of graphite. Acta Cryst **B69**, 474–479 (2013)
155. Y. Nakamuta, S. Toh, Transformation of graphite to lonsdaleite and diamond in the Goalpara ureilite directly observed by TEM. Am. Mineral. **98**(4), 574–581 (2015)
156. S.V. Goryainov, A.Y. Likhacheva, S.V. Rashchenko, A.S. Shubin, V.P. Afanas'eva, N.P. Pokhilenko, Raman identification of lonsdaleite in Popigai impactites. J. Raman Spectrosc. **45**, 305–313 (2014)
157. B. Qu, B. Zhang, L. Wang, R. Zhou, X. Cheng Zeng, L. Li, Persistent luminescence hole-type materials by design: Transition-metal-doped carbon allotrope and carbides. ACS Appl. Mater. Interfaces **8**(8), 5439–5444 (2016)
158. A. Milani, M. Tommasini, V. Russo, et al., Raman spectroscopy as a tool to investigate the structure and electronic properties of carbon-atom wires. Beilstein J. Nanotechnol. **6**, 480–491 (2015)
159. V.V. Sobolev, V.Y. Slobodskoy, S.N. Selyukov, A.A. Udoyev, Some conversions of chaoite to other carbon phases. Int. Geol. Rev. **28**(6), 680–683 (1986)
160. J. Pola, A. Ouchi, S. Bakardjieva, et al., Laser photochemical etching of silica: Nanodomains of crystalline chaoite and silica in amorphous C/Si/O/N phase. J. Phys. Chem. C **112**(34), 13281–13286 (2008)
161. A. Tembre, J. Henocque, M. Clin. Infrared and Raman spectroscopic study of carbon-cobalt composites. Int. J. Spectrosc. **2011**, Article ID 186471, 6 pp (2011)
162. S.K. Simakov, A.E. Kalmykov, L.M. Sorokin, et al., Chaoite formation from carbon-bearing fluid at low PT parameters. Dokl. Earth Sci. **399A** (9), 1289–1290 (2004)
163. S. Li, Z. Huang, et al., Ferromagnetic chaoite macrotubes prepared at low temperature and pressure. Appl. Phys. Lett. **90**, 232507 (2007)
164. S. Li, G. Ji, Z. Huang, F. Zhang, Y. Du, Synthesis of chaoite-like macrotubes at low temperature and ambient pressure. Carbon **45**, 2946–2950 (2007)
165. Q. Peng, A.K. Dearden, J. Crean, et al., New materials graphyne, graphdiyne, graphone, and graphane: Review of properties, synthesis, and application in nanotechnology. Nanotechnol. Sci. Appl. **7**, 1–29 (2014)
166. J.O. Sofo, A.S. Chaudhari, G.D. Barber, Graphane: A two-dimensional hydrocarbon. Phys. Rev. B **75**, 153401 (2007)
167. D.C. Elias, R.R. Nair, T.M.G. Mohiuddin, S.V. Morozov, P. Blake, M.P. Halsall, A.C. Ferrari, D.W. Boukhvalov, M.I. Katsnelson, A.K. Geim, K.S. Novoselov, Control of Graphene's properties by reversible hydrogenation: Evidence for Graphane. Science **323**(5914), 610–613 (2009)
168. H. Sahin, O. Leenaerts, S.K. Singh, F.M. Peeters. GraphAne: From synthesis to applications. arXiv:1502.05804 [cond-mat.mtrl-sci], (2015)
169. H. Zhang, Y. Miyamoto, A. Rubio. Laser-induced preferential dehydrogenation of graphane. Phys. Rev. B. **85**, 201409(R) (2012)
170. C. Zhou, S. Chen, J. Lou, J. Wang, et al., Graphene's cousin: The present and future of graphene. Nanoscale Res. Lett. **9**, 26 (2014)
171. H. Sahin, O. Leenaerts, S.K. Singh, F.M. Peeters, Graphane. WIREs Comput. Mol. Sci. **5**, 255–272 (2015)
172. A. Bhattacharya, S. Bhattacharya, C. Majumder, G.P. Das. Third conformer of graphane: A first-principles density functional theory study. Phys. Rev. B. **83**, Article ID 033404 (2011)
173. H. Einollahzadeh, S. Mahdi Fazeli, R. Sabet Dariani, Studying the electronic and phononic structure of penta-graphane. Sci. Technol. Adv. Mater. **17**(1), 610–617 (2016)
174. D. Haberer, C.E. Guusca, Y. Wang, et al., Evidence for a new two-dimensional C_4H-type polymer based on hydrogenated graphene. Adv. Mater. **23**, 4497–4503 (2011)
175. V.E. Antonov, I.O. Bashkin, A.V. Bazhenov, et al., Multilayer graphane synthesized under high hydrogen pressure. Carbon **100**, 465–473 (2016)
176. H. Peelaers, A.D. Hernández-Nieves, O. Leenaerts, B. Partoens, F.M. Peeters, Vibrational properties of graphene fluoride and graphene. Appl. Phys. Lett. **98**, 051914 (2011)
177. M. Pumera, Z. Sofer, Towards stoichiometric analogues of graphene: Graphane, fluorographene, graphol, graphene acid and others. Chem. Soc. Rev. **46**, 4450–4463 (2017)

178. B.-R. Wu, C.-K. Yang, Electronic structures of graphane with vacancies and graphene adsorbed with fluorine atoms. AIP Adv. **2**, 012173 (2012)
179. M.Z.S. Flores, P.A.S. Autreto, S.B. Legoas, D.S. Galvao, Graphene to graphane: A theoretical study. Nanotechnology **20**, 465704, 6 pp (2009)
180. W. Liu, F.-H. Meng, J.-H. Zhao, X.-H. Jiang, A first-principles study on the electronic transport properties of zigzag graphane/graphene nanoribbons. J. Theor. Comput. Chem. **16**(4), 1750032, 12 pp (2017)
181. J.-H. Lee, J.C. Grossman, Magnetic properties in graphene-graphane superlattices. Appl. Phys. Lett. **97**, 133102 (2010)
182. A.S. Barnarda, I.K. Snook, Size- and shape-dependence of the graphene to graphane transformation in the absence of hydrogen. J. Mater. Chem. **20**, 10459–10464 (2010)
183. T. Hussain, P. Panigrahi, R. Ahuja, Sensing propensity of a defected graphane sheet towards CO, H_2O and NO_2. Nanotechnology **25**(32), 325501 (2014)
184. J. Xiao, S. Sitamraju, M.J. Janik, CO_2 adsorption thermodynamics over N-substituted/grafted Graphanes: A DFT study. Langmuir **30**(7), 1837–1844 (2014)
185. T. Hussain, P. Panigrahi, R. Ahuja, Enriching physisorption of H_2S and NH_3 gases on a graphane sheet by doping with li adatoms. Phys. Chem. Chem. Phys. **16**(17), 8100–8105 (2014)
186. E. Ventura-Macias, J. Guerrero-Sánchez, N. Takeuchi, Formaldehyde adsorption on graphane. Computational and Theoretical Chemistry **1117**, 119–123 (2017)
187. T. Hussain, B. Pathak, M. Ramzan, T.A. Maark, R. Ahuja, Calcium doped graphane as a hydrogen storage material. Appl. Phys. Lett. **100**, 183902 (2012)
188. S.C. Ray, N. Soin, T. Makgato, et al., Graphene supported Graphone/Graphane bilayer nanostructure material for Spintronics. Sci. Reports **4**, 3862 (2014)
189. W. Zhao, J. Gebhardt, F. Spath, et al., Reversible hydrogenation of graphene on Ni(111)—Synthesis of "Graphone". Chem. Eur. J. **21**, 3347–3358 (2015)
190. L. Feng, W.X. Zhang, The structure and magnetism of graphone. AIP Adv. **2**, 042138 (2012)
191. Q. Peng, A.K. Dearden, X.-J. Chen, et al., Peculiar pressure effect on Poisson ratio of graphone as a strain damper. Nanoscale **7**, 9975–9979 (2015)
192. M. Neek-Amal, J. Beheshtian, F. Shayeganfar, S.K. Singh, J.H. Los, F.M. Peeters, Spiral graphone and one-sided fluorographene nanoribbons. Phys. Rev. B **87**, 075448 (2013)
193. A.I. Podlivaev, L.A. Openov, On the thermal stability of Graphone. Semiconductors **45**(7), 958–961 (2011)
194. D.W. Boukhvalov, Stable antiferromagneticgraphone. Physica **E43**, 199–201 (2010)
195. Q. Li, Y. Ma, A.R. Oganov, et al., Superhard monoclinic polymorph of carbon. Phys. Rev. Lett. **102**, 175506 (2009)
196. M.J. Xing, B.H. Li, Z.T. Yu, Q. Chen, Monoclinic C2/m-20 carbon: a novel superhard sp^3 carbon allotrope. RSC Adv. **6**, 32740–32745 (2016)
197. M. Amsler, J.A. Flores-Livas, M.A.L. Marques, S. Botti, S. Goedecker, Prediction of a novel monoclinic carbon allotrope. The European Physical Journal B **86**, 383 (2013)
198. J. Narayan, A. Bhaumik, Novel phase of carbon, ferromagnetism, and conversion into diamond. J. Appl. Phys. **118**, 215303 (2015)
199. J. Narayan, A. Bhaumik, Q-carbon discovery and formation of single-crystal diamond nano- and microneedles and thin films. Mater. Res. Lett. **4**(2), 118–126 (2016)
200. J. Pandey, R. Khare, S. Khare, Q-carbon: A new, inexpensive and affordable diamond in Everyones hand. International Journal for Research in Applied Science & Engineering **5**(V), 89–91 (2017)
201. https://www.nextbigfuture.com/2011/04/t-carbon-novel-carbon-allotrope.html. Accessed on 26 Nov 2017
202. X.-L. Sheng, Q.-B. Yan, F. Ye, Q.-R. Zheng, G.S. T-Carbon, A novel carbon allotrope. Phys. Rev. Lett. **106**, 155703 (2011)
203. J. Zhang, R. Wang, X. Zhu, et al. Pseudo-topotactic conversion of carbon nanotubes to T-carbon nanowires under picosecond laser irradiation in methanol. Nat. Commun. **8**, Article number 683 (2017)
204. D. Li, F. Tian, D. Duan, Z. Zhao, et al., Modulated T carbon-like carbon allotropes: An ab initio study. RSC Adv. **4**, 17364–17369 (2014)
205. J.Q. Wang, C.X. Zhao, C.Y. Niu, Q. Sun, Y. Jia, C_{20}-T carbon: A novel superhard sp^3 carbon allotrope with large cavities. J. Phys. Condens. Matter **28**(47), 475402 (2016)
206. Aegerter, Michel A., Leventis, Nicholas, Koebel, Matthias M. (Eds.), *Aerogels Handbook. Advances in Sol-Gel Derived Materials and Technologies*. (Springer, New York, 2011)